5-2018

Quantum correlations in nanophotonics: from long-range dipole-dipole interactions to fundamental efficiency limits of coherent energy transfer

Cristian L. Cortes
Purdue University

QUANTUM CORRELATIONS IN NANOPHOTONICS:

FROM LONG-RANGE DIPOLE-DIPOLE INTERACTIONS TO

FUNDAMENTAL EFFICIENCY LIMITS IN COHERENT ENERGY TRANSFER

A Dissertation

Submitted to the Faculty

of

Purdue University

by

Cristian L. Cortes

In Partial Fulfillment of the

Requirements for the Degree

of

Doctor of Philosophy

May 2018

Purdue University

West Lafayette, Indiana

THE PURDUE UNIVERSITY GRADUATE SCHOOL
STATEMENT OF DISSERTATION APPROVAL

Dr. Zubin Jacob, Chair

School of Electrical and Computer Engineering

Dr. Supriyo Datta

School of Electrical and Computer Engineering

Dr. Weng C. Chew

School of Electrical and Computer Engineering

Dr. Chen-Lung Hung

Department of Physics and Astronomy

Dr. Tongcang Li

Department of Physics and Astronomy

Approved by:

Dr. Venkataramanan Balakrishnan

Head of the School Graduate Program

For my parents.

ACKNOWLEDGMENTS

First and foremost, I would like to acknowledge my advisor Zubin Jacob for the many hours of discussions, for the lessons in communicating scientific ideas, for his patience, and for the freedom he gave me throughout my PhD. Zubin is certainly one of the most intuitive and creative people that I have met. His constant pursuit of knowledge spanning many fields in physics has always inspired my scientific output. Thank you Zubin. I would also like to provide my sincerest gratitude to Supriyo Datta. His guidance and support has been tremendous. My deepest thanks also go to Chen-Lung Hung, Tongcang Li, and Weng Cho Chew. Thank you for your input and for being part of my committee.

To my lab mates: thank you for your support, for all of our discussions, and for your sheer presence. You truly made my PhD much more enjoyable than I would have ever imagined.

This thesis would not have been realized without my family: my mother and father *Lucero* and *Rafael*, my sister *Estefania* and my little brother *Camilo*. I am so thankful to have your unwavering love and support every single day.

Finally, I want to thank *Kailan*, I am so grateful to have your support every day. You are my sunshine.

TABLE OF CONTENTS

Page

Page

Page

LIST OF TABLES

LIST OF FIGURES

Figure Page

Figure Page

Figure Page

Figure Page

SYMBOLS

$\mathbf{E}$	Electric field vector
$\mathbf{B}$	Magnetic field vector
$\mathbf{A}$	vector potential
ϕ	scalar potential
$\mathbf{G}$	dyadic Green function
ρ_N	noise charge density
$\mathbf{j}_N$	noise current density
$\mathbf{d}$	electric dipole moment
$\mathbf{m}$	magnetic dipole moment
$\mathbf{k}$	wavevector
$\boldsymbol{\epsilon}$	dielectric permittivity tensor
ϵ_o	permittivity of free-space
μ_o	permeability of free-space
c	speed of light in vaccum
ω	radial frequency
H	Hamiltonian
$\mathbf{p}$	momentum vector for charged particle
$\mathbf{f}^\dagger/\mathbf{f}$	creation/annihilation vector operator for polaritonic field
η_{et}	energy transfer efficiency
Q_D	intrinsic quantum efficiency of donor
F_p	Purcell factor
F_{et}	Energy transfer figure of merit
Q	quality factor
C	concurrence

ABSTRACT

Cortes, Cristian L. PhD, Purdue University, May 2018. **Quantum Correlations in Nanophotonics:** *From Long-Range Dipole-Dipole Interactions to Fundamental Efficiency Limits in Coherent Energy Transfer.* Major Professor: Zubin Jacob.

Quantum properties like coherence and entanglement can lead to enhanced performance characteristics in a wide range of applications including quantum computation, quantum memory storage, optical sensing, and energy harvesting. Entanglement is very sensitive to static and dynamical disorder. Similarly, the generation of highly-entangled states requires strong coupling or strong driving fields. Satisfying all of these requirements is generally quite difficult. In the first part of this thesis, we present an approach to overcome these limitations through the use of exotic light-matter states in hyperbolic media which provide a new approach to control quantum correlations and interatomic interactions. We reveal a class of excited-state, long-range interactions, referred to as *Super-Coulombic* interactions that are singular along a material-dependent resonance angle. In practical systems, the Super-Coulombic interaction achieves dipole-dipole coupling that is orders of magnitude larger than conventional approaches, while also occurring across a large frequency bandwidth making it robust to static energy-level disorder. This unique hyperbolic response is not only naturally occurring, found in materials like h-BN, $BiTe_2$, $BiSe_2$, and mono-layered black phosphorus, but can also be designed with artificial nanostructured materials (metamaterials) to create the desired hyperbolic dispersion across different parts of the electromagnetic spectrum. Our theoretical prediction motivated an intense search for the effect and was confirmed by an experimental demonstration at room temperature. To obtain agreement with experimental results, we present a rigorous theoretical framework that takes into account ensemble effects, finite-sized effects,

and dimensional effects that arise from confined geometries ultimately modifying the Super-Coulombic spatial scaling law.

In the second part of this thesis, we solve an outstanding theoretical problem dealing with the control of resonance energy transfer in nanophotonic environments in both the incoherent and coherent coupling limits. Resonance energy transfer is a fundamental process that is the subject of intense research across all sciences. For example, in chemistry for drug delivery and chemical monitoring, in engineering for photovoltatic and up-conversion devices, and in biology for exciton transport within photosynthetic complexes. First, we consider the disordered and weak coupling limit of resonance energy transfer often encountered in chemistry. We propose new design principles for enhancing and suppressing the energy transfer rate and efficiency quantitatively captured by a simple image dipole model. Our theory explains a wide range of experimental results which have been the subject of an ongoing debate for the past 15 years. Second, we present our recent result aimed at understanding the fundamental role of entanglement and quantum coherence in resonance energy transfer. To uncover the role of these effects, we develop a unified theory of energy transfer valid from the incoherent to quantum coherent coupling regimes. Ultimately, our theory reveals a fundamental bound $\eta_{max} = \frac{\gamma_a}{\gamma_d+\gamma_a}$ for energy transfer efficiency arising from the spontaneous emission rates γ_d and γ_a of the donor and acceptor. This bound provides an upper limit to the efficiency of energy transfer regardless of quantum coherence or entanglement, suggesting new design principles for achieving near-unity energy transfer efficiency in coherent systems. The result has important implications for the two-chromophore model found in photosynthetic complexes and paves the way for nanophotonic analogues of efficiency-enhancing environments mimicking biological photosynthetic systems.

1. INTRODUCTION

Quantum properties like coherence and entanglement can lead to enhanced performance metrics in a wide variety of applications. In quantum computation, Shor's algorithm uses quantum coherence to solve prime factoring problems significantly faster than classical algorithms [1–5]. In quantum metrology, quantum squeezed light is used to go beyond classical noise measurement limits [6–8]. In quantum thermodynamics, the use of quantum coherence and quantum correlations has been proposed to go beyond the Carnot efficiency limit of classical heat engines [9–11]. And in quantum biology, landmark experiments have shown long-lived coherence ranging on the order of hundreds of femtoseconds up to several picoseconds suggesting its role in the near-unity energy transfer efficiency of photosynthetic systems [12–14]. The idea of quantum coherence playing a role in photosynthesis is intriguing because it indicates many-body quantum correlations may exist in ambient conditions with the potential for a wide range of technological applications [15–17].

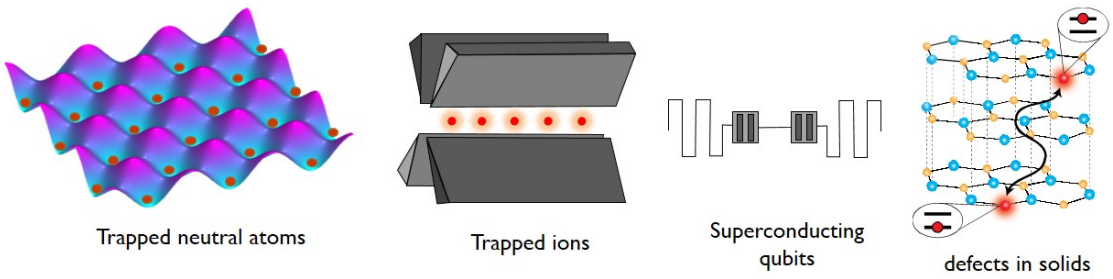

Fig. 1.1. *Leading quantum platforms.* A single two-level system, or qubit, represents the building block of more complex quantum systems. Scaling up these platforms to many qubits provides a formidable challenge because it requires the precise control of exponentially growing degrees of freedom.

As shown in Fig. 1.1, the leading quantum system platforms include trapped ultracold atoms, trapped ions, superconducting qubits, and dopants/defects in solid-state systems (e.g. color centers in diamond). These platforms emerged as a result of their long coherence times and controllable quantum states, typically achieved through optical pumping, or external AC/DC electric or magnetic fields. As quantum systems are scaled up to include multiple qubits or atoms, the task of controlling them will become exponentially more difficult. Generating entanglement requires strong light-matter or inter-qubit coupling, while maintaining entanglement requires precise decoupling from the environment. The former is difficult due to the properties of the Rabi frequency in vacuum, which is intrinsically small. The latter is difficult because entanglement is innately sensitive to both static disorder (static shifts in the energy level) as well as dynamical disorder (fluctuations in the energy level). Overcoming all of these requirements is paramount for future quantum technologies, however, as it stands today it is an open question as to how we can generate, control, and maintain entanglement within a large many-body system.

1.1 From quasi-particles to quantum materials

The central theme of this thesis is to tackle the control of quantum correlations from a nanophotonics and materials engineering approach. This approach is motivated by potential long-term applications as well as pure theoretical pursuit. One the one hand, we expect the future commercialization of quantum devices will require a solid-state platform. That is, if we ever expect integration within a robust hand-held device, it is worthwhile to consider *how* that will be achieved. One possible way is through the control of dopants or defects in solid-state systems. Consider the interaction between two qubits inside a material like hexagonal Boron nitride (h-BN), as shown on the right of Fig 1.1. If such a dopant or defect state were to exist, then it would interact with other dopants through the light-matter states, also known as quasi-particles, of the material. This brings an additional degree of freedom from the

material itself that could potentially increase the inter-qubit interaction while also making it robust to static or dynamical disorder. In the future, the emergent field of *quantum materials* (2D materials, topological insulators, etc.) may play an important role where one expects quantum device engineers to take advantage of the wide range exotic material properties. From a theorist perspective, it is then important to consider what theoretical framework will take into account all of these considerations in the simplest way possible. The ideal framework should take into account the material properties, the qubit properties, effects arising from external fields, as well as full quantization of system variables to utilize quantum information protocols.

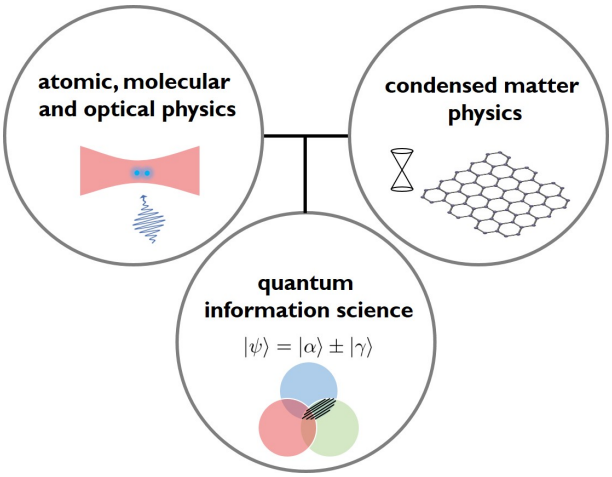

This thesis utilizes a so-called *macroscopic quantum electrodynamics* (QED) framework to provide a unified view of these aspects. Material properties are taken into account through linear response functions like polarization $\mathbf{P}(\mathbf{r}, t)$ and magnetization $\mathbf{M}(\mathbf{r}, t)$, which may be determined experimentally or through *ab-initio* numerical approaches. The material response functions are incorporated into Maxwell's equations forming the well-known macroscopic Maxwell's equations. Upon quantization, we obtain a suitable framework that can describe the interaction between atoms and polaritons (describing light-matter states). Unlike much of the work in cavity QED that has dealt with the interaction of a single atom and a single cavity mode, this thesis uses a theoretical treatment that is applicable to general nanophotonic environments.

Our focus will be to study how atom-atom interactions are modified within the class of media exhibiting hyperbolic dispersion.

1.2 Hyperbolic media

The progress of nanofabrication and material research has led to establishing the concept of artificial materials: metamaterials. The metamaterial approach requires the control of the material response through structural resonances and near-field coupling between sub-wavelength meta-atoms. Metamaterial research has led to exotic effects such as negative refraction, sub-wavelength imaging, invisibility cloaking, exotic chiral media, meta-surfaces, and perfect absorption [18–24]. One of the most important classes of artificial media that emerged in the optical frequency regime are now referred to as hyperbolic or indefinite media. It is a uniaxial (birefringent)

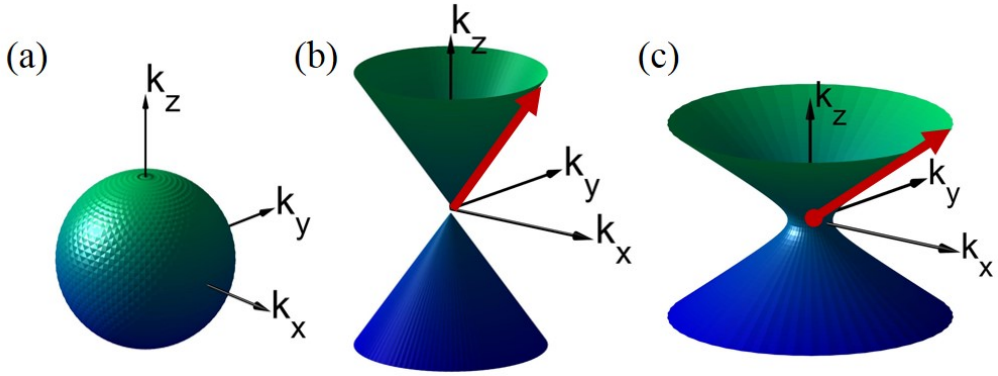

Fig. 1.2. ***k*-space topology.** The isofrequency contour for (a) an isotropic dielectric is a sphere, while for (b) extraordinary waves in a uniaxial medium with extreme anisotropy ($\epsilon_x = \epsilon_y > 0$ and $\epsilon_z < 0$) is a hyperboloid (type I). (c) A type II hyperboloid arises when two components of the dielectric tensor are negative ($\epsilon_x = \epsilon_y < 0$ and $\epsilon_z > 0$). Note that hyperbolic media (b) and (c) can support propagating waves with unbounded wavevectors (red arrow) as opposed to isotropic media.

medium described by the permittivity tensor,

$$\boldsymbol{\epsilon} = \begin{pmatrix} \epsilon_{xx} & 0 & 0 \\ 0 & \epsilon_{xx} & 0 \\ 0 & 0 & \epsilon_{zz} \end{pmatrix}, \tag{1.1}$$

where z-direction corresponds to the optic axis expressed in Cartesian coordinates. By solving the vector wave equation, one finds two polarization wave solutions: (1) *ordinary* waves satisfying the dispersion relation, $k_x^2 + k_y^2 + k_z^2 = \epsilon_{xx}\,\omega^2/c^2$, and (2) *extraordinary* waves satisfying the dispersion relation

$$\frac{k_x^2 + k_y^2}{\epsilon_{zz}} + \frac{k_z^2}{\epsilon_{xx}} = \frac{\omega^2}{c^2}. \tag{1.2}$$

Conventional uniaxial crystals have permittivity components that are positive ($\epsilon_{xx}\epsilon_{zz} > 0$) representing glass-like behavior. For such a crystal, the dispersion relation at a single-frequency, also known as the iso-frequency surface, describes the surface of an ellipsoid (see Fig. 1.2-a). If one of the components is negative ($\epsilon_{xx}\epsilon_{zz} < 0$) representing metal-like behavior, the iso-frequency surface changes to that of a hyperboloid (see Fig. 1.2-b and Fig. 1.2-c). The term *hyperbolic medium* arises from the shape of the iso-frequency surface. It is important to note that the hyperbolic response is a *non-resonant* effect occurring for a broad range of frequencies.

While the work of hyperbolic metamaterials was initiated by their ability to exhibit negative refraction, research of this medium diversified into a wide-range of applications ranging from sub-wavelength imaging, nanoscale waveguiding, as well as broadband thermal emission and absorption [25–27] . As an example, the work by Jacob et al. [28] proposed hyperbolic media for the use of quantum-based applications such as room-temperature single-photon sources. Since the photonic density of states is a measure of the infinitesimal volume of the constant energy surface (Fig. 1.2), a hyperbolic medium accordingly has a divergent photonic density of states occurring for a broad range of wavelengths. This property allows for enhanced emission rates of broadband quantum emitters operating at room temperature.

1.3 Overview of the thesis

In Chapter 2, we introduce the macroscopic quantum electrodynamic framework that will be used throughout this thesis. Note that previous work in hyperbolic media primarily focused on the semi-classical limit that often requires many ad-hoc assumptions. The quantum electrodynamic framework we present in this thesis provides a self-consistent and unified treatment of both single-atom and multi-atom processes like the cooperative Lamb shift, cooperative decay rate, Casimir-Polder interaction, as well Förster resonance energy transfer. In Chapter 3, we explore the modification of dipole-dipole interactions inside a hyperbolic medium which ultimately gives rise to Super-Coulombic interactions. This is the first major result of this thesis. Chapter 4 extends the framework to take into account incoherent many-body effects between multiple emitters, as well as dimensional effects arising from confined geometries. We also discuss an experiment that was performed to verify the Super-Coulombic long-range dipole-dipole interaction.

The second part of this thesis will aim to resolve an outstanding theoretical problem regarding resonance energy transfer in nanophotonics ranging from classically incoherent to quantum coherent regimes. Chapter 5 will deal with the disordered and incoherent regime. We will show that a simple image dipole model can be used to explain how Förster resonance energy transfer (FRET) is modified within various nanophotonic environments. The model provides a simple way of understanding multiple experiments which have used incorrect interpretations of certain observed phenomena. In chapter 6, we consider the question of whether quantum entanglement and coherence may be used to enhance the *efficiency* of energy transfer between two atoms. We develop a unified quantum model that connects the incoherent and coherent regimes, exactly solving the model to provide a simple solution for the energy transfer efficiency in both regimes. Our result uncovers a fundamental efficiency bound that limits the energy transfer efficiency even in the presence of maximal en-

tanglement or quantum coherence. This forms the second major result of this thesis. The final chapter provides a brief conclusion and future outlook of the current work.

Other major contributions

We have excluded the following first-author papers from this thesis:

[1] Cortes, C.L., Newman, W., Molesky, S., Jacob, Z. *Quantum nanophotonics using hyperbolic metamaterials*. J. Opt. 14 063001, (2012).
[2] Cortes, C.L., Jacob, Z. *Photonic analog of a van Hove singularity in metamaterials*. Phys. Rev. B, 88 045407, (2013).

The published results represent some of the previous work accomplished by the present author while attending the University of Alberta. This work focused on single-atom interactions in hyperbolic media. For the sake of brevity, we chose to only include work related to multi-atom interactions within this thesis.

2. QED IN NANOPHOTONIC ENVIRONMENTS

Historically, the success of quantum electrodynamics stems from its accurate calculation of the Lamb shift and the electron's anomalous magnetic dipole moment [29,30]. Precision tests of the fine structure constant α have also led to spectacular agreement between theory and experiment down to the eighth decimal place, making QED one of the most succesful theories in physics [31,32]. The quantization of the electrodynamic field ultimately leads to a non-classical interpretation of electromagnetic radiation. The photon emerges as the quantized excitation of the field characterized through statistical properties, such as Poisson probability distribution of photon detection of laser light as well as sub-Poissonian distributions arising from single photon sources.

2.1 Quantum noise and correlations

In this thesis, we are interested in understanding how nanophotonic environments and quasi-particle excitations within different material systems modify fundamental physical processes. *Quantum noise* is the fundamental origin of many observable properties, arising as a result of the Heisenberg uncertainty principle. Quantum noise is defined as a signal $\hat{E}_i(\mathbf{r},t)$ having zero mean, $\langle\{0\}|\hat{E}_i(\mathbf{r},t)|\{0\}\rangle = 0$, and finite variance,

$$\langle\{0\}|[\Delta\hat{E}_i(\mathbf{r},t)]^2|\{0\}\rangle = \int_0^\infty d\omega \frac{\hbar\omega^2}{\pi\epsilon_o c^2}\mathrm{Im}G_{ii}(\mathbf{r},\mathbf{r},\omega)e^{-i\omega(t-t')} \neq 0, \tag{2.1}$$

characterizing *local* field fluctuations. The expectation value is taken with respect to the zero-particle vacuum state $|\{0\}\rangle$. We have also defined $\Delta\hat{E}(\mathbf{r},t) = \hat{E}(\mathbf{r},t) - \langle\hat{E}(\mathbf{r},t)\rangle$. Quantum noise affects *local* atomic properties like the spontaneous emission

rate or Lamb shift. Non-local interatomic processes are governed by non-local field fluctuations,

$$\langle\{0\}|\Delta\hat{E}_i(\mathbf{r},t)\Delta\hat{E}_j(\mathbf{r}',t')|\{0\}\rangle = \int_0^\infty d\omega \frac{\hbar\omega^2}{\pi\epsilon_o c^2}\mathrm{Im}G_{ij}(\mathbf{r},\mathbf{r}',\omega)e^{-i\omega(t-t')} \neq 0, \qquad (2.2)$$

This quantity defines the correlation between two space-time points $(\mathbf{r},t)$ and $(\mathbf{r}',t')$. The dyadic Green function $\mathbf{G}(\mathbf{r},\mathbf{r}',\omega)$ may be viewed as the photon propagator connecting two spatial locations. Generally, it will composed of both free-space and scattering field contributions. The dyadic Green function is a classical quantity which may be calculated analytically for certain geometries, or numerically for general nanophotonic structures. Ultimately, the control of local and non-local fundamental processes arises directly from controlling local and non-local zero-point fluctuations. Historically, understanding how the presence of a dielectric or conducting surface affects fundamental processes dates back to the early work of Purcell, Mandel, Agarwal and Sipe [33–36].

In this Chapter, we will first discuss the difficulty of quantizing the electrodynamic field in dispersive and absorbing media, followed by a straightforward quantization procedure based on using the fluctuation-dissipation theorem. This sort of quantization procedure has a long history with contributions from many authors [35–39]. In this thesis, we use the modern approach introduced in [40, 41]. Next, we will introduce the minimal coupling and multipolar Hamiltonians that are used to describe the interaction charged particles and the electrodynamic field. Finally, we present a general algorithm for calculating mult-atom processes in hyperbolic media. This formalism is used in Chapter 3 where we study the Super-Coulombic interaction. We emphasize that the proposed algorithm of this chapter allows for a unified framework for calculating a wide-range of 2-body processes including: the resonant dipole-dipole interaction (RDDI) consisting of the cooperative Lamb shift and cooperative decay rate, irreversible energy transfer between molecules (Forster resonance energy transfer) as well as the Casimir-Polder potential between two ground-state or excited-state atoms. Our work is among the first fully-quantized approaches to treat atom-atom

interactions in hyperbolic media in a unified way, where we explicitly avoid ad-hoc assumptions that are typically made within semi-classical theories.

2.2 Second quantization in lossy media

Outline of the problem. The conventional approach, also known as the canonical approach, of quantizing the electrodynamic field in free-space consists of converting the radiation field Hamiltonian

$$H_{rad} = \frac{1}{2}\int d^3r \left[\epsilon_o \mathbf{E}^2(\mathbf{r},t) + \frac{1}{\mu_o}\mathbf{B}^2(\mathbf{r},t)\right] \tag{2.3}$$

into a set of uncoupled harmonic oscillators of the form

$$H_{rad} = \frac{1}{2}\sum_{\sigma}\int d^3k [p^2_{\mathbf{k}\sigma} + \omega^2 q^2_{\mathbf{k}\sigma}] \tag{2.4}$$

where the summation runs over the two transverse polarizations allowed in vacuum. The quantities $p_{\mathbf{k}\sigma}$ and $q_{\mathbf{k}\sigma}$ are analogous to the momentum and position of a classical particle which satisfy the Poisson bracket relation $\{q_{\mathbf{k}\sigma}, p_{\mathbf{k}'\sigma'}\} = \delta(\mathbf{k}-\mathbf{k}')\delta_{\sigma\sigma'}$. The canonical quantization scheme amounts to promoting the Poisson bracket relation to the commutation relation $[\hat{q}_{\mathbf{k}\sigma}, \hat{p}_{\mathbf{k}'\sigma'}] = i\hbar\delta(\mathbf{k}-\mathbf{k}')\delta_{\sigma\sigma'}$. Here, the classical position and momentum functions have been promoted to operators that exist within the Hilbert space $\mathcal{H}$. Defining the annihilation operator $\hat{a}_{\mathbf{k}\sigma} = \sqrt{\frac{\omega}{2\hbar}}(\hat{q}_{\mathbf{k}\sigma} + i\omega^{-1}\hat{p}_{\mathbf{k}\sigma})$, the quantized Hamiltonian for the electrodynamic field takes the form

$$\hat{H}_{rad} = \sum_{\sigma}\int \frac{d^3k}{(2\pi)^3}\hbar\omega_{\mathbf{k}\sigma}\left(\hat{a}^{\dagger}_{\mathbf{k}\sigma}\hat{a}_{\mathbf{k}\sigma} + \frac{1}{2}\right). \tag{2.5}$$

One may then derive the fundamental equal-time commutation relation for the electric and magnetic fields,

$$\left[\hat{\mathbf{E}}(\mathbf{r}), \hat{\mathbf{B}}(\mathbf{r}')\right] = -\frac{i\hbar}{\epsilon_o}\nabla \times \boldsymbol{\delta}(\mathbf{r}-\mathbf{r}'), \tag{2.6}$$

ensuring that we recover the quantized form of Maxwell's equations under the Heisenberg picture. The problem with using this quantization scheme for the case of elec-

trodynamics in an absorbing medium is clear if we write out the energy of the electrodynamic field based on the macroscopic Maxwell's equations,

$$H' = \frac{1}{2}\int d^3r \left[\epsilon_o \mathbf{E}(\mathbf{r},t)\cdot\boldsymbol{\epsilon}\cdot\mathbf{E}(\mathbf{r},t) + \frac{1}{\mu_o}\mathbf{B}^2(\mathbf{r},t)\right] \tag{2.7}$$

Here, we consider the uniaxial permittivity tensor $\boldsymbol{\epsilon}$ and permeability ($\mu = 1$) which are directly related to the response functions of the medium. In frequency space, these functions are generally complex-valued (e.g. $\boldsymbol{\epsilon} = \boldsymbol{\epsilon}' + i\boldsymbol{\epsilon}''$) where the imaginary component describes absorption within the medium. The Hamiltonian H' cannot describe the energy of the system because it is non-hermitian. As a result, the canonical quantization approach outlined above cannot be used.

The quantization of the electrodynamic field inside an absorbing medium is equivalent to the quantization of lossy harmonic oscillators [see Eqn. 2.4]. The question then becomes: how do we quantize a lossy harmonic oscillator? It turns out that this question has been addressed by a wide variety of authors over the years. The modern approach amounts to including an external bath, where the bath provides an additional source of fluctuations ensuring the system satisfies the fluctuation-dissipation theorem assuring the equal-time commutation relations are satisfied. In the next few sections, we outline the steps needed for the quantization of the electrodynamic field in an absorbing and dispersive uniaxial medium.

2.2.1 The fluctuation-dissipation theorem

The fluctuation-dissipation theorem states that the linear response of a system to an applied perturbation is directly related to the system's fluctuation properties in thermodynamic equilibrium. In other words, one may directly relate the relaxation of a system to its fluctuations. This important theorem suggests that if we wish to quantize the electrodynamic field in a dissipative environment, we must add a

fluctuating quantity to ensure the fluctuation-dissipation theorem is satisfied. Using the macroscopic form of Maxwell's equations in frequency-space as a starting point,

$$\nabla \cdot [\epsilon_o \boldsymbol{\epsilon} \mathbf{E}] = \rho_N, \tag{2.8}$$

$$\nabla \cdot \mathbf{B} = 0, \tag{2.9}$$

$$\nabla \times \mathbf{E} = i\omega \mathbf{B}, \tag{2.10}$$

$$\nabla \times \mathbf{B} = -i\omega \mu_o \epsilon_o \boldsymbol{\epsilon} \mathbf{E} + \mu_o \mathbf{j}_N, \tag{2.11}$$

where we introduce ρ_N and $\mathbf{j}_N$ represent the fluctuating (noise) charges and currents. Taking the divergence of the last equation recovers the continuity equation for the noise charge and current: $-i\omega\rho_N + \nabla \cdot \mathbf{j}_N = 0$. Similarly, taking the curl of the third equation, we find the electric field satisfies the vector wave equation,

$$\nabla \times \nabla \times \mathbf{E} - \frac{\omega^2}{c^2} \boldsymbol{\epsilon} \cdot \mathbf{E} = i\mu_o \omega \, \mathbf{j}_N. \tag{2.12}$$

Introducing the classical dyadic Green function, $\mathbf{G}(\mathbf{r}, \mathbf{r}'; \omega)$, defined by the vector wave equation,

$$\nabla \times \nabla \times \mathbf{G}(\mathbf{r}, \mathbf{r}'; \omega) - \frac{\omega^2}{c^2} \boldsymbol{\epsilon} \cdot \mathbf{G}(\mathbf{r}, \mathbf{r}'; \omega) = \delta(\mathbf{r} - \mathbf{r}'), \tag{2.13}$$

as well as the radiation condition $\mathbf{G}(\mathbf{r}, \mathbf{r}'; \omega) \to 0$ as $|\mathbf{r} - \mathbf{r}'| \to 0$, one may formally define a unique solution to the electric field as

$$\mathbf{E}(\mathbf{r}, \omega) = i\mu_o \omega \int d^3\mathbf{r}' \, \mathbf{G}(\mathbf{r}, \mathbf{r}'; \omega) \cdot \mathbf{j_N}(\mathbf{r}', \omega). \tag{2.14}$$

2.2.2 Second quantization

To quantize this theory, the classical noise currents $\mathbf{j}_N(\mathbf{r}, \omega)$ are promoted to quantum operators. For self-consistency, this requires the equal-time commutation relation

$$\left[\hat{\mathbf{E}}(\mathbf{r}), \hat{\mathbf{B}}(\mathbf{r}')\right] = -\frac{i\hbar}{\epsilon_o} \nabla \times \boldsymbol{\delta}(\mathbf{r} - \mathbf{r}'). \tag{2.15}$$

to hold *even* in the presence of dispersive and absorbing environment. Writing the noise current as $\mathbf{j}_N \to \hat{\mathbf{j}}_N(\mathbf{r}, \omega) = C_n \hat{\mathbf{f}}(\mathbf{r}, \omega)$ where C_n is a yet undetermined normal-

ization coefficient and $\hat{\mathbf{f}}(\mathbf{r},\omega)$ represents an operator with yet undetermined commutations relations, the quantized electric and magnetic fields are given by

$$\hat{\mathbf{E}}(\mathbf{r},\omega) = i\mu_o\omega \int d^3\mathbf{r}'\, \mathbf{G}(\mathbf{r},\mathbf{r}';\omega)\cdot\hat{\mathbf{j}}_{\mathbf{N}}(\mathbf{r}',\omega). \tag{2.16}$$

and

$$\hat{\mathbf{B}}(\mathbf{r},\omega) = \mu_o\nabla\times \int d^3\mathbf{r}'\, \mathbf{G}(\mathbf{r},\mathbf{r}';\omega)\cdot\hat{\mathbf{j}}_{\mathbf{N}}(\mathbf{r}',\omega). \tag{2.17}$$

where we used (2.10) to determine the magnetic field. Substituting these equations into the equal-time commutation relation (2.15), we find the noise current operator *must* satisfy the commutation relation[1]

$$\left[\hat{\mathbf{j}}(\mathbf{r},\omega),\hat{\mathbf{j}}^\dagger(\mathbf{r}',\omega')\right] = \frac{\hbar\epsilon_o\omega^2}{\pi}\mathrm{Im}[\boldsymbol{\epsilon}]\delta(\mathbf{r}-\mathbf{r}')\delta(\omega-\omega') \tag{2.18}$$

in agreement with the fluctuation-dissipation commutation relation that is well-known within linear response theory. We have determined the normalization coefficient must be the tensor, $C_n = \sqrt{\frac{\hbar\omega^2}{\mu_o\pi c^2}\mathrm{Im}[\boldsymbol{\epsilon}]}$, while the commutation relation must take the form,

$$[\hat{\mathbf{f}}(\mathbf{r},\omega),\hat{\mathbf{f}}(\mathbf{r}',\omega')] = [\hat{\mathbf{f}}^\dagger(\mathbf{r},\omega),\hat{\mathbf{f}}^\dagger(\mathbf{r}',\omega')] = 0 \tag{2.19}$$

$$[\hat{\mathbf{f}}(\mathbf{r},\omega),\hat{\mathbf{f}}^\dagger(\mathbf{r}',\omega')] = \delta(\mathbf{r}-\mathbf{r}')\delta(\omega-\omega'). \tag{2.20}$$

In macroscopic quantum electrodynamics, these operators represent excitations of collective polaritons of the combined matter and electrodynamic field. The ground state of the polariton operators are defined by

$$\hat{\mathbf{f}}(\mathbf{r},\omega)\,|\{0\}\rangle = 0 \tag{2.21}$$

while the single-excitation Fock state of the polariton is simply

$$|\mathbf{1}(\mathbf{r},\omega)\rangle = \hat{\mathbf{f}}^\dagger(\mathbf{r},\omega)\,|\{0\}\rangle\,. \tag{2.22}$$

[1]Here, we used the identity

$$\int d^3s\frac{\omega^2}{c^2}\mathbf{G}^*(r,s)\cdot\mathrm{Im}[\boldsymbol{\epsilon}]\cdot\mathbf{G}(s,r') = \mathrm{Im}[\mathbf{G}(r,r')]$$

Note that we must also use

$$\mathbf{E}(\mathbf{r}) = \int_{-\infty}^{\infty} d\omega\,\mathbf{E}(\mathbf{r},\omega) = \int_0^\infty d\omega\,\mathbf{E}(\mathbf{r},\omega) + \text{h.c.}$$

where h.c. stands for the hermitian conjugate.

Thus, we interpret $\hat{\mathbf{f}}^\dagger(\mathbf{r},\omega)$ and $\hat{\mathbf{f}}(\mathbf{r},\omega)$ as the creation and annihilation operators of the polaritonic field. Using these definitions, it is straightforward to verify that the quantum average of the noise current vanishes ($\langle\hat{\mathbf{j}}_N\rangle = 0$) as expected. Furthermore, we can explicitly write the noise current operator in cartesian coordinates demonstrating how it depends on different components of the uniaxial permittivity. Recalling the permittivity tensor is defined as $\boldsymbol{\epsilon} = \mathrm{diag}[\epsilon_{xx}, \epsilon_{xx}, \epsilon_{zz}]$, we find

$$\begin{aligned}
\hat{j}_x(\mathbf{r},\omega) &= \sqrt{\frac{\hbar\epsilon_o\omega^2}{\pi}}\sqrt{\mathrm{Im}[\epsilon_{xx}]}\hat{f}_x(\mathbf{r},\omega) \\
\hat{j}_y(\mathbf{r},\omega) &= \sqrt{\frac{\hbar\epsilon_o\omega^2}{\pi}}\sqrt{\mathrm{Im}[\epsilon_{xx}]}\hat{f}_y(\mathbf{r},\omega) \\
\hat{j}_z(\mathbf{r},\omega) &= \sqrt{\frac{\hbar\epsilon_o\omega^2}{\pi}}\sqrt{\mathrm{Im}[\epsilon_{zz}]}\hat{f}_z(\mathbf{r},\omega).
\end{aligned} \tag{2.23}$$

2.3 From the minimal coupling to the multipolar Hamiltonian

It is possible to extend the theory to include the presence of additional charged particles. For a single-charged particle in free-space, the total Hamiltonian is given by the minimal coupling Hamiltonian along with the radiation Hamiltonian defined earlier

$$H = \frac{(\mathbf{p} - e\mathbf{A})^2}{2m} + e\phi + H_{rad}. \tag{2.24}$$

It is straightforward to verify, using Hamilton's equations of motion, that this Hamiltonian returns Maxwell's equations along with the Lorentz force law for a charged particle in the presence of an electric and magnetic field. Upon quantization, the total Hamiltonian may be written as

$$\hat{H} = \hat{H}_o + \hat{H}_{rad} + \hat{H}_{int} \tag{2.25}$$

where

$$\hat{H}_o = \frac{\mathbf{p}^2}{2m} \tag{2.26}$$

$$\hat{H}_{rad} = \int d^3r \int d\omega\, \hat{\mathbf{f}}^\dagger(\mathbf{r},\omega)\cdot\hat{\mathbf{f}}(\mathbf{r},\omega) \tag{2.27}$$

$$\hat{H}_{int} = e\hat{\phi} - \frac{e}{m}\hat{\mathbf{p}}\cdot\hat{\mathbf{A}} + \frac{e^2}{2m}\hat{\mathbf{A}}^{\mathbf{2}}. \tag{2.28}$$

This result resembles the free-space Hamiltonian. Note, however, that the free-space electromagnetic field has been replaced by the polaritonic field with $\hat{\mathbf{f}}^{\dagger}(\mathbf{r},\omega)$ and $\hat{\mathbf{f}}(\mathbf{r},\omega)$ as the creation and annihilation operators. The minimal coupling Hamiltonian for a single particle is easily extended to the general case of N charged particles, where the collection of particles represent a bound atom or molecule. The definition of the scalar and vector potentials follow from the well-known definitions

$$\mathbf{E} = -\nabla\phi - \frac{\partial \mathbf{A}}{\partial t} \tag{2.29}$$

$$\mathbf{B} = \nabla \times \mathbf{A} \tag{2.30}$$

which apply to both classical and quantum fields. In the Coulomb gauge $\nabla\cdot\mathbf{A} = 0$, we would have $\mathbf{E}_L = -\nabla\phi$ and $\mathbf{E}_T = -\partial\mathbf{A}/\partial t$ where the subscripts denote the longitudinal and transverse components of the electric field. In Fourier-space, these equations reduce to simple algebraic relations. While the minimal-coupling Hamiltonian is often used in solid-state physics, it is sometimes more insightful to split the Hamiltonian in terms of multipolar components. Here, we provide the final result which can be obtained through the Power-Zienau-Woolley transformation [41]

$$\hat{f}' = U\hat{f}U^{\dagger} \quad \text{with} \quad U = \exp\left[\frac{i}{\hbar}\int d^3r\ \hat{\mathbf{P}}\cdot\hat{\mathbf{A}}\right] \tag{2.31}$$

where $\hat{\mathbf{P}}$ is the polarization vector defined as

$$\hat{\mathbf{P}}(\mathbf{r}) = \sum_{\alpha} e\mathbf{r}_{\alpha}\int_0^1 ds\delta(\mathbf{r} - \mathbf{r}_a - s\mathbf{r}_{\alpha}). \tag{2.32}$$

The summation runs over a collection of charges and $\mathbf{r}_a$ represents the centre-of-mass position of all charges. Extensive algebraic manipulation yields the multipolar Hamiltonian,

$$\hat{H}_{mult} = \hat{H}'_o + \hat{H}'_{rad} + \hat{H}'_{int} \tag{2.33}$$

where

$$\hat{H}'_o = \frac{\mathbf{p}^2}{2m} + \frac{1}{2\epsilon_o}\int d^3r\, \hat{\mathbf{P}}^2 \tag{2.34}$$

$$\hat{H}'_{rad} = \int d^3r \int d\omega\, \hat{\mathbf{f}}^\dagger(\mathbf{r},\omega)\cdot\hat{\mathbf{f}}(\mathbf{r},\omega) \tag{2.35}$$

$$\hat{H}'_{int} = -\hat{\mathbf{d}}\cdot\hat{\mathbf{E}}(\mathbf{r}_a) - \hat{\mathbf{m}}\cdot\hat{\mathbf{B}}(\mathbf{r}_a) + \frac{e^2}{8m}[\mathbf{r}\times\hat{\mathbf{B}}(\mathbf{r}_a)] + \frac{3}{8m}[\hat{\mathbf{d}}\times\hat{\mathbf{B}}(\mathbf{r}_a)]^2 - \frac{1}{m}\hat{\mathbf{d}}\times\mathbf{p}\cdot\hat{\mathbf{B}}(\mathbf{r}_a) \tag{2.36}$$

is written in the long-wavelength limit. Here $\hat{\mathbf{d}}$ and $\hat{\mathbf{m}}$ correspond to the electric dipole and magnetic dipole moments for an atom with position $\mathbf{r}_a$. For the rest of this thesis, we will only consider electric dipole interactions. For the case of two atoms, the interaction Hamiltonian takes the simplified form

$$H'_{int} = -\hat{\mathbf{d}}_\mathbf{a}\cdot\hat{\mathbf{E}}(\mathbf{r}_a) - \hat{\mathbf{d}}_\mathbf{b}\cdot\hat{\mathbf{E}}(\mathbf{r}_b) \tag{2.37}$$

corresponding to atom A and atom B in position $\mathbf{r}_a$ and $\mathbf{r}_b$ respectively.

2.4 Perturbative theory of dipole-dipole processes

In this thesis, we are interested in understanding the wide range of multi-atom processes that arise for both ground-state and excited-state atoms. A unified approach for calculating all of these processes is based on using the well-established perturbation theory of standard quantum mechanical textbooks. The *transition amplitude*, M_{fi}, between two different states $|i\rangle$ and $|f\rangle$ is given by,

$$M_{fi} = \langle f|\hat{H}_{int}|i\rangle + \sum_I \frac{\langle f|\hat{H}_{int}|I\rangle\langle I|\hat{H}_{int}|i\rangle}{E_I - E_i} + \sum_{I,II}\frac{\langle f|\hat{H}_{int}|II\rangle\langle II|\hat{H}_{int}|I\rangle\langle I|\hat{H}_{int}|i\rangle}{(E_I-E_i)(E_{II}-E_i)} + \sum_{I,II,III}\frac{\langle f|\hat{H}_{int}|III\rangle\langle III|\hat{H}_{int}|II\rangle\langle II|\hat{H}_{int}|I\rangle\langle I|\hat{H}_{int}|i\rangle}{(E_I-E_i)(E_{II}-E_i)(E_{III}-E_i)} + ... \tag{2.38}$$

written here up to fourth order of the perturbation expansion. The summation in the 2^{nd} and higher order terms runs over all possible intermediate states; the summation

can be replaced by an appropriate integral for the case of continuum states. The energy level shift of state $|i\rangle$ is given by

$$\Delta E_i = M_{ii} \tag{2.39}$$

where it is understood that the principal value is taken during the integration of continuum intermediate states. The transition rate from initial state $|i\rangle$ to final state $|f\rangle$ is given by Fermi's Golden rule

$$\Gamma_{i\to f} = \frac{2\pi}{\hbar}\sum_{i,f}|M_{fi}|^2\delta(E_f - E_i) \tag{2.40}$$

where the summation runs over all possible initial and final states.

2.4.1 Identical atoms: resonant dipole-dipole interaction

We now consider the interaction between two identical atoms, labeled atom A and atom B respectively. The probability transition rate from state $|i\rangle$ and $|f\rangle$ is found through (2.40) and leads to the following cooperative decay rate

$$\gamma_{\rm dd} = \frac{2\omega_{\rm a}^2}{\hbar\epsilon_o c^2}\mathbf{d}_{\rm b}\cdot{\rm Im}[\mathbf{G}(\mathbf{r}_{\rm b},\mathbf{r}_{\rm a};\omega_{\rm a})]\cdot\mathbf{d}_{\rm a}. \tag{2.41}$$

Assuming the dipole moments of both atoms are oriented along the same direction, the total decay rate of two identical atoms will be $\gamma_{tot} = \gamma_o \pm \gamma_{\rm dd}$, where γ_o is the bare spontaneous emission rate of atom A (or atom B). The initial state is $|i\rangle = \frac{1}{\sqrt{2}}(|e_{\rm a}\rangle|g_{\rm b}\rangle \pm |g_{\rm a}\rangle|e_{\rm b}\rangle)\otimes|\{0\}\rangle$ and final state $|f\rangle = |g_{\rm a}\rangle|g_{\rm b}\rangle\otimes|\{1\}\rangle$. Note that $|\{1\}\rangle = |\{\mathbf{1}(\mathbf{r},\omega)\}\rangle$ represents the single-photon Fock state with position $\mathbf{r}$ and frequency ω.

The first order dipole-dipole frequency shift of initial state $|i\rangle$ is then found through evaluation of (2.39) which results in a resonant and off-resonant contribution $J_{\rm dd} = J_{\rm dd}^r + J_{\rm dd}^{or}$, specified by

$$J_{\rm dd}^r = -\frac{\omega_{\rm a}^2}{\hbar\epsilon_o c^2}\mathbf{d}_{\rm b}\cdot{\rm Re}[\mathbf{G}(\mathbf{r}_{\rm b},\mathbf{r}_{\rm a};\omega_{\rm a})]\cdot\mathbf{d}_{\rm a} \tag{2.42}$$

and

$$J_{\rm dd}^{or} = \frac{\mu_o}{\hbar\pi}\int_0^\infty {\rm d}\eta\,\eta^2\frac{\omega_{\rm ge}}{\omega_{\rm ge}^2+\eta^2}\mathbf{d}_{\rm b}\cdot\mathbf{G}(\mathbf{r}_{\rm b},\mathbf{r}_{\rm a};i\eta)\cdot\mathbf{d}_{\rm a}. \tag{2.43}$$

where $\omega_{ge} = \omega_g - \omega_e$. These results are in agreement with [42]. We will examine these results thoroughly in the following chapter.

2.4.2 Resonance energy transfer rate

Considering now the interaction between two non-identical atoms or molecules, we now calculate the irreversible and perturbative energy transfer rate from atom A to atom B using (2.40),

$$\Gamma_{\text{ET}} = \frac{2\pi}{\hbar^2}\frac{\omega_{\text{a}}^4}{\epsilon_o^2 c^4}|\mathbf{d}_{\text{b}} \cdot \mathbf{G}(\mathbf{r}_{\text{a}}, \mathbf{r}_{\text{b}}; \omega_{\text{a}}) \cdot \mathbf{d}_{\text{a}}|^2 \delta(\omega_{\text{a}} - \omega_{\text{b}}) \tag{2.44}$$

where we performed the calculation for the initial state $|i\rangle = |e_{\text{a}}\rangle\,|g_{\text{b}}\rangle \otimes |\{0\}\rangle$, with atom A in the excited-state and atom B in the ground-state, and final state $|f\rangle = |g_{\text{a}}\rangle\,|e_{\text{b}}\rangle \otimes |\{0\}\rangle$ where both atoms are in the ground-state. In both cases, the electrodynamic field is assumed to be in the vacuum state.

2.4.3 Excited-state Casimir-Polder Potential

The associated energy-level shift between two non-identical atoms, given that one is prepared in the excited-state and the other remains in its ground state, is given by the Casimir-Polder potential: [43]

$$U_{\text{eg}}(r) = U_{\text{eg}}^{r}(r) + U_{\text{eg}}^{or}(r) \tag{2.45}$$

where the resonant component is

$$U_{\text{eg}}^{r}(r) = -\frac{\omega_{\text{a}}^4|\mathbf{d}_{\text{a}}|^2}{3\epsilon_o^2 c^4}\alpha_{\text{b}}^{g}(\omega_{\text{a}})\text{Re}\{\text{Tr}[\mathbf{G}(\omega_{\text{a}})\mathbf{G}(\omega_{\text{a}})]\} \tag{2.46}$$

and off-resonant component is given by

$$U_{\text{eg}}^{or}(r) = \frac{-\hbar\mu_o^2}{2\pi}\int_0^\infty d\eta\,\eta^4\alpha_{\text{a}}^{e}(i\eta)\alpha_{\text{b}}^{g}(i\eta)\text{Tr}[\mathbf{G}(i\eta)\mathbf{G}(i\eta)]. \tag{2.47}$$

$\alpha_{\text{a}}^{k}(\omega)$ is the isotropic electric polarizability of atom A in the kth energy eigenstate, defined as

$$\alpha_{\text{a}}^{k}(\omega) = \frac{2}{3\hbar}\sum_m \frac{\omega_{mk}|\,\langle k|\hat{\mathbf{d}}_{\text{a}}|m\rangle\,|^2}{\omega_{mk}^2 - \omega^2 - i\omega 0^+}. \tag{2.48}$$

For this calculation, we had to use the *fourth*-order transition matrix element (2.38).

2.4.4 Ground-state Casimir-Polder potential

The Casimir Polder potential (sometimes referred to as the Van der Waals interaction) between two ground-state atoms is [44]

$$U_{\mathrm{gg}}(r) = -\frac{\hbar\mu_o^2}{2\pi}\int_0^\infty d\eta\,\eta^4\alpha_{\mathrm{a}}^g(i\eta)\alpha_{\mathrm{b}}^g(i\eta)\mathrm{Tr}[\mathbf{G}(i\eta)\mathbf{G}(i\eta)] \tag{2.49}$$

This result is applicable in both the retarded and non-retarded regimes. We have dropped the spatial coordinate dependence for the Green function in (2.46), (2.47) and (2.49). Again, we used the *fourth*-order transition matrix element (2.38). Note that this result is similar to the off-resonant potential (2.47). Strictly speaking, the Van der Waals potential refers to the r^{-6} spatial scaling between two ground-state atoms, which occurs in the non-retarded, near-field limit $r \ll \lambda$. Quantum electrodynamic calculations by Casimir and Polder showed that the spatial scaling in the retarded limit ($r \gg \lambda$) changes to r^{-7}.

Applicability of perturbation theory. The perturbation theory formalism used in this chapter is strictly applicable for the case of finite absorption with a sufficiently large interatomic separation distance. This is in agreement with our simulations for practical experimental systems such as plasmonic super-lattices and hyperbolic meta-surfaces as we shall show in the following chapter. For the case of low-losses and short separation distances, a non-perturbative approach will be required to treat the dipole-dipole interaction in a self-consistent manner. We present one such non-perturbative approach in the second half of this thesis.

In the following chapter, we will take the transition frequency of atom A to be $\omega_{\mathrm{a}}/2\pi = 500$ THz, while the transition frequency of atom B will be $\omega_{\mathrm{b}}/2\pi = 460$ THz for all simulations.

Chapter addendum: Constitutive Relations

The response of a collection of charged particles must be linear and causal in the linear response limit hence the constitutive relation required for quantization of a dispersive and absorbing medium must generally given by

$$\mathbf{P}(\mathbf{r},t) = \epsilon_o \int_{-\infty}^{\infty} d\tau \int d^3r' \, \boldsymbol{\chi}(\mathbf{r},\mathbf{r}',\tau) \cdot \mathbf{E}(\mathbf{r}',t-\tau) + \mathbf{P}_N(\mathbf{r},t) \tag{2.50}$$

where $\boldsymbol{\chi}$ corresponds to the electric susceptibility and $\mathbf{P}_N$ is a noise polarization term. In this description the susceptibilities are required to provide the total polarization of a medium at point $\mathbf{r}$ and time t due to an applied electric field $\mathbf{E}$ applied at the advanced time τ. The integration over all positions and time provides the most complete description demonstrating how the interaction over all space and time results in the final polarization at point $\mathbf{r}$ and time t. Note that causality restricts the space-time points that can affect the final polarization by

$$\chi(\mathbf{r},\mathbf{r}',\tau) = 0 \quad \text{for} \quad |\mathbf{r}-\mathbf{r}'| > c\tau \tag{2.51}$$

Thus effectively restricting the interactions to time-like or light-like separations between charged particles. This condition ensures $\boldsymbol{\chi}$ is a retarded response function. In this thesis, we focus on *local* media with the property $\chi(\mathbf{r},\mathbf{r}',\tau) = \chi(\mathbf{r},t-t')\delta(\mathbf{r}-\mathbf{r}')$ so that

$$\mathbf{P}(\mathbf{r},t) = \epsilon_o \int_{-\infty}^{\infty} d\tau \, \boldsymbol{\chi}(\mathbf{r},\tau) \cdot \mathbf{E}(\mathbf{r},t-\tau) + \mathbf{P}_N(\mathbf{r},t) \tag{2.52}$$

The causality requirement thus simplifies to $\boldsymbol{\chi}(\mathbf{r},t) = 0$ for $\tau < 0$. In other words, $\boldsymbol{\chi}(\mathbf{r},t) \equiv \Theta(\tau)\boldsymbol{\chi}(\mathbf{r},\tau)$, where $\Theta(\tau)$ represents the Heaviside function, effectively changing the integration limits from 0 to infinity. This implies the polarization depends only on the past history of the electromagnetic field as represented by the convolution integral. It is possible to simplify the constitutive relations by working in Fourier space

$$\mathbf{P}(\mathbf{r},\omega) = \epsilon_o \chi(\mathbf{r},\omega) \cdot \mathbf{E}(\mathbf{r},\omega) + \mathbf{P}_N(\mathbf{r},\omega) \tag{2.53}$$

The displacement field is then written as

$$\mathbf{D}(\mathbf{r},\omega) = \epsilon_o \mathbf{E}(\mathbf{r},\omega) + \mathbf{P}(\mathbf{r},\omega) = \epsilon_o \boldsymbol{\epsilon} \cdot \mathbf{E}(\mathbf{r},\omega) + \mathbf{P}_N(\mathbf{r},\omega) \tag{2.54}$$

where we have defined the permittivity tensor as $\boldsymbol{\epsilon} = 1 + \boldsymbol{\chi}$. The causality relation implies in the Kramers-Kronig relations for the susceptibility,

$$\mathrm{Re}[\boldsymbol{\chi}] = \frac{1}{\pi} P.V. \int_{-\infty}^{\infty} d\omega' \frac{\mathrm{Im}\boldsymbol{\chi}(\omega')}{\omega' - \omega}, \text{ and } \mathrm{Im}[\boldsymbol{\chi}] = -\frac{1}{\pi} P.V. \int_{-\infty}^{\infty} d\omega' \frac{\mathrm{Re}\boldsymbol{\chi}(\omega')}{\omega' - \omega} \tag{2.55}$$

where *P.V.* denotes the principal value of the integral. One may use this condition to ensure experimental response functions are physical. Similarly, one may determine the real components of the response function based on measurements of the absorption (imaginary) components.

3. SUPER-COULOMBIC DIPOLE-DIPOLE INTERACTIONS IN HYPERBOLIC MEDIA

In the following, we provide the first main result of this thesis using the formalism of the previous chapter. The results of this Chapter have been published in the open-access journal, *Nature Communications* [45], re-published with suitable editing with permission from the Nature Publishing Group.

3.1 Motivation for studying dipole-dipole interactions

Dipole-dipole interactions (DDI) are instrumental in mediating entanglement, superradiance, as well as coherent coupling between single molecules or atoms [46–52]. There are two fundamental ways of controlling the strength and length scales of dipole-dipole interactions. The first method involves tuning intrinsic atomic properties such as transition dipole moments and transition frequencies (cf. highly-excited Rydberg atoms and superconducting qubits [52–54]). The second method tunes the properties of the quantum electrodynamic vacuum, typically achieved through cavities, waveguides or photonic crystals [55–58]. Conventional electrodynamic approaches typically rely on resonant effects that require huge quality factors along with extensive nanofabrication steps. It is an open question, however, whether there exists alternative non-resonant techniques for controlling dipole-dipole interactions that would be robust to broad spectral lineshapes of atoms or molecules with possible room temperature applications. The main purpose of this chapter is to present work related to this new avenue of research.

In this chapter, we reveal a class of singular excited-state atom-atom interactions that can occur in natural and artificial media with hyperbolic dispersion. Unlike the above mentioned approaches which engineer radiative coupling, we show that the ho-

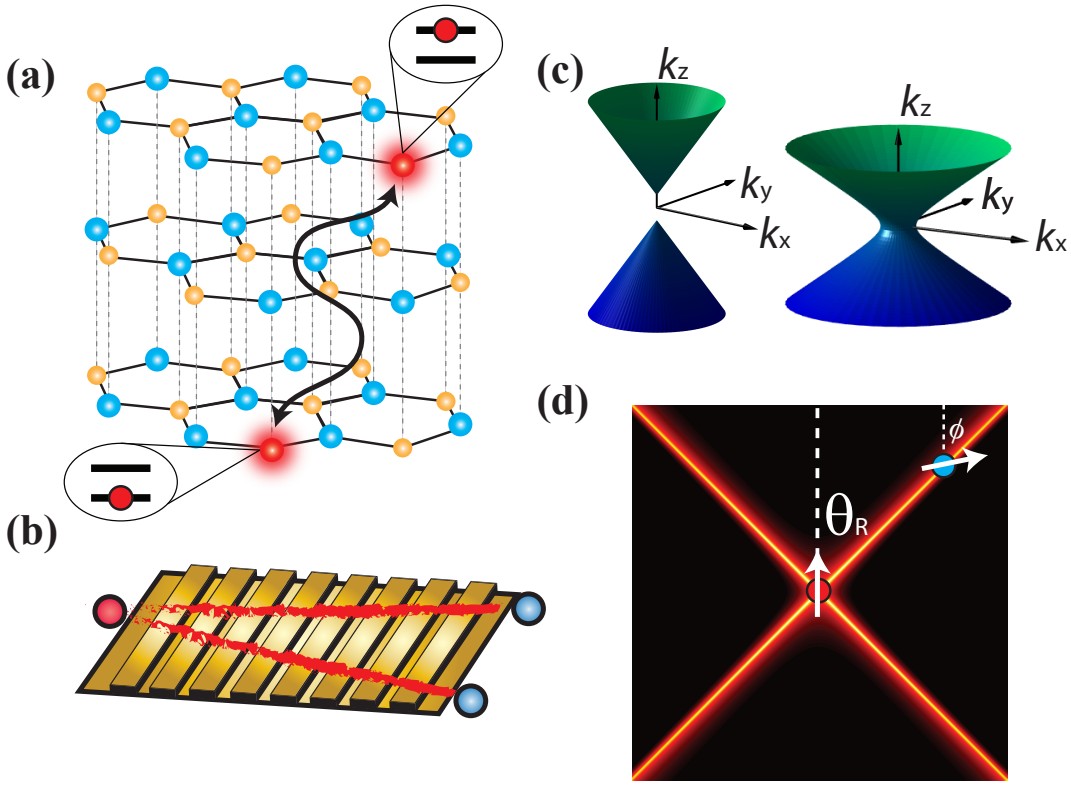

Fig. 3.1. **Overview of Super-Coulombic interaction.** The proposed long-range Super-Coulombic dipole-dipole interaction may be observed (a) between single-photon defect centers in natural hyperbolic media (e.g. h-BN, Bi_2Se_3, Bi_2Te_3) or (b) between ultra-cold atoms trapped above a hyperbolic meta-surface. (c)-(d) The Super-Coulombic interaction occurs over a broad range of frequencies along the resonance angle of a hyperbolic medium and causes the effective interaction distance to approach zero irrespective of the physical distance.

mogeneous hyperbolic medium itself fundamentally alters the Coulombic near-field. The resultant divergant long-range interaction, referred to as a Super-Coulombic interaction, is described by an effective interaction distance that goes to zero ($r_e \to 0$) along a material-dependent resonance angle. We show that this interaction affects the entire landscape of real photon and virtual photon phenomena such as the cooperative Lamb shift, the cooperative decay rate, resonance energy transfer rates and frequency shifts as well as resonant interatomic forces. While we find that the sin-

gularity is curtailed by material absorption, it still allows for interactions with much larger magnitudes and longer ranges than those found in any conventional media. We also show that atoms in a hyperbolic medium will exhibit a strong orientational dependence that can effectively switch the dipolar interaction off or on, providing an additional degree of freedom to control dipole-dipole interactions. Our investigation reveals a marked contrast between ground-state and excited-state interactions which can be used to distinguish the Super-Coulombic effect in experiment. Finally, we provide a unified perspective for controlling dipole-dipole interactions on multiple experimental platforms for hyperbolic media including plasmonic super-lattices, hyperbolic metasurfaces, and natural hyperbolic media such as hexagonal boron nitride (h-BN).

We emphasize that the materials platform we introduce in this chapter to enhance dipole-dipole interactions is fundamentally different from the cavity QED [59, 60] or waveguide QED regimes [50, 61–63]. We do not rely on atom confinement [47, 50–52, 60], cavity resonances or modal effects such as the quasi-TEM mode in circuit QED [62], the band-edge slow light as in PhC waveguides [50, 51, 64], the low mode volume of plasmonic waveguides [63, 65], or the infinite phase velocity at the cut-off frequency of ENZ waveguides [55, 66]. We also stress that the Super-Coulombic effect engineers the conventional non-radiative (longitudinal) near-fields as opposed to radiative (transverse) modes and will occur over a broad range of frequencies due to the broadband nature of the hyperbolic dispersion relation [67–70]. Fig. 3.1 depicts a schematic of the proposed Super-Coulombic dipole-dipole interaction using hexagonal Boron Nitride (h-BN) [71–74] and two dopant atoms. In the infrared spectral range, h-BN behaves like a hyperbolic uniaxial medium that supports extraordinary waves satisfying the hyperbolic dispersion relation $k_x^2/\epsilon_z + k_z^2/\epsilon_x = \omega^2/c^2$ whenever $\epsilon_x\epsilon_z < 0$.

3.2 Dipole-dipole interactions in hyperbolic media

By using the QED theory of hyperbolic media developed in the previous chapter, we now calculate the dipole-dipole interactions between two neutral, non-magnetic atoms in a hyperbolic medium. We focus on dipolar interactions where the electrodynamic field is initially prepared in the vacuum state $|\{0\}\rangle$. The results of this chapter use the multipolar Hamiltonian for two neutral atoms [positions $\mathbf{r}_j$, transition frequencies ω_j and transition electric dipole moments $\hat{\mathbf{d}}_j$ $(j = a, b)$]. We emphasize that the QED theory captures both ground-state, ground-state interactions and excited-state, ground-state interactions which a semi-classical approach cannot. In the following, we distinguish between *identical* and *non-identical* dipole-dipole processes. This distinction is useful because they have fundamentally different spatial scaling laws.

3.2.1 Interaction between 2 identical atoms

We now present the dominant dipole-dipole process for two identical atoms having equal dipole moment magnitudes and transition frequencies. Due to the excited-state degeneracy, we take the initial state of the atomic system to be prepared in the symmetric or anti-symmetric state, $|i\rangle = \frac{1}{\sqrt{2}}(|e_{\rm a}\rangle\,|g_{\rm b}\rangle \pm |g_{\rm a}\rangle\,|e_{\rm b}\rangle)$.

Resonant dipole-dipole interaction Based on the perturbative theory introduced in the previous chapter, we introduce the (non-hermitian) resonant dipole-dipole interaction (RDDI),

$$V_{\rm dd} = \hbar\left(J_{\rm dd} - i\frac{\gamma_{\rm dd}}{2}\right) = -\frac{\omega_{\rm a}^2}{\epsilon_o c^2}\mathbf{d}_{\rm b}\cdot\mathbf{G}(\mathbf{r}_{\rm b},\mathbf{r}_{\rm a};\omega_{\rm a})\cdot\mathbf{d}_{\rm a}, \tag{3.1}$$

where $\mathbf{d}_j = \langle g_j|\hat{\mathbf{d}}_j|e_j\rangle$ is the transition dipole moment of atom j, assumed to be real. $J_{\rm dd}$ is the cooperative Lamb shift (also known as the virtual photon exchange interaction) and $\gamma_{\rm dd}$ is the cooperative decay rate commonly associated with super-

radiant or subradiant effects. Our result for the resonant dipole-dipole interaction in a hyperbolic medium ($\boldsymbol{\epsilon} = \mathrm{diag}[\epsilon_x, \epsilon_x, \epsilon_z]$) is

$$V_{\mathrm{dd}} = \frac{e^{ik_o r_e}}{4\pi\epsilon_o\sqrt{\epsilon_x} r_e^3}\mathbf{d}_{\mathrm{b}} \cdot \left[(1 - ik_o r_e)\boldsymbol{\kappa}_{\mathrm{nf}} - k_o^2 r_e^2 \boldsymbol{\kappa}_{\mathrm{ff}}\right] \cdot \mathbf{d}_{\mathrm{a}} + \tilde{V}_{\mathrm{dd}}^{eo} \tag{3.2}$$

valid when $\mathbf{r}_{\mathrm{a}} \neq \mathbf{r}_{\mathrm{b}}$. The first term arises exclusively from extraordinary waves following a hyperbolic dispersion while the second term $\tilde{V}_{\mathrm{dd}}^{eo}$ arises from a combination of ordinary and extraordinary waves. Here, we have defined the near-field and far-field dipole orientation matrix factors $\boldsymbol{\kappa}_{\mathrm{nf}} = \epsilon_x\epsilon_z(\boldsymbol{\epsilon}^{-1} - 3(\boldsymbol{\epsilon}^{-1} \cdot \mathbf{r})(\boldsymbol{\epsilon}^{-1} \cdot \mathbf{r})/(\mathbf{r} \cdot \boldsymbol{\epsilon}^{-1} \cdot \mathbf{r}))$ and $\boldsymbol{\kappa}_{\mathrm{ff}} = \epsilon_x\epsilon_z(\boldsymbol{\epsilon}^{-1} - (\boldsymbol{\epsilon}^{-1} \cdot \mathbf{r})(\boldsymbol{\epsilon}^{-1} \cdot \mathbf{r})/(\mathbf{r} \cdot \boldsymbol{\epsilon}^{-1} \cdot \mathbf{r}))$ respectively. Equation (3.2) reduces to the vacuum RDDI expression when $\epsilon_x = \epsilon_z = 1$, which is applicable both in the retarded ($r \gg \lambda$) and non-retarded ($r \ll \lambda$) regimes. The most unique aspect of dipole-dipole interactions inside a uniaxial media is the divergence that is predicted from the first term only when the hyperbolic condition ($\epsilon_x\epsilon_z < 0$) is satisfied. In the ideal lossless limit, we find that the effective interaction distance between two atoms, $r_e = \sqrt{\epsilon_x\epsilon_z(\mathbf{r} \cdot \boldsymbol{\epsilon}^{-1} \cdot \mathbf{r})} = r\sqrt{\epsilon_z \sin^2\theta + \epsilon_x \cos^2\theta}$, tends towards the limit

$$r_e \to 0 \ \text{ as } \ \theta \to \theta_{\mathrm{R}} = \tan^{-1}\sqrt{-\epsilon_x/\epsilon_z}. \tag{3.3}$$

This Super-Coulombic effect results in the divergence of the dipole-dipole interaction strength $|V_{\mathrm{dd}}|/\hbar$ along the resonance angle θ_{R}, defined with respect to the optic axis.

Atoms in a hyperbolic medium will then have an associated cooperative Lamb shift (CLS) and cooperative decay rate (CDR)

$$J_{\mathrm{dd}} \approx \frac{\sqrt{\epsilon_x}\epsilon_z}{4\pi\hbar\epsilon_o r_{\mathrm{e}}^3}\,\mathbf{d}_{\mathrm{b}} \cdot [\boldsymbol{\epsilon}^{-1} - 3\frac{(\boldsymbol{\epsilon}^{-1} \cdot \mathbf{r})(\boldsymbol{\epsilon}^{-1} \cdot \mathbf{r})}{\mathbf{r} \cdot \boldsymbol{\epsilon}^{-1} \cdot \mathbf{r}}] \cdot \mathbf{d}_{\mathrm{a}} \tag{3.4}$$

$$\gamma_{\mathrm{dd}} \approx \frac{\omega_{\mathrm{a}}^3\sqrt{\epsilon_x}\epsilon_z}{3\pi\hbar\epsilon_o c^3}\mathbf{d}_{\mathrm{b}} \cdot \boldsymbol{\epsilon}^{-1} \cdot \mathbf{d}_{\mathrm{a}} \tag{3.5}$$

in the limit $\theta \to \theta_{\mathrm{R}}$. Equations (3.4) and (3.5) are the dominant factors of the extraordinary wave contribution only.

We now contrast the scaling of cooperative Lamb shift (CLS) with distance when mediated by hyperbolic media as opposed to vacuum modes. In vacuum, for separation distances much larger than the transition wavelength, the CLS scales as

$J_{\rm dd} \sim \gamma_o \cos(k_o r)/(k_o r)$ and becomes much smaller than the free-space spontaneous emission rate (γ_o). On the other hand, for distances much smaller than the wavelength, the CLS scales as $J_{\rm dd} \sim \gamma_o/(k_o r)^3$, which implies that it can become much larger than the spontaneous emission rate. In contrast, the cooperative Lamb shift in a hyperbolic medium is dependent on r_e^{-3}, $J_{\rm dd} \sim \gamma_o/(k_o r_e)^3$, for all interatomic distances. The material-dependent factor $1/r_e^3$ diverges in the lossless case and therefore results in giant cooperative Lamb shifts for short and large interatomic distances.

This marked contrast is also revealed in the cooperative decay rate (CDR). At large distances, the CDR in vacuum scales as $\gamma_{\rm dd} \sim \gamma_o \sin(k_o r)/(k_o r)$, therefore becoming weak for distances much larger than the wavelength. For distances much smaller than the wavelength, the CDR becomes independent of position, $\gamma_{\rm dd} \sim \gamma_o$, and remains on the order of the free space spontaneous emission rate. In contrast, the cooperative decay rate in a hyperbolic medium along the resonance angle is not dependent on the effective interaction distance r_e, and instead it depends crucially on the orientation angle ϕ of the dipoles, $\gamma_{\rm dd} \sim \gamma_o(\epsilon_z/\sqrt{\epsilon}_x \sin^2\phi + \sqrt{\epsilon}_x \cos^2\phi)$. When both dipoles are oriented perpendicular to the optic axis ($\phi = \pi/2$), there exists a unique wavelength when the medium can achieve an anisotropic epsilon-near-zero (ENZ) medium ($\epsilon_x \to 0$ and $\epsilon_z \neq 0$) resulting in a divergent cooperative decay rate. Surprisingly, the effect is independent of interatomic distance. When both dipoles are parallel to the optic axis ($\phi = 0$), the same anisotropic ENZ condition gives a null CDR between the two atoms, independent of interatomic distance.

Role of material absorption

We will now consider the role of material absorption ($\epsilon_x = \epsilon_x' + i\epsilon_x''$ and $\epsilon_z = \epsilon_z' + i\epsilon_z''$) on atom-atom interactions in a hyperbolic medium. We find that the effective interaction distance is not zero and tends to the finite value $|r_e| \to |r| \left[\frac{\epsilon_z''|\epsilon_x'| + \epsilon_x''|\epsilon_z'|}{|\epsilon_x'| + |\epsilon_z'|}\right]^{1/2}$ as $\theta \to \theta_{\rm R}$. This curtails the singularity of the hyperbolic dipolar interaction but nevertheless allows for very large interaction strengths compared to conventional media whenever

$|r_e|/|r| < 1$ is satisfied. Material absorption will also modify the spatial scaling laws of the RDDI in eqn. (5.6) so that both the cooperative decay rate and Lamb shift will scale as r_e^{-3}. Another consequence of material absorption on resonant dipole-dipole interactions is in the transition from non-retarded (r^{-3}) to retarded (r^{-1}) interactions. In vacuum, the transition occurs when the interatomic separation distance is on the order of wavelength, $(\omega/c)r \sim 1$. In an ideal lossless hyperbolic medium, this transition from near-field to far-field does not occur since the effective separation distance approaches zero, $r_e \to 0$ specifically along the resonance angle of a hyperbolic medium. Therefore we find that RDDI should scale with the characteristic power law of near-field (longitudinal) non-radiative interactions (r^{-3}) for all interatomic distances. Once material absorption is included, the transition is expected to occur approximately when $(\omega/c)|r_e| \sim 1$. The dipolar interactions will transition from the power law (r_e^{-3}) to the exponential scaling law ($e^{-(\omega/c)\mathrm{Im}[r_e]}$) which is valid at large interatomic distances.

Fig. 3.2 shows the result of the cooperative Lamb shift and decay rate for two z-oriented dipoles in a hyperbolic medium that includes material absorption. We compare the resonant dipole-dipole interactions with the conventional results of a lossy dielectric and vacuum. Note that the RDDI peaks near the resonance angle θ_{R} as predicted theoretically. The spatial field plots in the insets clearly demonstrate the distinguishing features of the RDDI in a hyperbolic medium compared to vacuum. Fig. 3.2-c and Fig. 3.2-d demonstrate the r_e^{-3} Super-Coulombic spatial dependence along the resonance angle. Note that the sign of the interaction is dependent on the orientation of the dipoles as well as the relative position of the dipoles within the hyperbolic medium.

Orientational dependence

We now turn to the unique orientational dependence of the RDDI between two atoms positioned along the resonance angle θ_{R}. In Fig. 3.3, we plot the normalized

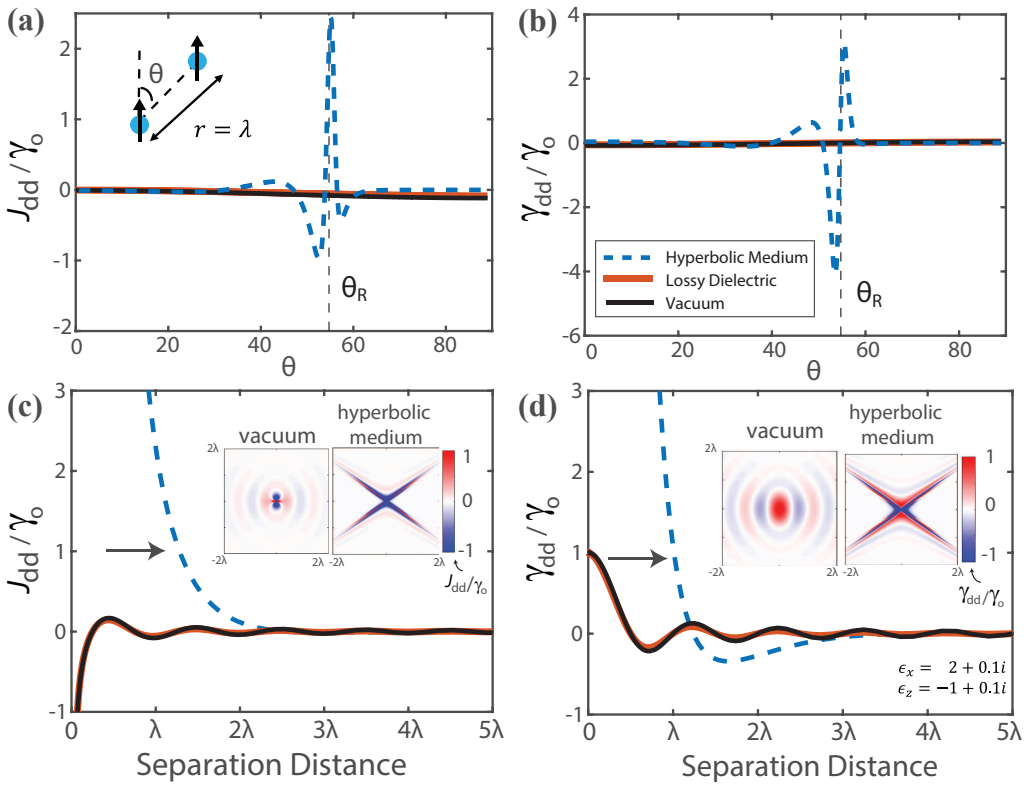

Fig. 3.2. **Manifestation of Super-Coulombic interaction in hyperbolic media.** Angular dependence of (a) cooperative Lamb shift (CLS) $J_{\rm dd}$ and (b) cooperative decay rate (CDR) $\gamma_{\rm dd}$ for two z-oriented dipoles in a lossy hyperbolic medium, lossy dielectric, and vacuum. The CLS and CDR have large peaks near the resonance angle of the hyperbolic medium indicative of the super-Coulombic interaction, even for distances of a wavelength. Comparison of (c) CLS and (d) CDR at the resonance angle versus interatomic separation distance. The CLS and CDR both obey a $1/r^3$ power law dependence in the near-field due to the inclusion of absorption in the hyperbolic medium. Note that the giant interactions start occuring at distances on the order of a wavelength (arrows) even in the presence of material absorption which is in stark contrast to vacuum. The insets show the contrasting spatially-resolved (c) CLS and (d) CDR for vacuum and for a hyperbolic medium.

cooperative Lamb shift of two atoms a full wavelength apart ($r = \lambda$) as a function of dipole orientation angle ϕ. The cooperative Lamb shift has a minimum when $\phi = \theta_{\rm R}$

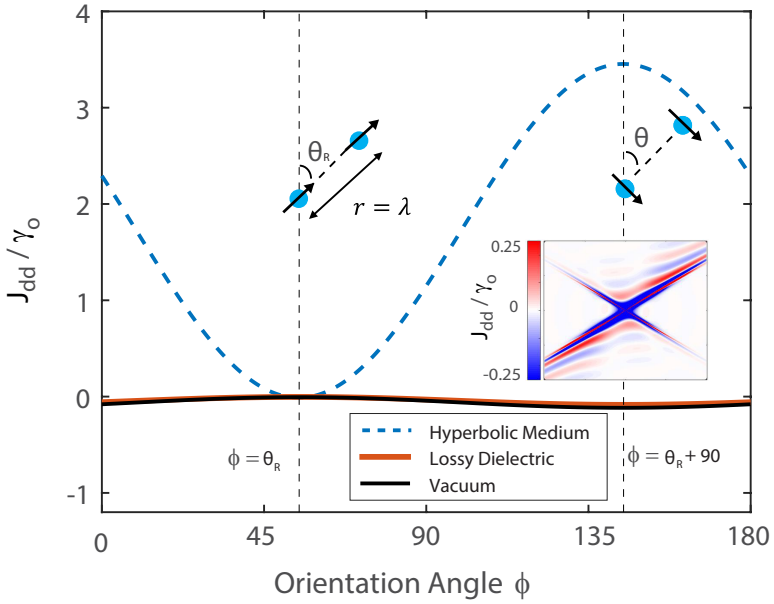

Fig. 3.3. **Unique orientational dependence of RDDI in hyperbolic media.** The plot shows CLS versus orientation angle ϕ for two dipoles positioned along the resonance angle. The cooperative Lamb shift is minimized when the dipoles are collinear with the the resonance angle, and it is maximized when the dipoles are perpendicular to the resonance angle. The inset shows the asymmetric nature of the spatially-resolved $J_{\rm dd}/\gamma_o$ when the dipoles are orthogonal to the resonance angle.

and a maximum when $\phi = \theta_{\rm R} + \pi/2$. Assuming that $|\epsilon'| = |\epsilon'_x| \approx |\epsilon'_z|$, $\epsilon'' = \epsilon''_x \approx \epsilon''_z$, and $\epsilon'' \ll |\epsilon'|$, we find that the ratio between the maximum and minimum is

$$\frac{J_{\rm dd}(\phi = \theta_{\rm R} + \pi/2)}{J_{\rm dd}(\phi = \theta_{\rm R})} \approx -\frac{3}{2}\left(\frac{\epsilon'}{\epsilon''}\right)^2 \tag{3.6}$$

showing that it is proportional to the square of the figure of merit of the hyperbolic medium. In Fig. 3.3, we use the full Green's function to calculate the orientational dependence of the dipolar interaction in a hyperbolic medium with material absorption, and find excellent agreement with the analytical expression.

3.2.2 Interaction between 2 non-identical atoms

We now consider 2^{nd} order super-coulombic QED interactions arising from initial state preparation consisting of atom A in its excited state and atom B in its ground state, $|i\rangle = |e_{\rm a}\rangle\,|g_{\rm b}\rangle$.

Förster resonance energy transfer

In the weak-coupling regime, an incoherent and irreversible resonance energy transfer takes place transferring a photon from atom A to atom B. This process is known as Förster resonance energy transfer (FRET) and, as mentioned in the main abstract of the thesis, this process has many applications across all sciences. The transfer rate is calculated using Fermi's golden rule is $\Gamma_{\rm ET} = 2\pi\hbar^{-1}|V_{\rm dd}|^2\delta(\hbar\omega_{\rm a}-\hbar\omega_{\rm b})$. Along the resonance angle, FRET is mediated by hyperbolic modes and the rate is given by

$$\Gamma_{\rm ET} \approx \frac{2\pi}{\hbar}\frac{|\mathbf{d}_{\rm b}\cdot\boldsymbol{\kappa}_{\rm nf}\cdot\mathbf{d}_{\rm a}|^2}{(4\pi\epsilon_o)^2|\epsilon_x||r_e|^6}\delta(\hbar\omega_{\rm a}-\hbar\omega_{\rm b}) \tag{3.7}$$

which shows a r_e^{-6} scaling dependence and giant enhancement – the key signature of second order Super-Coulombic interactions in hyperbolic media.

Casimir-Polder potential

In addition to the FRET rate, there is also a predicted frequency shift that comes from the initial state preparation $|i\rangle = |e_{\rm a}\rangle\,|g_{\rm b}\rangle$. This is the excited-state Casimir-Polder potential, $U_{\rm eg}(r) = U^r_{\rm eg}(r) + U^{or}_{\rm eg}(r)$, composed of a resonant and off-resonant contribution. The resonant excited-state Casimir-Polder potential is of the form $U^r_{\rm eg}(r) = -\frac{|\mathbf{d}_{\rm a}|^2\omega_{\rm a}^4}{3\epsilon_o^2c^4}\alpha_{\rm b}(\omega_{\rm a}){\rm Re}\{{\rm Tr}[\mathbf{G}(\mathbf{r}_{\rm b},\mathbf{r}_{\rm a};\omega_{\rm a})\mathbf{G}(\mathbf{r}_{\rm a},\mathbf{r}_{\rm b};\omega_{\rm a})]\}$ [43]. We therefore predict that the excited-state energy potential will also diverge with a r_e^{-6} scaling dependence similar to the FRET rate.

Fig. 3.4 shows the full numerical results for the 2nd order dipole-dipole interactions in a lossy hyperbolic medium, a lossy dielectric, and vacuum. In the non-

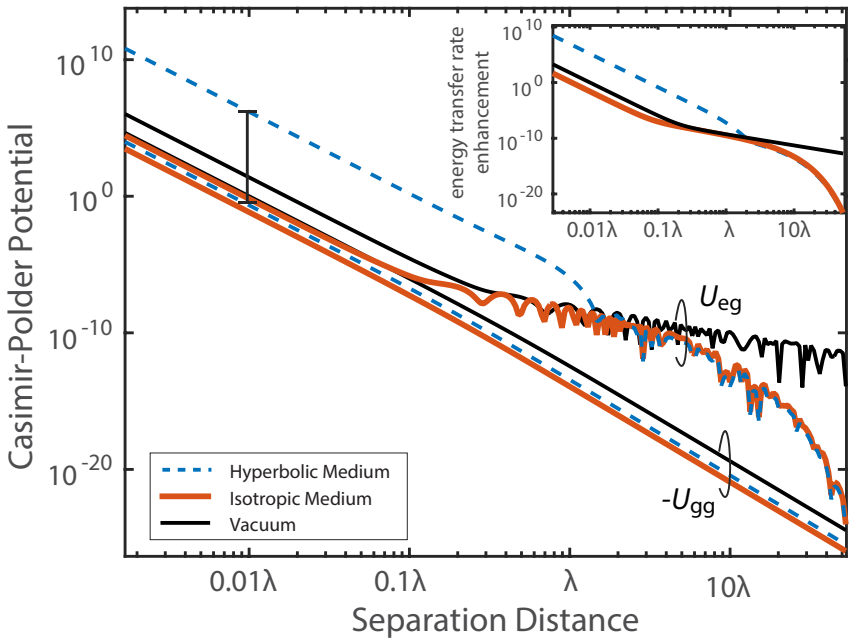

Fig. 3.4. **Ground-state and excited-state Casimir-Polder interaction energy in hyperbolic media.** Casimir-Polder interaction energy between two ground-state atoms (U_{gg}) and between an excited-state atom and ground-state atom (U_{eg}) show fundamental differences when interacting in hyperbolic medium. $U_{eg} >> U_{gg}$ since resonant interactions lie completely within the bandwidth of hyperbolic dispersion and are strongly enhanced. The results are normalized to U_{gg} in vacuum, evaluated at the near-field interatomic distance of $r_o = \lambda/100$. The inset shows the giant enhancement of the FRET rate, Γ_{ET}, as compared to vacuum. The FRET rate is normalized to the vacuum energy transfer rate evaluated at r_o.

retarded regime ($r \ll \lambda$), we clearly see the effect of the Super-Coulombic interaction which results in a large enhancement of the dipolar interactions U_{eg} and Γ_{ET} (shown in inset). The super-Coulombic enhancement occurs only along the asymptotes of the hyperboloid and is unrelated to the suppression of FRET rate of an ensemble of emitters near a conventional metallic surface or hyperbolic medium [75–77].

It is interesting that the dispersive Van der Waals interaction between two ground state atoms does not diverge in a hyperbolic medium. Using fourth order perturbation theory [44], the interaction energy between two ground-state atoms is given

by $U_{\rm gg}(\mathbf{r}_{\rm a},\mathbf{r}_{\rm b}) = \frac{-\hbar\mu_o^2}{2\pi}\int_0^\infty d\eta\eta^4\alpha_{\rm a}(i\eta)\alpha_{\rm b}(i\eta){\rm Tr}[\mathbf{G}(\mathbf{r}_{\rm b},\mathbf{r}_{\rm a};i\eta)\mathbf{G}(\mathbf{r}_{\rm a},\mathbf{r}_{\rm b};i\eta)]$, where $\alpha_{A,B}(\omega)$ is the isotropic electric polarizability of atom A or B. In the non-retarded limit, the dominant contribution is given by

$$U_{\rm gg} \approx -\frac{\hbar}{32\pi^3\epsilon_o^2}\int_0^\infty d\eta\,\frac{{\rm Tr}[\boldsymbol{\kappa}_{\rm nf}^2(i\eta)]}{\epsilon_x(i\eta)r_e^6(i\eta)}\alpha_{\rm a}(i\eta)\alpha_{\rm b}(i\eta) \tag{3.8}$$

which reduces to the well known free-space non-retarded Van der Waals interaction energy when $\epsilon_x = \epsilon_z = 1$. It is important to note that the integral is performed over the entire range of positive imaginary frequencies ($\eta = i\omega$). Generally, the hyperbolic condition $\epsilon_x\epsilon_z < 0$ is only satisfied within a finite bandwidth of the electromagnetic spectrum. We therefore expect that it would not alter the broadband cumulative effect of the entire electromagnetic spectrum, and as a result we predict that the ground-state ground-state interaction energy will not diverge in a hyperbolic medium. From Fig. 3.4, it is also clear that the ground-state ground-state Casimir Polder potential $U_{\rm gg}$ does not show any type of enhancement for the hyperbolic medium, in agreement with our discussion. Note that the distance scaling dependence in the non-retarded regions is in agreement with equations (3.7)-(3.8), as expected. In the retarded regime ($r \gg \lambda$), the excited-state interactions $U_{\rm eg}$ and $\Gamma_{\rm ET}$ display an exponential damping behaviour due to material absorption, while the ground-state interaction $U_{\rm gg}$ displays the typical Casimir-Polder power law dependence, r^{-7} (Fig. 3.4).

3.3 Practical Implementations of Hyperbolic Media

In the following, we discuss multiple experimental platforms for hyperbolic media paving the way for the experimental demonstration of the long-range Super-Coulombic interactions and unique many-body physics in hyperbolic media.

3.3.1 Plasmonic super-lattice

Fig. 3.5-a and Fig. 3.5-b propose a practical plasmonic super-lattice system to enhance atom-atom interactions taking into account the role of dissipation, dispersion and finite unit cell size. We show the large enhancement of cooperative Lamb shift (J_{dd}) for an effective medium model and compare it to a 40-layer structure consisting of Ag and TiO_2 with a total slab thickness of 100 nm. For such a system, effective medium theory predicts a type I response ($\epsilon_x > 0, \epsilon_z < 0$) for wavelengths smaller than 492 nm, and a type II response ($\epsilon_x < 0, \epsilon_z > 0$) for wavelengths larger than 492 nm. Atom A is 4 nm away from the top interface (see Fig. 3.5 inset), while atom B is assumed to be adsorbed to the bottom interface. Atom B has a fixed horizontal displacement of $x_{\mathrm{B}} = 5$ nm, and therefore there is a fixed separation angle θ_o between atom A and atom B with respect to the normal to the interface. The two large peaks seen in Fig. 3.5 occur when the dispersive resonance angle $\theta_{\mathrm{R}}(\lambda)$ is equal to the fixed separation angle, i.e. $\theta_{\mathrm{R}}(\lambda) = \theta_o$ in agreement with theory. For the material system shown here, this occurs both in the type I and type II hyperbolic regions. The inset shows the directional sensitivity of the interaction as a function of atom B's horizontal displacement. Note that accurate agreement between the effective medium model and the super-lattice structure is achieved when the unit-cell size is smaller than the separation distance between atom A and the top interface.

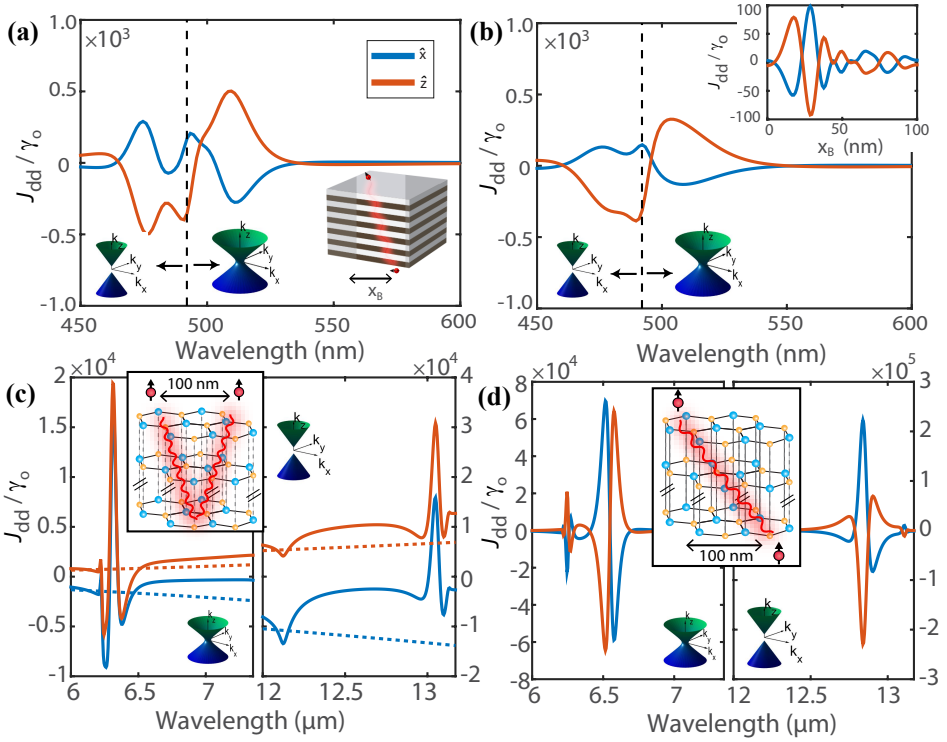

Fig. 3.5. **Giant long-range Cooperative Lamb shift in practical structures**. (a)-(b) Plasmonic super-lattice in visible range, and (c)-(d) natural hyperbolic medium in infrared range. (a) The effective hyperbolic model is compared with (b) a 40-layer multilayer system taking into account dissipation, dispersion and finite unit cell size. Atom A is 4 nm away from top interface, while atom B is adsorbed to bottom interface with a horizontal displacement of $x_{\mathrm{B}} = 5$ nm. The inset shows the cooperative Lamb shift dependence on atom B's horizontal displacement when $\lambda = 550$ nm. Good agreement is seen between the EMT model and practical multilayer design paving the way for an experimental demonstration of the Super-Coulombic effect with cold atoms. Cooperative Lamb shift for (c) two atoms above h-BN and (d) two atoms across an h-BN structure; dashed lines denote bulk vacuum results. Note that a smaller spontaneous emission rate ($\gamma_o \sim \omega^3$) in the infrared range will contribute to a larger normalized cooperative decay rate J_{dd}/γ_o. The orange and blue curves denote the two orientations of the transition dipole moment of the atoms. The total slab thickness for both structures is 100 nm.

3.3.2 Natural hyperbolic medium: hexagonal Boron Nitride

Fig. 3.5-c and Fig. 3.5-d propose a 2D Van der Waals bonded natural material, hexagonal Boron Nitride (hBN), as a candidate material to control optically-active

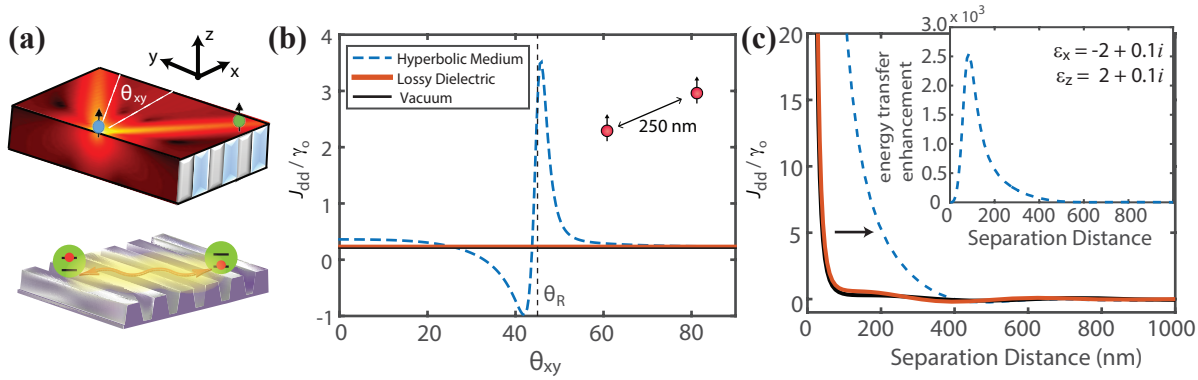

Fig. 3.6. **Super-Coulombic cooperative Lamb shift above hyperbolic meta-surface.** Cooperative Lamb shift, $J_{\rm dd}$, above hyperbolic metasurface with optic axis in the $\hat{\mathbf{x}}$ direction, calculated via dyadic Green function approach. Atom A and atom B are 2 nm above the interface. (a) Two dimensional resonance cone on hyperbolic metasurfaces which causes giant in-plane long-range dipole-dipole interactions (b) Cooperative Lamb shift dependence on angle θ_{xy} of atom B for a fixed separation distance of $r = \lambda/2 = 250$ nm. Note the clear enhancement of the resonant dipole-dipole interaction near the resonance angle $\theta_{\rm R}$. (c) Separation distance dependence of cooperative Lamb shift along the resonance angle $\theta_{xy} = \theta_{\rm R}$. Inset shows giant FRET enhancement (> 2000) for separation distances of 100 nm in the metasurface plane.

vibrational transitions between molecules, or electronic intersubband transitions between quantum wells. hBN is a natural hyperbolic medium in the mid-infrared spectral range. We show giant cooperative Lamb shifts $J_{\rm dd}$ for the case of two atoms 10 nm away from the top interface of an h-BN structure, as well as for two atoms across an h-BN film. In the first case, the atom-atom interaction is due to a Super-Coulombic ray-like interaction that reflects from the bottom interface (see insets). In the second case, the interatomic interaction is primarily due to a direct Super-Coulombic interaction from atom A to atom B. Atom A is 10 nm above the top interface, while atom B is assumed to be adsorbed to the bottom interface. Note that these long-range dipole-dipole interactions are seen equally in the type I hyperbolic region ($\lambda \sim 12 - 13$ μm) as well as the type II hyperbolic region ($\lambda \sim 6 - 7$ μm). We

have used the experimentally-verified permittivities for h-BN from Caldwell et al. for our numerical simulations [71].

3.3.3 Hyperbolic meta-surface

Finally, Fig. 3.6 proposes a 2D-material system to enhance resonant dipole-dipole interactions, using hyperbolic metasurfaces. Our theoretical proposal provides additional future directions for designer metasurfaces based on graphene, black phosphorous, h-BN, gold/air, or silver/air nanogratings [78–81] (see Fig. 3.6-a). We must emphasize that all of the experimental and theoretical studies thus far have focused on Purcell factor enhancements or the photonic spin-Hall effects. Here, we propose hyperbolic metasurfaces to control many-body dipole-dipole interactions. Fig. 3.6-a shows the key difference from bulk hyperbolic media where a two dimensional resonance cone mediates giant long-range interactions due to in-plane hyperbolic dispersion (x-y plane anisotropy). In Fig. 3.6-b, we show an enhancement of the cooperative Lamb shift $J_{\rm dd}$ versus angle θ_{xy} of atom B. The angle θ_{xy} is defined with respect to the optic axis that lies parallel to the interface, such that $\boldsymbol{\epsilon} = \text{diag}[\epsilon_x, \epsilon_z, \epsilon_z]$. A clear enhancement is seen along the resonance angle $\theta_{\rm R}$ compared to the vacuum and the dielectric half-space cases. Furthermore, when the position of atom B lies along the resonance angle $\theta_{xy} = \theta_{\rm R} = \tan^{-1}\sqrt{-\epsilon_z/\epsilon_x}$ we find a clear order-of-magnitude enhancement in the cooperative Lamb shift up to distances of 200 nm [Fig. 3.6-b and Fig. 3.6-c]. Numerical simulations of the hyperbolic meta-surface were done using a dyadic Green function approach given explicitly in the addendum of this report.

Chapter summary

To summarize, we have revealed a class of singular excited-state atom-atom interactions in hyperbolic media that arise from a fundamental modification of the Coulombic near-field. The experimental observation of such effects will require careful isolation of medium-induced cooperative interactions between atoms from the effect

of independent atoms interacting with the hyperbolic medium. Preliminary results have shown signatures of such interactions between molecules via FRET [82]. Future work should also focus on understanding the intricate role of non-locality [83, 84] on dipole-dipole interactions in hyperbolic media. Our work motivates the search for defect centers in natural hyperbolic media like hexagonal boron nitride, where the interaction is mediated by hyperbolic phonon-polaritons. It should also motivate the study of unique many-body physics in atomic lattice quantum metamaterials with hyperbolic response [85]. Finally, our work should also promote studies of long-range entanglement and self-organization [51]. This work provides a first step towards cold-atom studies with hyperbolic meta-surfaces exhibiting unique effects that are not found in photonic crystals, waveguides, or cavities.

4. MANY-BODY ENERGY TRANSFER EFFECTS IN MULTI-LAYERED NANOPHOTONIC ENVIRONMENTS

In this chapter, we extend the two-body theory of dipole-dipole interactions to take into account the effect many acceptors confined to a finite volume. This work was motivated by the experimental verification of the Super-Coulombic interaction (experimental work performed by Ward Newman) which lead to the successful demonstration of long-range dipole-dipole interactions through a hyperbolic metamaterial. This work is currently unpublished but under review. In the following, we present the many-body theory of Förster resonance energy transfer in multi-layered nanophotonic environments providing the full expressions for the energy transfer rate in terms of the dyadic Green function integrated over a finite volume. Of note, we compare the results to the well-known energy transfer spatial scaling laws in homogeneous environments. In the second part of the chapter, we present our experimental results and discuss discrepancies between theory and experiment. The focus of this Chapter is the theory but we have included experimental results for the sake of completeness.

4.1 Many-body theory of FRET in multi-layered environments

We begin by considering the two-body energy transfer rate between two molecules. Unlike the results of the previous chapter, we include the vibrational states of the molecules through the Born-Oppenheimer approximation which assumes the molecule's nuclear degrees of freedom are slowly varying compared to the electronic degrees of freedom. This difference in timescales allows the total wavefunction of the molecule to be written as the product of nuclear and electronic contributions respectively.

4.1.1 Energy transfer between two molecules

For the case of two molecules, the total transition matrix element is given by $d_{aa'(bb')} = \mathbf{d}_{A(B)} v_{aa'(bb')}$ in the Born-Oppenheimer approximation. $v_{aa'(bb')}$ corresponds to the overlap integral between the vibrational states of each molecule. Here, $\mathbf{d}_{A(B)}$ is the electronic transition dipole matrix element between the electronic ground $|a\rangle$ ($|b\rangle$) and excited state $|a'\rangle$ ($|b'\rangle$) of atom A(B). We assume molecule A is initially prepared in its excited electronic state and molecule B is initially prepared in the electronic ground state with the electrodynamic field in the vacuum state, $|i\rangle = |a'\rangle\,|b\rangle \otimes |\{0\}\rangle$. Using Fermi's Golden rule, as outlined in Chapter 2, the Förster resonance energy transfer (FRET) rate from molecule A to molecule B is given by

$$\Gamma_{ET} = \frac{2\pi}{\hbar^2} \int d\omega\, |V_{dd}(\omega)|^2 \sigma_A(\omega)\sigma_B(\omega) \tag{4.1}$$

where $V_{dd}(\omega) = \hbar\left(J_{\mathrm{dd}} - i\frac{\gamma_{\mathrm{dd}}}{2}\right) = -\frac{\omega^2}{\epsilon_o c^2}\mathbf{d}_{\mathrm{b}}\cdot\mathbf{G}(\mathbf{r}_{\mathrm{b}}, \mathbf{r}_{\mathrm{a}}; \omega_{\mathrm{a}})\cdot\mathbf{d}_{\mathrm{a}}$ is the resonant dipole-dipole interaction introduced in the previous chapter. $\sigma_A(\omega)$ and $\sigma_B(\omega)$ are proportional to the single-photon emission and absorption spectrum of molecule A and B respectively [86],

$$\sigma_A(\omega) = \sum_{a,a'} p'_a |v_{aa'}|^2 \delta(\omega_{a'a} - \omega) \tag{4.2}$$

and

$$\sigma_B(\omega) = \sum_{b,b'} p_b |v_{b'b}|^2 \delta(\omega_{b'b} - \omega) \tag{4.3}$$

where p_i is the occupation probability of state $|i\rangle$. The experimental signature of FRET is the reduction in the excited state lifetime of atom A which is sensitive to the presence of atom B in the near-field.

4.1.2 Many-body energy transfer rate: analytical derivation

We now calculate the change in the FRET rate when there is a large distribution of acceptors. The spatially integrated energy transfer rate is

$$\bar{\Gamma}_{ET} = N_a \int d\mathbf{r}_A \rho_A(\mathbf{r}_A) \Gamma_{ET}(\mathbf{r}_D, \mathbf{r}_A) \tag{4.4}$$

where $\rho_A(\mathbf{r}_A)$ represents the spatial distribution of acceptors. For the rest of the Chapter, we consider a uniform distribution of acceptors with $\rho_A = 1/V_a$, where N_a is the total number of acceptors and V_a is the confined volume surrounding the acceptor molecules. As shown in Appendix A, for multi-layered nanophotonic environments with cylindrical symmetry, the dyadic elements of the Green function may be written in the form $G_{ij} \sim \int dk_\rho \, f_{ij}(k_\rho) J_n(k_\rho \rho) \cos(n\theta)$ or $G_{ij} \sim \int dk_\rho \, f_{ij}(k_\rho) J_n(k_\rho \rho) \sin(n\theta)$, where $f_{ij}(k_\rho \rho)$ is a function containing the reflection or transmission coefficients of the environment, while $J_n(k_\rho)$ is the cylindrical Bessel function of order n. In cylindrical coordinates, the integral over the acceptor surface area yields the following types of integrals

$$\int_0^{2\pi} d\theta \int_0^{\infty} \rho \, d\rho \, |\mathbf{n}_a \cdot \mathbf{G}(\mathbf{r}_A, \mathbf{r}_D) \cdot \mathbf{n}_d|^2 \sim \begin{cases} \int_0^{2\pi} \cos(n\theta)\cos(m\theta) d\theta \int_0^{\infty} \rho J_n(k_\rho \rho) J_m(k'_\rho \rho) d\rho \\ \int_0^{2\pi} \sin(n\theta)\sin(m\theta) d\theta \int_0^{\infty} \rho J_n(k_\rho \rho) J_m(k'_\rho \rho) d\rho \\ \int_0^{2\pi} \cos(n\theta)\sin(m\theta) d\theta \int_0^{\infty} \rho J_n(k_\rho \rho) J_m(k'_\rho \rho) d\rho \end{cases}$$

The orthogonality relations of the trigonometric functions together with the closure relation of the Bessel function ensures a complete evaluation of the surface integral for any component of the Green function. In the following, we provide an exact expression

for the spatially integrated transmitted Green function. In the experiment, linearly-polarized laser light excites the donor molecules lying parallel to the interface. The Green function components related to parallel (x-oriented) donor dipole moment

$$G_{xx}(\mathbf{r}) = \frac{i}{8\pi k_1^2}\int dk_\rho \frac{k_\rho}{k_z} e^{ik_z(z_a+z_d)}\left[t_{ss}k_1^2 J_+^c + k_z^2 J_-^c t_{pp}\right] \tag{4.5}$$

$$G_{yx}(\mathbf{r}) = \frac{i}{8\pi k_1^2}\int dk_\rho \frac{k_\rho}{k_z} e^{ik_z(z_a+z_d)}\left[k_1^2 t_{ss} - k_z^2 t_{pp}\right] J_2(k_\rho\rho)\sin 2\theta \tag{4.6}$$

$$G_{zx}(\mathbf{r}) = \frac{i}{8\pi k_1^2}\int dk_\rho k_\rho^2 e^{ik_z(z_a+z_d)}\left[2it_{pp}J_1(k_\rho\rho)\cos(\theta)\right] \tag{4.7}$$

where we have used the shorthand notation for the cylindrical bessel functions $J_\pm = J_o(k_\rho\rho) \pm J_2(k_\rho\rho)\cos 2\theta$. The final result for the ensemble-averaged energy transfer rate for a two-dimensional sheet of acceptors is:

$$\int_0^{2\pi} d\theta \int_0^\infty \rho\, d\rho\, |G_{xx}|^2 = \frac{\pi}{|8\pi k_1^2|^2}\int dk_\rho \frac{k_\rho}{|k_z|^2} e^{i(k_z-k_z^*)(z_a+z_d)}\Big[3|t_{ss}k_1^2|^2 + 3|t_{pp}k_z^2|^2 + t_{pp}t_{ss}^* k_z^2 k_1^2 + t_{pp}^* t_{ss} k_z^{2*} k_1^2\Big] \tag{4.8}$$

$$\int_0^{2\pi} d\theta \int_0^\infty \rho\, d\rho\, |G_{zx}|^2 = \frac{4\pi}{(8\pi k_1^2)^2}\int dk_\rho k_\rho^3 e^{i(k_z-k_z^*)(z_a+z_d)}|t_{pp}|^2 \tag{4.9}$$

$$\int_0^{2\pi} d\theta \int_0^\infty \rho\, d\rho\, |G_{yx}|^2 = \frac{\pi}{|8\pi k_1^2|^2}\int dk_\rho \frac{k_\rho}{|k_z|^2} e^{i(k_z-k_z^*)(z_a+z_d)}|t_{ss}k_1^2 - t_{pp}k_z^2|^2 \tag{4.10}$$

To take into account the acceptor slab thickness, t_a, we evaluate the following integral

$$\int_0^{t_a} dz_a\, e^{-2\mathrm{Im}[k_z]z_a} = \frac{1-e^{-2\mathrm{Im}[k_z]t_a}}{2\mathrm{Im}[k_z]} \tag{4.11}$$

and use the substitution $e^{i(k_z-k_z^*)(z_d+z_a)} \rightarrow \frac{1-e^{-2\mathrm{Im}[k_z]t_a}}{2\mathrm{Im}[k_z]}$ in all of the previous equations. The final result is a one dimensional integral over the radial wavevector k_ρ. The integral is evaluated numerically using the Gauss-Kronrod method. The final expression (4.4) provides the total energy transfer rate from a donor to a 2-D sheet (or 3-D slab) of acceptors depending on whether we include a finite slab thickness for the acceptor molecules. These expressions form the main result of this Chapter. As we show below, the dimensionality of the acceptor volume alters the energy transfer spatial scaling law.

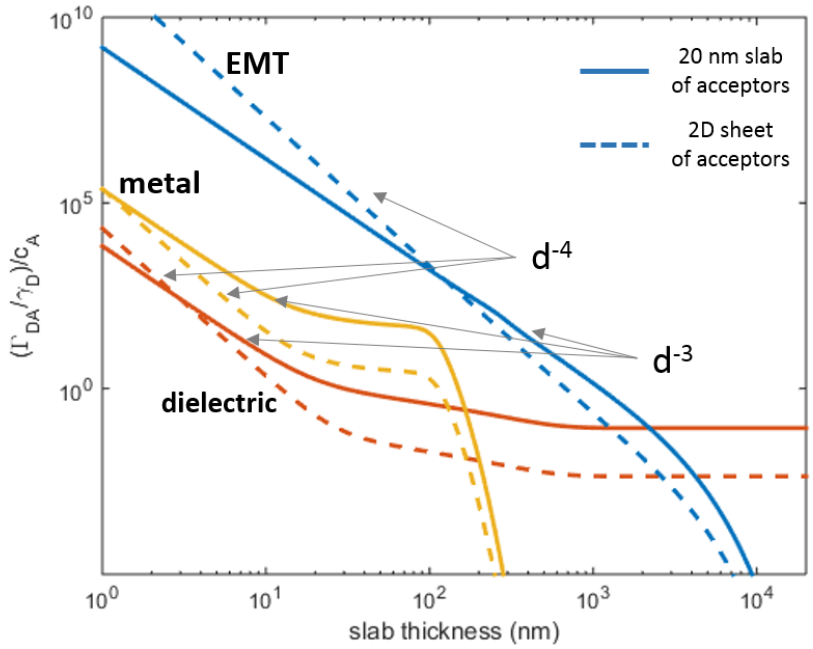

Fig. 4.1. Comparison of energy transfer power law behavior for dielectric, metal, and ideal hyperbolic medium. We provide results for infinitely thin sheet of acceptors labelled as the 2D case, as well as finite-sized 20 nm slab of acceptors. We clearly see distinct power laws for short donor-acceptor separation distances corresponding to d^{-3} and d^{-4} scaling dependence for the 3D and 2D cases respectively. We emphasize that these power laws arise from the Coulombic r^{-6} point-to-point interaction.

4.1.3 Comparison to energy transfer power laws in homogeneous media

We now compare the results derived above to the well-known energy transfer spatial scaling laws for donor-acceptor systems inside a homogeneous medium where the energy transfer rate is given by $\Gamma_{ET} = \gamma_o(R_o/r)^6$ in the near-field. The many-body energy transfer rate from a single donor molecule to a 2D sheet of acceptor molecules is given by:

$$c_a \int_0^\infty \Gamma_{ET}\, \rho d\rho = c_a \gamma_o R_o^6 \int_0^\infty \frac{\rho d\rho}{(d^2+\rho^2)^3} = c_a \gamma_o \frac{R_o^6}{4d^4} \tag{4.12}$$

where d is the distance between the donor to 2D-sheet of acceptors, while c_a is the 2D sheet concentration. This unique spatial scaling arises from the near-field Coulombic coupling, $\Gamma_{ET} = \gamma_o(R_o/r)^6$, and would not occur for radiative coupling r^{-2}. For the case of acceptors confined to a 3D slab with finite thickness t_a, we must integrate over the third spatial dimensions corresponding to the acceptor slab thickness. Upon evaluation of this additional integral, we ensemble-averaged energy transfer rate becomes proportional to d^{-3}. The result shown in Fig. 4.1 compares the 2D and 3D scaling arising from a finite-slab (20 nm) of acceptors and 2D sheet of acceptors. Note the result in Fig. 4.1 is calculated with the integral expressions in k-space, clearly reproducing the limiting power law behavior derived in this sub-section.

4.1.4 Wavevector-resolved energy transfer

Using the expressions derived above, we numerically evaluate the wavevector-resolved energy transfer rate as a function of k-space modes. This approach provides a clear separation of radiative and non-radiative contributions by separating the integral as $\int_0^\infty = \int_0^{k_1} + \int_{k_1}^\infty$. These results are analogous to the k-resolved local density of states used in nanophotonics [69], however, we must emphasize that wavevector-resolved energy transfer rate is a non-local quantity. In Fig. 4.2 we show the origin of the extended Super-Coulombic scaling law as a result of the high-k spatial frequency modes allowed to propagate within a hyperbolic medium.

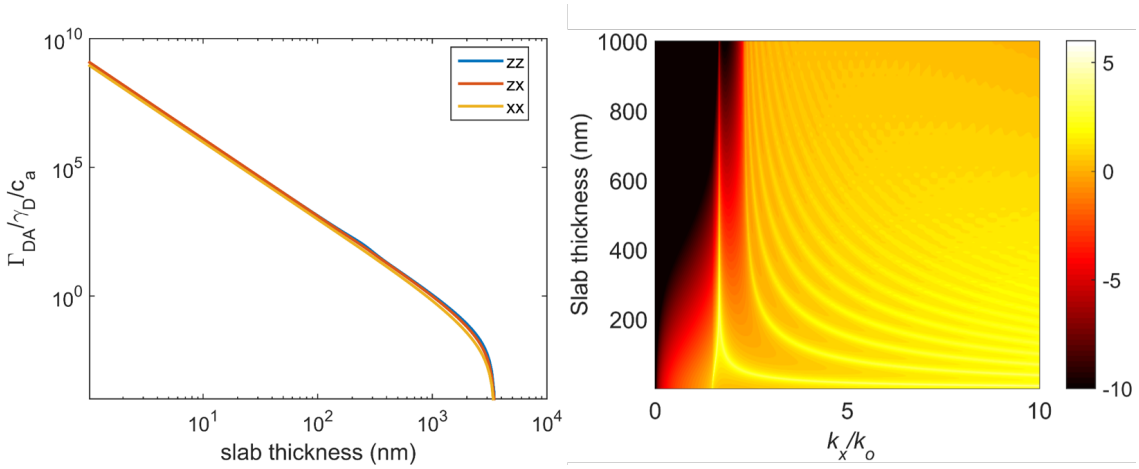

Fig. 4.2. Long distance sheet-sheet non-radiative dipole-dipole interactions in a hyperbolic medium: (left) The scaling law of energy transfer between a 2D sheet of donors and a 2D sheet of acceptors is shown versus the sheet-to-sheet separation. We observe the persistence of the near-field Coulombic scaling law ($\sim$d^{-3}) up to 5-10 μm, 500$\times$ the conventional near-field of 5-10 nm. The near-field scaling is eventually curtailed by dissipative losses at large distance. The result is shown for various donor-acceptor dipole moment orientations. (right) This extension of the Coulombic near-field originates from the high spatial frequency bulk hyperbolic polaritons that propagate in the metamaterial. These high-spatial frequency modes retain a longitudinal character even at large propagation distances, a fundamental requirement for near-field Coulombic interactions.

4.2 Experimental demonstration of long-range interaction

In Fig. 4.3-a, we present the primary experimental results showing the comprehensive set of samples required to demonstrate the long-range dipole-dipole interactions through a hyperbolic metamaterial consisting of alternating layers of metal (Ag) and dielectric (SiO_2). Nine total samples are required for isolating the role of the metamaterial on the dipole-dipole interaction as opposed to the role of the: (i) local photonic density of states (LDOS) enhancement and (ii) non-radiative enhanced quenching of donor molecules above the metal. [87, 88]. We isolate the dipole-dipole contribution by carefully comparing the results between donors with acceptors (hybrid, front row

of Fig. 4.3-a) to the donor-alone and acceptor-alone cases (middle and back rows, Fig. 4.3-a). Along with the metamaterial, experiments on Ag and SiO_2 control samples of equal thickness to the metamaterial (100 nm) were also performed.

Evidence of energy transfer from donor molecules to acceptor molecules is demonstrated through steady-state fluorescence measurements. Once again, we compare the control samples to the hybrid, donor-acceptor samples. Fig. 4.3-b, Fig. 4.3-c, and Fig. 4.3-d show the transmitted photoluminescence (PL) spectra for the control and hybrid samples of three types of material systems corresponding to dielectric, metal, and metamaterial respectively. The fabricated samples are optically pumped with a steady-state fluence of approximately 25 μW/1 mm^2 from a 405 nm continuous wave laser. Note the clear evidence of energy transfer from donor to acceptor molecules in all three material systems given by the increase in the acceptor emission intensity for the hybrid donor-acceptor case (black curve) compared to the acceptor-only case (red curve). Furthermore, there is a clear decrease in the donor emission intensity relative to the donor-only case (blue curve). We must also emphasize that while energy transfer is clearly evident for all three material systems, the transmitted PL spectra does not provide evidence of the increased dipole-dipole interaction magnitude for the hyperbolic metamaterial case. This is due to the acceptor molecules not having an equivalent photonic density of states for all three material systems. Ultimately, this will modify the observed acceptor PL spectra making it difficult to discern the strength of the dipole-dipole interaction. Evidence of an increased FRET rate is only attainable through the careful analysis of time-resolved photoluminescence.

4.2.1 Time-resolved photoluminesence

The main experimental result is shown in Fig. 4.3-e and Fig. 4.3-f demonstrating the nature of the energy transfer process through time-resolved photoluminescence of the Alq3 donor. The result clearly shows an additional increase to the donor relaxation rate in the presence of R6G acceptors across the metamaterial. Fig. 4.3

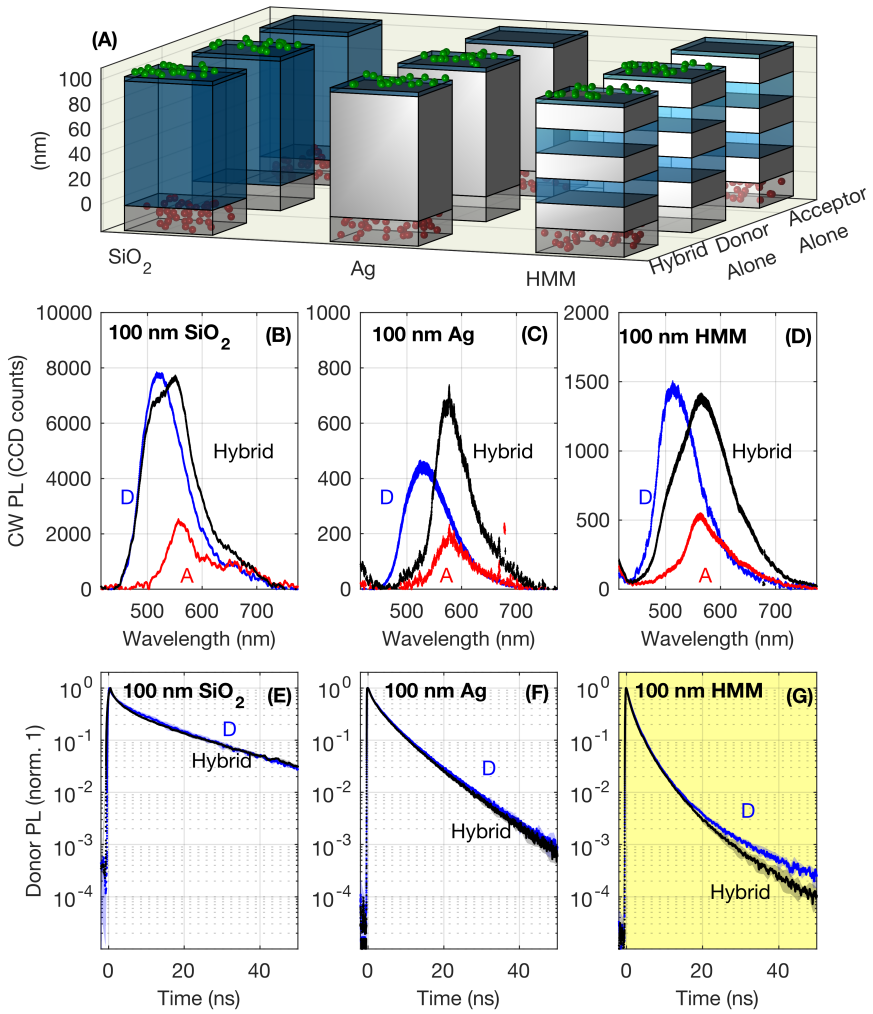

Fig. 4.3. **a** The sample-types used to isolate RDDI in various material systems is shown. Donors (Alq3, shown green) **(b, c, d)** The transmitted PL spectra for the donor and acceptor separated by dielectric, metal and metamaterial shown. We note that energy transfer is clearly visible in all three material systems; that is, the donor excited state is causing the acceptor to be excited and subsequently relax and emit a photon. This is concluded by noting an increased intensity of acceptor emission and a quenched donor emission when the emitters are placed in the hybrid geometry (black curve) relative to the donor-only (blue curve) and acceptor-only (red curve) control systems. **(e, f, g)** The time resolved donor fluorescence for donor-only (blue) and hybrid (black) samples are shown for the three material systems. For the donors:acceptors separated by 100 nm of SiO_2 or Ag **(g, h)**, the hybrid decay traces reveal no additional lifetime reduction compared to the donor-only case, indicating no long-range RDDI. When the donor and acceptors are separated by a 100 nm Ag/SiO_2 multilayer metamaterial **(g)**, we observe a marked excited state lifetime reduction when the acceptor molecules are present, providing evidence of long-range super-Coulombic RDDI.

compares the decay trace for the 100 nm SiO_2 film with (black curves) and without acceptors (blue curves). Introducing acceptors to the far-side of the SiO_2 film produces no change in the emission kinetics, despite the fact that the steady-state fluorescence indicates that there is energy transfer from donors to acceptors. This suggests that the energy transfer mechanism occurs through a much weaker dipole-dipole interaction that is radiative in nature, i.e. mediated by a photon emitted by the excited donor which propagates through the 100 nm SiO_2 film and is subsequently absorbed by the acceptor. For the 100 nm Ag material system, we only observe a Purcell-based effect which decreases the lifetime of the donor as a result of the metallic environment [89, 90], however, this system does not show any change in the donor decay trace similar to the 100 nm SiO_2 thin film.

Fig. 4.3-g shows the fundamentally different emission kinetics of the donor in the hyperbolic metamaterial system. The donor only sample shows a decreased excite-state lifetime relative to the pure Ag sample (blue Fig. 4.3-f). This is due to the enhanced optical density of photonic states in the near-field of HMMs [69, 70]. When acceptors are introduced to the opposite side of the hyperbolic metamaterial in the hybrid donor-acceptor sample (black data), we observe a notable decrease in the excited-state lifetime of the donor. This lifetime reduction offers proof of long-range super-Coulombic dipole-dipole coupling of donors and acceptors with a physical separation distance of 100 nm.

4.3 Comparison between theory and experiment

In the following, we outline the theoretical model that was developed to provide a theoretical estimate of the observed energy transfer rate extracted from the experimental data discussed above. The final result comparing theory and experiment is shown in Fig. 4.5.

4.3.1 Theory of time-resolved donor fluorescence intensity

To confirm the nature of the Super-Coulombic dipole-dipole interaction over large intermolecular distances, the experiment performed time-resolved *ensemble* measurements of the donor fluorescence intensity. In the following, we provide a simple derivation showing how the integrated (many-body) energy transfer rate emerges naturally from the time-resolved donor fluorescence intensity. In general, the fluorescence intensity decay trace of a donor surrounded by N_a acceptor molecules depends on the probability of the energy transfer from the donor to each of the acceptors. For a given configuration specified by the donor position $\mathbf{r}_D$, and acceptor positions $\mathbf{r}_{Aj}$, the total donor decay rate γ_D is given by $\gamma_D = \gamma_o + \sum_i^{N_a} \Gamma_{ET}(\mathbf{r}_{Ai}, \mathbf{r}_D)$, where γ_o is the spontaneous emission rate of the donor in the absence of acceptor molecules. The total donor intensity decay trace is given by [91]

$$\begin{aligned} I_D(t) &\sim e^{-\gamma_o t} \int d\mathbf{r}_{A1}\, \rho(\mathbf{r}_{A1}) \int d\mathbf{r}_{A2}\, \rho(\mathbf{r}_{A2}) \cdots \int d\mathbf{r}_{AN_a}\, \rho(\mathbf{r}_{AN_a}) e^{-t\sum_i \Gamma_{ETi}(\mathbf{r}_{Ai}, \mathbf{r}_D)} \\ &\sim e^{-\gamma_o t} \left[\int d\mathbf{r}_A\, \rho(\mathbf{r}_A) e^{-t\Gamma_{ET}(\mathbf{r}_A, \mathbf{r}_D)} \right]^{N_a} \end{aligned} \tag{4.13}$$

where we must spatially average over all possible acceptor locations for every acceptor molecule. In the limit of small point-to-point energy transfer rates $t\Gamma_{ET} \ll 1$, an assumption that is generally valid for large separation distances between donors and acceptors, the exponential term may be expanded giving the final result,

$$\begin{aligned} I_D(t) &\approx e^{-\gamma_o t} \left[\int d\mathbf{r}_A\, \rho(\mathbf{r}_A)(1 - t\Gamma_{ET}(\mathbf{r}_A, \mathbf{r}_D)) \right]^{N_a} \\ &\sim e^{-\gamma_o t} \exp\left[-c_A \int d\mathbf{r}_A \Gamma_{ET}(\mathbf{r}_D, \mathbf{r}_A) t \right] \end{aligned} \tag{4.14}$$

We used the basic definition of the exponential, $\exp(x) = \lim_{n\to\infty}(1 + x/n)^n$, and assumed a uniform acceptor density $\rho(\mathbf{r}_a) = 1/V_a$ in the thermodynamic limit ($N_a \to \infty, V_a \to \infty, N_a/V_a \to$ const). We emphasize this result predicts the measured donor's photoluminescence decay trace will consist of the donor's spontaneous emission γ_o contribution, in addition to the *spatially-integrated* energy transfer rate from the donor to the uniform distribution of acceptors. The integral is performed over the

total volume of the acceptors and is in agreement with the general result derived earlier in this Chapter.

4.3.2 Calibration of theoretical model

In Fig. 4.4, we provide a flow chart outlining the first-principles theoretical model used to estimate the many-body energy transfer. The results from this model are compared with the extracted energy transfer rates from the experiment. Note that the theoretical model avoids the use of fitting parameters, only using measured experimental parameters as *calibrated inputs*. For example, the theoretical model uses the dielectric permittivity values obtained through ellipsometry measurements, as well as film thicknesses independently verified through SEM imaging, a quartz crystal monitor, and ellipsometry measurements. Similarly, the estimated two-point FRET rate was calibrated through independent measurements of the FRET radius R_o, the spatially-averaged spontaneous emission lifetime of the donor molecules γ_o, and the acceptor concentration c_a estimated independently through transmission measurements utilizing the Beer-Lambert law. Additional details related to the FRET radius calibration is included at the end of this Chapter.

4.4 Spatial scaling of energy transfer rate

To elucidate the distance scaling law of dipole-dipole interactions mediated by metamaterials, we fabricated additional structures displaying varying strengths of RDDI owing to the different separation distance (20, 60 nm) between donors and acceptors. We experimentally quantify the effective FRET strength between the donors and acceptors using the harmonic mean of the measured decay rates of the donor emission kinetics with and without acceptors (see [92]). If the observed decay traces $I(t)$ are normalized to unity at time zero, the integral of the trace over time yields an averaged excited-state lifetime, $\bar{\gamma}^{-1} = \bar{\tau} = \int \mathrm{d}t I(t)$. Since we are in the weak coupling limit, the difference between the average decay rate of the donors

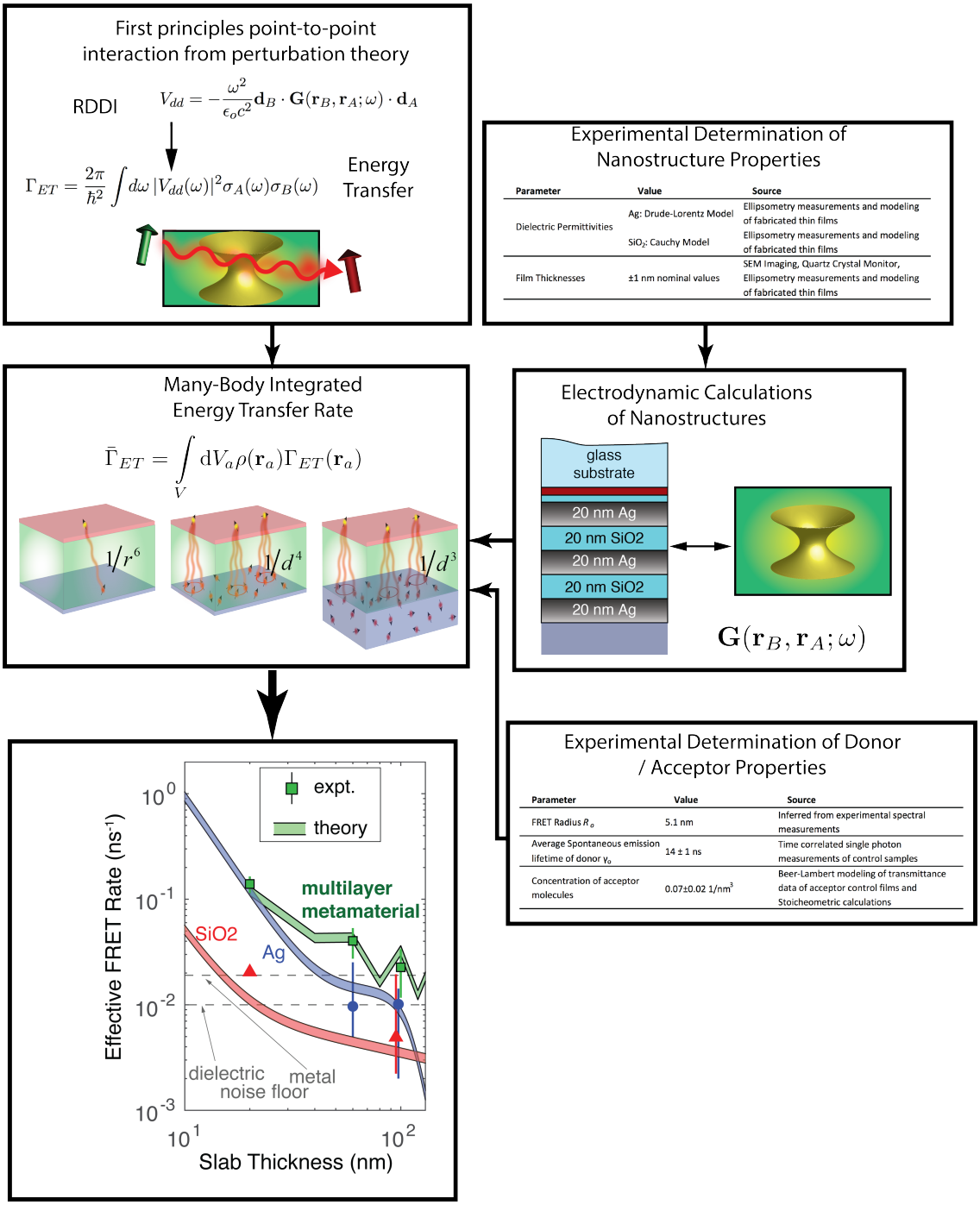

Fig. 4.4. Flow chart for going from point-to-point super-Coulombic dipole-dipole interactions, to many body ensemble dipole-dipole interactions observed in experiment.

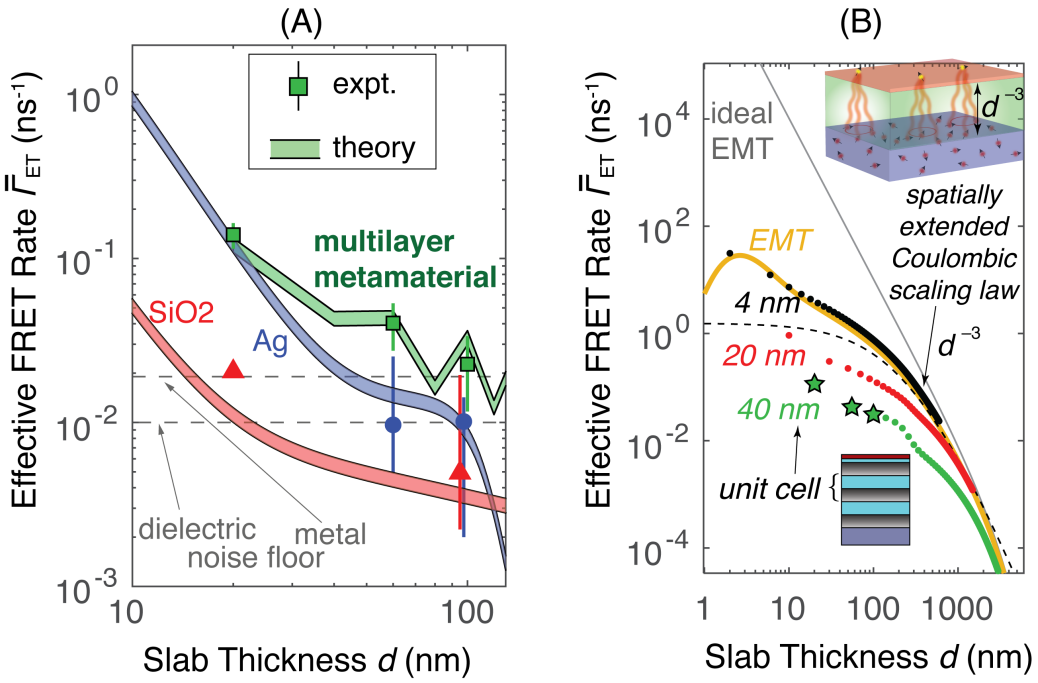

Fig. 4.5. Spatial scaling of Super-Coulombic interactions. **(a)** Experimental confirmation of enhanced energy transfer rates due to the Super-Coulombic effect in a hyperbolic metamaterial (green) compared to silver film (blue) and SiO2 film (red). The noise floors are denoted by dashed curves and the numerically calculated many-body dipole-dipole interaction curves are denoted by the colored bands. The theoretical predictions include 10% error bands accounting for uncertainty in the independently extracted physical parameters. **(b)** Numerically simulated spatial dependence of sheet-to-slab (2D sheet of donors and thin slab of acceptors) many-body dipole-dipole interactions demonstrating an enhanced FRET rate of the effective medium model (yellow) with d^{-3} power law dependence. Super-lattice structures with unit-cell sizes of 40 nm, 20 nm, and 4 nm respectively are also shown exhibiting an extended spatial range with enhanced Coulombic interactions beyond the scale of a wavelength. The green stars correspond to the experimentally measured data. The solid grey line shows the ideal EMT limit of adsorbed quantum emitters on a hyperbolic medium whereas the dashed black line presents the analytical scaling law taking into account the finite distance between the emitter and metamaterial.

with and without acceptors yields the effective FRET rate of donors to acceptors: $\bar{\Gamma}_{ET} = \bar{\gamma}_{DA} - \bar{\gamma}_{D}$. Here, $\bar{\gamma}_{D}$ denotes the averaged excited-state lifetime for a system of donor molecules without acceptors, while $\bar{\gamma}_{DA}$ denotes the excited-state lifetime for a system of donor molecules in the presence of acceptors.

The observed effective FRET rates and their scaling for three separation distances between donor and acceptor molecules are shown in Fig. 4.5. Using the theoretical framework developed in this Chapter, we provide a detailed quantitative comparison of the metamaterial response in the ideal effective medium theory (EMT) limit as well as the practical finite-sized multilayer structure. Using only physical quantities extracted independently from experiment (permittivity, layer thicknesses, FRET radius, donor decay rate, quantum yield and acceptor concentration) with no additional fitting parameters, the predicted many-body Super-Coulombic interaction theory shows excellent agreement with the experimentally observed FRET rates across the metamaterial (Fig. 4.5-a). The enhancement of FRET due to the HMM is close to two orders of magnitude compared to the dielectric and one order of magnitude larger than the metal case. Our simulations take into account the discrete nature of the metamaterial. The sawtooth behavior of the FRET rate is related to the influence of the termination layer (metal or dielectric) in the metamaterial sample.

4.4.1 Modified Super-Coulombic scaling law

Motivated by the agreement between theory and experiment (green stars and green dots in Fig. 4.5-b, we also compare the spatial scaling of the integrated FRET rate for the experimental realization of the metamaterial to the ideal effective medium theory limit of super-Coulombic RDDI for adsorbed quantum emitters on a hyperbolic medium (light gray line). We plots results for various unit-cell sizes. As the unit-cell size is decreased to 4 nm, a very strong agreement is noticed between effective medium theory (yellow curve) and the multi-layered system (black dots). We emphasize that the dramatic spatial extension of the Coulombic spatial scaling ($\Gamma_{ET} \sim d^{-3}$)

to beyond the wavelength scale ($d > 500$ nm) despite the inclusion of realistic losses, dispersion, absorption and finite unit-cell size of the metamaterial is evidence of the super-Coulombic effect. The dashed black curve presents our analytical model (given by the following equation) of the super-Coulombic FRET taking into account the finite distance between the emitter and metamaterial (z_a). The modified Coulombic scaling law taking into account this proximity effect is

$$\Gamma_{ET} \sim (d\,\mathrm{Re}[\sqrt{\epsilon_x/\epsilon_z}] + z_a)^{-3}. \tag{4.15}$$

Strong agreement in the scaling law between EMT and multi-layered simulations occurs when the unit-cell size is significantly smaller than the molecule-interface separation distance ($a_o < z_a$). The spatial range of the Super-Coulombic interaction is ultimately curtailed by material absorption (ϵ'') with an interaction range of $\xi^{-1} = \frac{\omega}{c}\sqrt{\frac{\epsilon_z''|\epsilon_x'|+\epsilon_z''|\epsilon_x'|}{|\epsilon_x'|+|\epsilon_z'|}}$.

This metamaterial-mediated non-radiative Förster interaction with Coulombic scaling should be contrasted with the previously reported super-radiant lifetime change in quantum dots which only showed a radiative interaction and $V_{dd} \sim 1/R$ scaling at the comparable distance of 150 nm [93]. Furthermore, two mesoscopic atomic clouds have shown Förster interaction at 40 microns [94]. However, the transition wavelength is 1 cm placing the experiment in the extreme near-field regime ($d \approx \lambda/250$). For comparison, if similar mesoscopic atomic systems were interacting through a hyperbolic metamaterial functioning at $\omega = 30$ GHz $\equiv 1$ cm, the interaction distance would be a centimeter.

4.4.2 Chapter Summary and Outlook

In this chapter, we developed a rigorous first-principles theoretical framework for many-body energy transfer in multi-layered nanophotonic environments. We used the result to estimate the long-range energy transfer rate and compared it to an experiment performed by Ward Newman. We obtained excellent agreement thereby providing the first demonstration of long-range Super-Coulombic dipole-dipole in-

teractions mediated by metamaterials in the optical frequency regime. We envision that Super-Coulombic interactions will impact deterministic entanglement creation between remote emitters [95], will increase the range of bio-molecular FRET rulers and FRET imaging systems [96], and will accelerate the progress towards the long-standing goal of strongly coupled quantum systems at room temperature.

Chapter Appendix: FRET radius for calibration

In order to calibrate the first-principles theory to the experiment, we use the famous Förster formula [97]

$$\frac{\Gamma_{ET}}{\gamma_o} = 18\pi \int_0^\infty f_d(\omega)\sigma_a(\omega)|\mathbf{n}_a \cdot \mathbf{G}(\mathbf{r}_A, \mathbf{r}_D; \omega) \cdot \mathbf{n}_d|^2 d\omega \tag{4.16}$$

expressed in terms of the normalized emission spectrum $f_d(\omega)$ of the donor, as well as the absorption cross-section $\sigma_a(\omega)$ of the acceptor which is phenomenologically determined through photoluminescence measurements. Here, γ_o is the donor decay rate measured in a homogeneous environment with $\mathbf{n}_a$ and $\mathbf{n}_d$ representing the unit orientation vectors for each dipole. This formula is directly related to measured quantities found in experiments, providing a direct approach to calibrate the theoretical predictions.

In free-space, the dyadic Green function is frequency-independent in the near-field limit ($kr \ll 1$). One may therefore remove the Green function contribution from the spectral integral resulting in the conventional definition for the FRET radius,

$$R_o^6 = Q_D \frac{9c^4\kappa^2}{8\pi} \int_0^\infty \frac{f_d(\omega)\sigma_a(\omega)}{n^4\omega^4} d\omega. \tag{4.17}$$

The FRET radius is defined as the donor-acceptor separation distance resulting in the FRET rate being equal to the donor spontaneous emission rate. For general nanophotonic environments, this definition of the FRET radius is not possible due to the frequency- dependence of the dyadic Green function. However, as shown in Fig. 4.6, the transmission for extraordinary-polarized light is slowly varying as a function of wavelength. In the spectral overlap region, the transmittance changes very slowly as a function of wavelength indicating that the permittivity values also change slowly. This suggests we can remove the Green function dependence from the spectral integral and approximate the FRET rate as

$$\frac{\Gamma_{ET}}{\gamma_o} = 16\pi^2 k^4 R_o^6 \, |\mathbf{n}_a \cdot \mathbf{G}(\mathbf{r}_A, \mathbf{r}_D; \omega_{da}) \cdot \mathbf{n}_d|^2 \tag{4.18}$$

where the FRET radius is equal to the conventional definition written above. The numerical Green function is evaluated at the peak of the emission-absorption spectrum overlap.

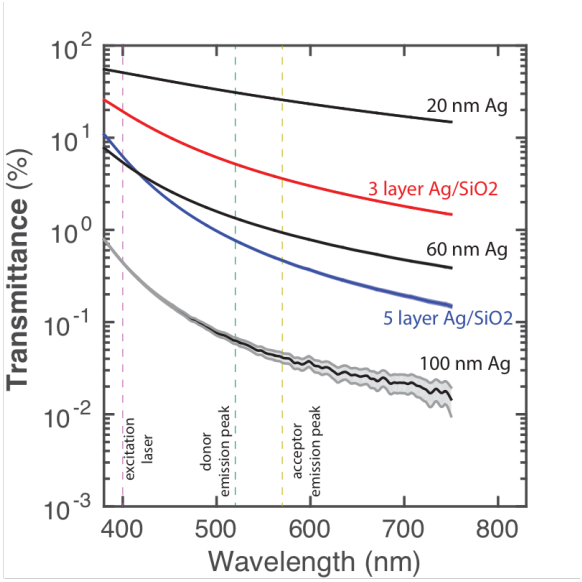

Fig. 4.6. The transmittance for extraordinary polarized light is shown for various metal and metamaterial samples. The donor and acceptor emission peaks are denoted by the green and yellow vertical dashed lines respectively.

5. FIGURES OF MERIT FOR ENGINEERING FÖRSTER RESONANCE ENERGY TRANSFER

This chapter presents the starting point for the second part of this thesis. Here, we present results related to an ongoing debate regarding the control of Förster resonance energy transfer in nanophotonic environments. We demonstrate that a simple image dipole model can be used to explain various regions of enhancement, suppression, and null-control of resonance energy transfer above a half-space dielectric as well as for two atoms near a dielectric or metal nanoparticle. The results are valid in the weak and incoherent coupling limits of resonance energy transfer. The coherent coupling limit of resonance energy transfer requires a fundamentally different analysis as given by the proceeding Chapter.

5.1 Motivation: an ongoing debate

Over the past 15 years there has been an ongoing debate regarding the influence of the environment on Förster resonance energy transfer (FRET). Disparate results corresponding to enhancement, suppression and null effect of the photonic environment have led to a lack of consensus between the traditional theory of FRET and experiments. Here we show that the quantum electrodynamic theory (QED) of FRET is exactly equivalent to an effective near-field model describing electrostatic dipole-dipole interactions. This connection leads to an intuitive and rigorously exact description of FRET, previously unavailable, bridging the gap between experimental observations and theoretical interpretations. Furthermore, we show that the widely used concept of Purcell factor variation is only important for understanding spontaneous emission and is an incorrect figure of merit (FOM) for analyzing FRET, as has been done in several experiments. To this end, we introduce two new figures of merit

which characterize resonance energy transfer: (1) the FRET rate enhancement factor (F_{ET}), (2) FRET efficiency enhancement factor (F_{eff}) and 3) two-point resonant dipole-dipole interaction (V_{EE}) which contains the photonic properties of the environment governing FRET and is analogous to the local density of states that controls spontaneous emission. Counter to previous claims, we show that suppression of the donor Purcell factor is necessary for enhancing the efficiency of the FRET process. We place bounds on the FRET figures of merit arising from both material absorption within environment as well as from intrinsic properties of the emitters including quantum efficiencies and dipole-moment orientation dependence. Finally, we use our approach to conclusively explain several experiments while predicting regimes where the FRET rate is expected to be enhanced, suppressed or remain the same. Our work paves the way for a complete theory of FRET with predictive power for designing the ideal photonic environment to control FRET in incoherent coupling limit.

While the microscopic nature of FRET is widely understood and accepted in simple homogeneous systems, the fundamental nature of FRET in complex photonic environments remains poorly understood and has been widely debated over the past 15 years (see table I). The debate is largely based on the vastly different and seemingly contradictory results of many experiments (see table I) when donor-acceptor pairs are placed in the vicinity of photonic cavities or nanoparticles. In some cases FRET has been shown to be enhanced [98–110], suppressed [108–113], or remain unchanged [114–117]. While the theory of FRET has been developed extensively since the first initiation by Förster, ranging from semi-classical electrodynamic theories to microscopic and macroscopic quantum electrodynamic (QED) theories [118–134], there remains a significant disparity between experimental results and theoretical predictions. This has also led to conjectures that the FRET rate is independent of the photonic environment. Thus, no insightful approach exists that can explain the underlying physics behind the disparity of observations in experiments.

The purpose of the present work is to illuminate the fundamental nature of FRET in a nanophotonic environment for experimentally-relevant scenarios, thereby resolv-

Table 5.1.
Experimental Results of FRET

	Enhancement	Suppression	No effect
Microcavity	[98–100, 106]	[113]	[114, 115, 117]
Nanoparticles	[101–105, 107–110]	[108–112]	[116]

ing the debate that has been ongoing for fifteen years. We show that the QED perturbative approach to analyzing dipole-dipole interactions in a nanophotonic environment can be completely captured by an effective near-field dipole model. This lends itself to a physically intuitive picture of environmental FRET rate modification that was not available before. As a result of our model, we are able to conclusively explain key recent experiments which have shown surprisingly contradictory results of enhancement, suppression and even no effect of the environment on FRET. We also show that the lack of FRET rate variation in recent experiments is not a universal behavior but is strongly dependent on environmental conditions and orientation effects. We define a FRET rate enhancement factor analogous to the Purcell factor used in spontaneous emission modification calculations to quantify the influence of nanostructures on the FRET rate. These introduced figures of merit (FOM) capture the contradictory regimes of FRET completely in the widely used planar and spherical nanostructured geometries. Our work also clarifies an important puzzling observation that the FRET rate enhancement factor (F_{ET}) as generally smaller than the Purcell factor (F_p) in most experiments; however, we show how careful design of environmental properties can result in cases where F_{ET} can be greater than F_p. A striking manifestation of this property can be exploited to enhance FRET efficiency in an all-dielectric (transparent and lossless) system where we predict that the FRET efficiency can be enhanced by more than 300-400%. Finally, we place bounds on the achievable figures of merit in realistic photonic environments that arise from orientation effects and limitations of intrinsic quantum efficiency of donors.

5.2 Theory of spontaneous emission

It is well understood that spontaneous emission and FRET have underlying connections but we show that the environmental attributes which govern them are entirely different. Using Fermi's Golden rule and the first order transition amplitude, one arrives at the general expression of the spontaneous emission (SE) rate

$$\gamma_{D,rad} = \frac{2\omega_D^2 |d_D|^2}{\hbar \epsilon_0 c^2} [\mathbf{n}_D \cdot \mathrm{Im}\{\mathbf{G}(\mathbf{r}_D, \mathbf{r}_D; \omega_D)\} \cdot \mathbf{n}_D] \tag{5.1}$$

for an atom in an inhomogeneous environment. ω_D is the radial frequency, $\hbar$ is the reduced Planck's constant, c is the speed of light, ϵ_o is the free-space permittivity, and $\mathbf{G}(\mathbf{r}, \mathbf{r}; \omega)$ is the classical dyadic Green function (GF) related to the electric field of the dipole with dipole moment $\mathbf{d}_D = d_D \mathbf{n}_D$. It is well established that the SE rate is dependent on the density of photonic modes of the environment quantified by the partial local density of states (LDOS) [135]

$$\rho_E(\mathbf{r}_D; \omega) = \frac{6\omega}{\pi c^2} \mathbf{n}_D \cdot \mathrm{Im}\{\mathbf{G}(\mathbf{r}_D, \mathbf{r}_D; \omega)\} \cdot \mathbf{n}_D \tag{5.2}$$

for a given dipole orientation $\mathbf{n}_D$. Note that the LDOS depends on the position $\mathbf{r}_D$ of the donor dipole moment only. An enhancement in the LDOS $\rho_E(\mathbf{r}_D; \omega)$ compared to that in vacuum $\rho_E^o(\mathbf{r}_D; \omega)$ translates into a larger decay rate described by the Purcell factor

$$F_p = \frac{\gamma_{D,rad}}{\gamma_{D,rad}^o} = \frac{\rho_E(\mathbf{r}_D; \omega)}{\rho_E^o(\mathbf{r}_D; \omega)}. \tag{5.3}$$

This is the well known figure of merit that is used to describe the decay rate enhancement or suppression of spontaneous emission in the case of low absorption. In the general case where the donor atom has an intrinsic quantum yield given by $Q_D = \frac{\gamma_{rad}}{\gamma_{rad} + \gamma_{nrad}}$, where γ_{nrad} is a nonradiative decay rate that is assumed to be independent of the environment, the overall enhancement of spontaneous emission becomes [136, 137]

$$\frac{\gamma_D}{\gamma_D^o} = (1 - Q_D) + Q_D F_p. \tag{5.4}$$

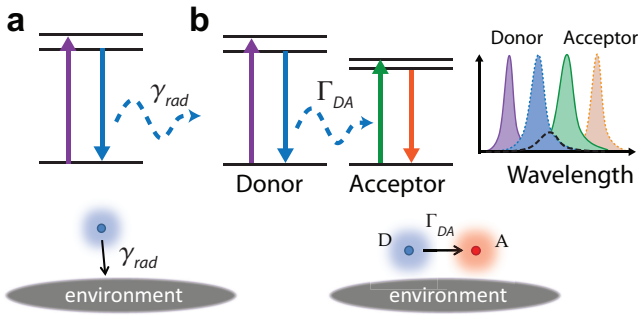

Fig. 5.1. (a) Energy-level diagram depicting spontaneous emission. γ_{rad} denotes the rate of radiative energy transfer to any location in the environment. The acceptor is not considered as part of the environment. (b) Energy-level diagram depicting FRET. FRET occurs when two neighboring atoms or molecules, denoted as donor and acceptor, have overlapping emission and absorption spectra and couple due to a Coulombic dipole-dipole interaction. The FRET rate Γ_{DA} denotes the energy transfer to the acceptor location only.

5.3 Environment-modified FRET

While the preceding results have been well established in literature, questions have emerged whether the same physical quantities can characterize the effect of the environment on Förster resonance energy transfer. FRET can be understood as spontaneous emission of a donor molecule to the specific location of the acceptor triggered by near-field dipole-dipole interaction. Within the semi-classical picture, a donor dipole induces a dipole moment of a nearby polarizable acceptor. If the donor and acceptor have overlapping emission and absorption spectra (see Fig. 5.1-b), then resonance energy transfer occurs. In the QED picture, FRET rate variation is mediated by virtual photons [127]. One arrives at the expression for the FRET rate,

$$\Gamma_{DA} = \frac{2\pi}{\hbar^2} \int d\omega \, |V_{EE}(\omega)|^2 \sigma_D(\omega) \sigma_A(\omega) \tag{5.5}$$

using Fermi's Golden rule by including the second order transition amplitude [129, 138]. Here, $\sigma_D(\omega)$ and $\sigma_A(\omega)$ represent the single-photon emission and absorption spectra of the donor and acceptor respectively. The results given above are applica-

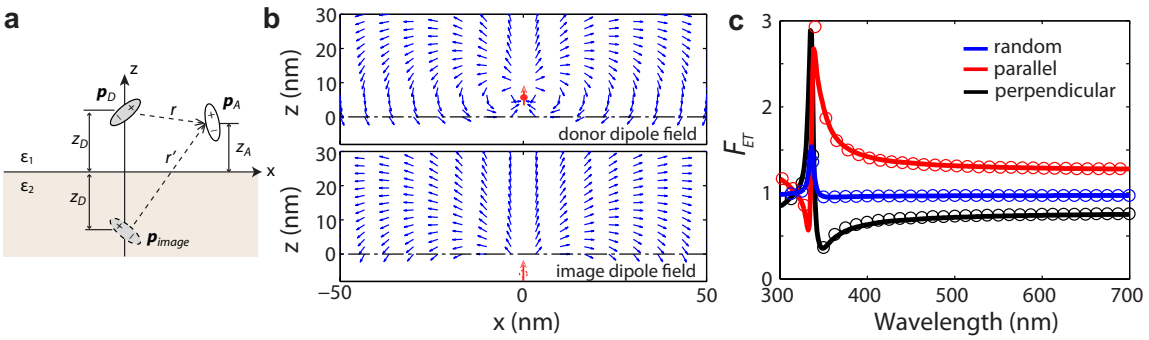

Fig. 5.2. **Environment modified dipole-dipole interactions and FRET.** QED theory of dipole-dipole interactions in the near-field is completely captured by an effective dipole model. FRET is governed by induced image dipoles in the metallic environment explaining a multitude of puzzling experimental observations. (a) Image dipole method for half-space structure. The magnitude of the image dipole moment is given by $p_{image} = \frac{\epsilon_2 - \epsilon_1}{\epsilon_2 + \epsilon_1} p_D$. (b) Visualization of normalized electric field plots for vertical donor dipole (above) and vertical image dipole (below) with $|\epsilon_2| > |\epsilon_1|$. Note that a non-trivial superposition of fields due to the vectorial nature of the electric field results in regimes of suppression, enhancement, and null effect on FRET. These regimes cannot be explained by the LDOS or Purcell factor alone. (c) FRET rate figure of merit for two dipoles 7 nm apart, and 7 nm above silver. Enhancement is seen when $|\epsilon_2| < |\epsilon_1|$, suppression is seen when $|\epsilon_2| > |\epsilon_1|$, while no effect is seen when $|\epsilon_2| \approx |\epsilon_1|$. These regimes are determined by the orientation of the image dipole. Note also that the FRET rate enhancement has a non-trivial dependence on the wavelength (see also table I). Exact QED results are denoted by the solid lines which are in complete agreement with our analytical expressions (circles).

ble for quantum emitters placed in a linear, absorbing and dispersive electromagnetic environment. We emphasize that elaborate calculations with macroscopic QED theory yield the exact same results as a semi-classical theory with only minor differences in the definition of the dipole moment. The dependence of FRET rate Γ_{DA} on the environment is clear through resonant dipole-dipole interaction (RDDI),

$$V_{EE}(\mathbf{r}_A, \mathbf{r}_D; \omega) = -\frac{\omega^2}{\epsilon_o c^2} \mathbf{d}_A \cdot \mathbf{G}(\mathbf{r}_A, \mathbf{r}_D; \omega) \cdot \mathbf{d}_D \tag{5.6}$$

as the environmental quantity that acts in an analogous way to the LDOS but instead mediates the magnitude of the FRET dipole-dipole interaction through virtual photon exchange. The subscript $_{EE}$ refers to an electric dipole interaction which is governed by the electric field of each dipole. The definition can be generalized to the case of magnetic dipole interactions (V_{BB}) and electric-magnetic dipole interactions (V_{EB}) as well. Note that in the near-field limit ($kr << 1$), the FRET rate reduces to the well known Förster formula ($\Gamma_{DA} \propto 1/n^4 r^6$) with the expected r^{-6} and n^{-4} dependence.

Note that the LDOS and FRET rate are both dependent on the dyadic Green function which contains all of the environmental information. The FRET rate is clearly not dependent on the LDOS, as debated in several papers [114–116]. Nevertheless, it is dependent on the environment through the two-point Green function. While the LDOS is a measure of the energy transfer rate to any location in the environment, the RDDI is a measure of the energy transfer rate to the acceptor location only (see Fig. 5.1). Analogous to the Purcell factor, we now introduce the FRET rate figure of merit

$$F_{ET} = \frac{\Gamma_{DA}}{\Gamma^o_{DA}} \tag{5.7}$$

where the denominator is the homogeneous FRET rate. Combining these results, the total decay rate of a (high-yield) donor in an inhomogeneous environment is

$$\gamma_{DA} = F_p \gamma^o_D + F_{ET} \Gamma^o_{DA} \tag{5.8}$$

where the first term denotes the modified spontaneous emission rate and the second term denotes the modified FRET rate.

5.4 Near-field image dipole model

We now show that the QED picture, consisting of virtual photon exchange, is completely captured by an effective dipole model that may be derived independently using the method of images. In a homogeneous environment, the FRET rate becomes comparable in magnitude to the SE rate for donor-acceptor separation distances of

$r \ll c/\omega_D$. This implies that the dipole-dipole interaction is dominated by a quasistatic field. Therefore to control FRET we must engineer the *quasistatic* fields as opposed to the electrodynamic fields. In both semi-classical and quantum theories of energy transfer, the FRET rate (5.5) is governed by the projected electric field induced by the donor, $\mathbf{E}(\mathbf{r}_A;\omega) = \omega^2\mu_o\mathbf{G}(\mathbf{r}_A,\mathbf{r}_D;\omega)\cdot\mathbf{d}_D$, at the location of the acceptor. In the near-field of a planar interface (see Fig. 5.2-a), it can be written as

$$\mathbf{n}_A \cdot \mathbf{E}(\mathbf{r}_A;\omega_D) = \frac{d_D}{4\pi n_1^2}\frac{\kappa}{r^3} + \frac{d_{image}}{4\pi n_1^2}\frac{\kappa'}{r'^3} \tag{5.9}$$

which simply denotes the dipole-dipole interaction between the donor and acceptor (first term) and the image dipole and acceptor (second term). Here, r and r' represent the donor-acceptor and image-acceptor separation distances respectively, $\kappa = (3\cos\theta_{Ar}\cos\theta_{Dr} - \cos\theta_{A,D})$ is the commonly used orientation parameter between the donor and acceptor [127], and $\kappa' = (3\cos\theta_{Ar'}\cos\theta_{D'r'} - \cos\theta_{A,image})$ is the orientation parameter between the acceptor and the image dipole.

Eqs. (5.5) and (5.9) imply that the total FRET rate is dependent on the total field generated at the acceptor location by the donor as well as its image dipole. This leads to a subtle interplay of interference effects that completely govern the nature of FRET. Note that while the donor dipole moment d_D is independent of the environment, the induced image dipole has an environment-dependent dipole moment given by

$$d_{image} = \frac{\epsilon_2 - \epsilon_1}{\epsilon_2 + \epsilon_1} d_D. \tag{5.10}$$

The FRET rate figure of merit is finally given by

$$F_{ET} = \left| \frac{\kappa}{r^3} + \frac{\epsilon_2 - \epsilon_1}{\epsilon_2 + \epsilon_1}\frac{\kappa'}{r'^3} \right|^2. \tag{5.11}$$

At this point we must make several observations in comparison to experimental results. First, note that the magnitude of the image dipole moment is enhanced at the surface plasmon (SP) resonance condition ($\epsilon_1 + \epsilon_2 = 0$). As expected, this explains why many experiments have observed FRET rate enhancements near the SP resonance (see table I). More importantly, FRET can be enhanced or suppressed depending on interference effects arising from the field of the image dipole. This is

clearly evident from our theoretical model since the orientation of the image dipole determines constructive or destructive interference effects depending on the magnitude of ϵ_1 and ϵ_2. The image dipole maintains its original orientation [see Fig. 5.2-a] if $|\epsilon_2| > |\epsilon_1|$ leading to enhancement, on the other hand, the image dipole orientation flips if $|\epsilon_2| < |\epsilon_1|$ causing FRET rate suppression (see eqn (5.9) and (5.11)). Thus in the case of metals which are highly dispersive, both regimes can be observed in different wavelength ranges.

Third, note that the vectorial structure of the near-field of the donor and image dipole results in a spatial inhomogeneity of the quasi-static fields. This affects the FRET rate depending on the acceptor location (see Fig. 5.2-b). This explains why various donor-acceptor geometric configurations with similar materials can result in suppression or enhancement of FRET. We emphasize that two important aspects which govern the regimes of enhancement, suppression or no effect throughout the various experimental studies of FRET are (a) the spectral overlap region in which FRET takes place and (b) the donor-acceptor separation compared to the distance from the photonic environment. The FRET rate will be independent of the environment only if the distance of the donor-acceptor pair from the photonic environment is much larger than the donor-acceptor separation distance. Environmental effects are also reduced when the mode resonances of the photonic environment do not lie in the spectral overlap region of the donor-acceptor pair [see Table 5.1].

(1) ***Perfect Reflector*** For the case of a perfect reflection eqn (5.10) shows that the image dipole moment magnitude is equal to the donor dipole moment magnitude. The perfect reflector condition is satisfied when there is high absorption in medium 2 ($\epsilon_2'' \to \infty$), or when there is a high contrast between the permittivities of medium 1 and 2 ($|\epsilon_2'|/\epsilon_1 \gg 1$) which typically occurs far from the SP resonance in the long-wavelength limit.

A simple analysis of the FRET rate dependence yields the following table of regimes:

Table 5.2.
Perfect reflector regimes for F_{ET}

F_{ET}	collinear dipoles ($\kappa^2 = 4$)	parallel dipoles ($\kappa^2 = 1$)	randomly oriented ($\langle\kappa^2\rangle = 2/3$)
$z_D/\rho \ll 1$	*suppression*	*enhancement*	*suppression*
$z_D \sim \rho$	*enhancement*	*suppression*	*no effect*
$z_D/\rho \gg 1$	*no effect*	*no effect*	*no effect*

In the table, we let $z_A = z_D$ while ρ denotes the horizontal separation distance between the donor and acceptor. We have used κ^2 as the commonly used relative orientation parameter between donor and acceptor. Note the large sensitivity of the behavior of FRET to both distance and orientation which has not been elucidated before. As outlined in table II, the perfect metal reflector can surprisingly inhibit or enhance FRET and even have no effect depending on the orientations and distances achieved in experiment.

(2) ***Realistic Metal*** For the case of realistic losses, the FRET figure of merit across wavelengths has the form

$$F_{ET} = \frac{[(\epsilon_2' + \epsilon_1) + q]^2}{|\epsilon_2 + \epsilon_1|^2} + \frac{\epsilon_2''^2(1+\Omega)^2}{|\epsilon_2 + \epsilon_1|^2} \tag{5.12}$$

where $q = \Omega(\epsilon_2' - \epsilon_1)$ is a Fano-like parameter and $\Omega = (r^3/r'^3)(\kappa'/\kappa)$ is an orientation/distance parameter. The first term, which corresponds to a dispersive dipole-dipole interaction, resembles a Fano resonance profile. The second term which depends on ϵ_2'' is a dissipative dipole-dipole interaction with a Lorentzian-like profile. When losses are sufficiently low the Fano term dominates. The result is shown in Fig. 5.2-c, which shows the excellent agreement between the exact QED result and the

quasi-static expression [Eqn. (5.12)]. The same system can show regions of enhancement, suppression, and no effect depending on the wavelength of operation. These various regimes are explained by the image dipole model, as outlined in the perfect reflector case. In stark contrast, the Purcell factor for a realistic metal is approximately given by

$$F_p = 1 + \frac{3}{16}\frac{\epsilon_1\epsilon_2''}{|\epsilon_1+\epsilon_2|^2}\frac{\kappa'}{(k_1 z_D)^3} \tag{5.13}$$

which is always enhanced in the near-field ($F_p > 1$). We now contrast the fundamental differences between the Purcell factor and FRET rate enhancement factor at the SP resonance ($\epsilon_2' = -\epsilon_1$). Eqn. (5.12) reduces to

$$F_{ET} = 4\frac{\kappa'^2 r^6}{\kappa^2 r'^6}\left(\frac{\epsilon_1}{\epsilon_2''}\right)^2 + \left(1+\frac{\kappa' r^3}{\kappa r'^3}\right)^2. \tag{5.14}$$

where we identify the quantity $Q = \epsilon_1/\epsilon_2''$ as the quality factor of the SP resonance. Similarly, eqn. (5.13) reduces to

$$F_p = 1 + \frac{3}{32\pi^3 n_1^3}\left(\frac{\lambda_D}{z_D}\right)^3\left(\frac{\epsilon_1}{\epsilon_2''}\right) \tag{5.15}$$

at the SP resonance. Note these expressions separate the material and geometrical properties of the system. Furthermore, the Purcell factor follows the well-known linear dependence on the quality factor while F_{ET} is dependent on the square of the quality factor.

We now use (5.14) and (5.15) to shed light on why Purcell factor enhancements have always shown large values in comparison to FRET rate enhancements (see table I). The key distinction between the two figures of merit lies in the difference in length scales captured by the r^6/r'^6 and λ_D^3/z_D^3 terms. For the half-space problem that we have considered here, geometric considerations imply that the donor-acceptor distance (r) is always smaller than the image-acceptor separation (r'). This drastically reduces the FRET figure of merit due to the sixth power dependence. The length scale factor of spontaneous emission, on the other hand, depends on the ratio of the wavelength of emission to the emitter distance from environment (λ_D^3/z_D^3) and is always much larger than 1 in the near-field. The cubed power dependence helps enhance the overall

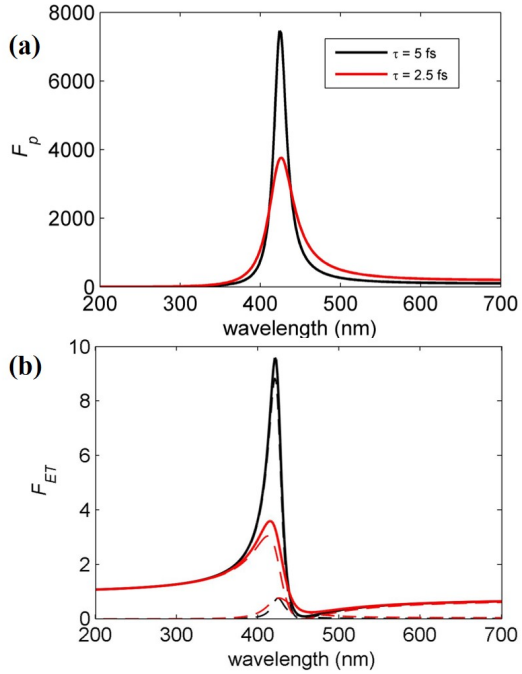

Fig. 5.3. **Effect of losses**. **(a)** Purcell factor F_p. **(b)** FRET figure of merit F_{ET}. Bottom half-space is modelled as Drude metal with $\omega_p = 6.3 \times 10^{15} s^{-1}$ and the Drude relaxation time of $\tau = 5fs$ (black) and $\tau = 2.5fs$ (red). Dashed lines correspond to the two terms, dispersive dipole-dipole interaction and dissipative dipole-dipole interaction, in Eqn. (5.12). Note the FRET enhancement factor is in general much smaller than the Purcell factor in agreement with widely reported observations.

Purcell factor and so in general we find that regardless of the material quality factor, the FRET figure of merit will be much smaller than the Purcell factor for metals with low material quality factors. In Fig. 5.3, we compare the Purcell factor and FRET enhancement factors across wavelengths which re-emphasizes this important point. Note that this explains the multitude of experiments which have observed negligible enhancements of the FRET rate as opposed to the SE rate (See Table 5.1).

5.4.1 (3) *Dielectric*

We now consider medium 2 as a dielectric ($\epsilon_2 > 0$). In this case, there are three general scenarios that may occur. (i) If $\epsilon_1 \approx \epsilon_2$ then the magnitude of the image dipole moment approaches zero and $F_{ET} \approx 1$. (ii) If $\epsilon_2/\epsilon_1 \gg 1$ then the dielectric acts like a perfect reflector with the different regimes outlined in the previous section. (iii) If $\epsilon_2/\epsilon_1 \ll 1$ then the image dipole flips orientation and the dielectric acts like a perfect reflector with opposite regimes to those outlined in Table II.

5.5 FRET efficiency

We now place limits on the FRET efficiency based on the quantum yield of the donor and elucidate fundamental competition between FRET efficiency and the Purcell factor. The efficiency of energy transfer to the acceptor location as compared to the energy transfer to the rest of the environment is given by

$$\eta_{et} = \frac{\Gamma_{DA}}{\gamma_D + \Gamma_{DA}}. \tag{5.16}$$

In many applications and experiments, controlling the FRET efficiency is as important as controlling the FRET rate hence we introduce the FRET efficiency figure of merit:

$$\begin{aligned} F_{eff} &= \frac{\eta_{et}}{\eta_o} \\ &= \frac{F_{ET}}{F_{ET}\eta_o + [(1-Q_D) + Q_D F_p](1-\eta_o)} \end{aligned} \tag{5.17}$$

where the denominator in the first line denotes the FRET efficiency in a homogeneous environment. It then follows that the condition of FRET efficiency enhancement ($F_{eff} > 1$) is

$$F_{ET} > (1 - Q_D) + Q_D\, F_p \tag{5.18}$$

which shows that the intrinsic quantum efficiency of donors (Q_D) has a large effect on the FRET efficiency.

5.5.1 (1) High-yield donor ($Q_D \approx 1$)

From the equations above, the condition to increase the FRET efficiency for high yield donors requires the FRET rate enhancement factor to be larger than the Purcell factor.

$$F_{eff} > 1 \implies F_{ET} > F_p \tag{5.19}$$

Our analysis from the previous section shows that this condition is very difficult to achieve for realistic metals. Using (5.14) and (5.15), we find that the minimum quality factor required to observe ($F_{ET} > F_p$) is given by

$$Q > \frac{3}{128\pi^3 n_1^3}\left(\frac{\lambda_D}{z_D}\right)^3 \frac{\kappa^2 r'^6}{\kappa'^2 r^6}. \tag{5.20}$$

For a donor-acceptor pair that is equidistant from the metal surface, the minimum quality factor can range from 10^3 and upwards. Since this value is not found in realistic metals, it is generally the case that FRET efficiency cannot be enhanced with high-yield donors explaining experimental observations.

5.5.2 (2) Low-yield donor

Using realistic parameters for metal-based systems (e.g $F_p \approx 10$ and $F_{ET} \approx 4$), we find that the intrinsic quantum efficiency must be less than 33% in order to observe FRET efficiency enhancement. This implies that low quantum yield donors will exhibit an increase in the FRET efficiency even if $F_p > F_{ET}$. We emphasize that this explains why many plasmonic-based experiments with metallic nanoparticles have observed enhancements in the FRET efficiency [103, 139, 140]. However, note that if $F_p \gg F_{ET}$ then there will no efficiency enhancement even with a low quantum yield donor.

5.6 FRET near a nanosphere

We now turn our attention to the effect of FRET near spherical nanoparticles, as has been the focus of a wide range of experiments [see Table I]. Our effective near-field dipole model captures the observed effects of FRET near these structures, in full agreement with the QED result. In the quasistatic regime, $kR \ll 1$, the nanoparticle can be treated as a dipole-driven multipolar source that acts to modify the overall FRET rate. For accurate predictions, we have used the full dyadic Green function for spherically multilayered media originally developed in ref. [141] (see the Appendix towards the end of this Chapter).

In Fig. 5.4-a, we compare the FRET rate enhancement factor with the Purcell factor for a donor-acceptor pair that has a fixed separation distance of 8 nm across the visible wavelength region. We consider a silver nanoparticle with a 10 nm radius. Two distinct peaks are observed in the spectrum. The peak at lower frequencies is the result of the dipolar surface plasmon resonance of the nanoparticle, while the second peak at higher frequencies is the result of the high-order (non-radiative) modes in the nanoparticle. Note that the Purcell factor (F_p) is orders of magnitude larger than the FRET rate enhancement factor (F_{ET}) near these resonant regions, in agreement with our previous arguments. Note, however, that in the low-frequency region the two factors became comparable in magnitude. Most interestingly, when the donor and acceptor are tangential to the surface of the sphere, the FRET rate is enhanced ($F_{ET} > 1$) while the Purcell factor is suppressed ($F_p < 1$).

In Fig. 5.4-b, we compare F_{ET} and F_p as a function of separation distance from the nanoparticle for an operating wavelength of 650 nm. Note that unlike the planar half-space case, the Purcell factor of a tangential dipole can be suppressed for certain distances. We emphasize that the FRET characteristics from the effective dipole model given in Table II captures the distance and orientation dependence completely in this spherical geometry.

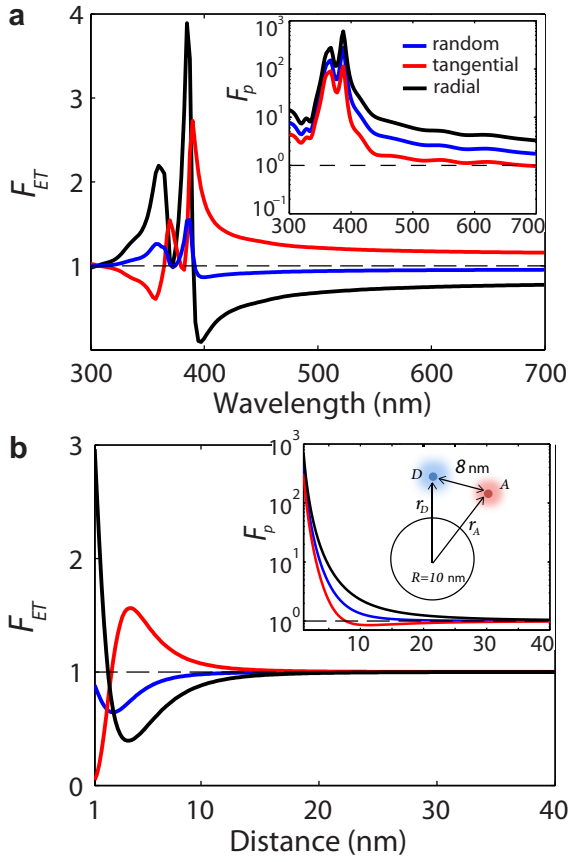

Fig. 5.4. **FRET near nanosphere. (a)** FRET rate enhancement factor for spherical nanoparticle systems widely used in experiment. The donor and acceptor are both 8 nm away from an Ag nanosphere of 10 nm radius. Inset: Calculated Purcell factor for same system. The peaks are related to dipolar surface plasmon resonance and higher order multipolar non-radiative modes. We emphasize that $F_p \gg F_{ET}$ for plasmonic systems near the LSP resonance implying the energy transfer to the sphere (environment) is larger than the energy transfer to the acceptor. **(b)** Distance dependence of F_{ET} and F_p at the 650 nm wavelength region (away from resonance). Note that a tangential dipole exhibits a suppression in the Purcell factor due to near-field interference effects. This effect can be used to boost the FRET efficiency ($F_{eff} \propto F_{ET}/F_p$). The enhancement, suppression and null effect features in the three curves of different colors corresponding to the orientations of the dipole moments of the acceptor and donor are in agreement with table I.

In Fig. 5.5, we directly compare the ratio of F_{ET} and F_p which dictates the FRET efficiency enhancement as outlined in the previous section. We consider the case shown in the inset of Fig. 5.4-b, but with a nanoparticle with 40 nm radius. Note that in the quasi-static regime, a larger radius enhances all of the figures of merit since they are directly related to the polarizability of the nanoparticle. This can be seen from the dipole contribution of the nanoparticle which has a polarizability of $\alpha = 4\pi\epsilon_o R^3 \frac{(\epsilon_2-\epsilon_1)}{(\epsilon_2+2\epsilon_1)}$. In Fig. 5.5-a, we find that there exists an optimum separation distance where $F_{ET}/F_p \approx 2.7$ which occurs only for the case when the donor and acceptor have dipole moments oriented tangential to the spherical nanoparticle (co-tangential case). We therefore suggest the implementation of co-tangential dipoles as an important design principle for enhancing the FRET efficiency for future experiments.

Finally, in Fig. 5.5-b we present an all-dielectric platform for enhancing the FRET efficiency. We consider a dielectric nanosphere with $\epsilon_2 = 6.25$ and 40 nm radius. Here, the ratio is shown to be as large as $F_{ET}/F_p \approx 2.45$. We note that the overall enhancement of the efficiency is mainly due to the suppression of the Purcell factor $F_p \approx 0.48$ and a moderate enhancement in the FRET rate $F_{ET} \approx 1.2$. We emphasize that while the FRET rate can be drastically enhanced near resonances with large quality factors, the Purcell factor will be simultaneously enhanced as well. As a result, enhancing the FRET efficiency will be difficult to achieve near resonances since most of the energy from the donor is funneled to the environment (nanoparticle) and not the acceptor. However as we have shown in Fig. 5.5, away from resonances we find that engineering the FRET efficiency can result from the modification of the quasi-static fields. In essence, the nanosphere platform allows a simultaneous suppression of the Purcell factor while also enhancing the FRET rate close to the nanoparticle. Moreover, the material parameters become irrelevant away from resonance whereas the orientation and the geometrical parameters play a much more important role.

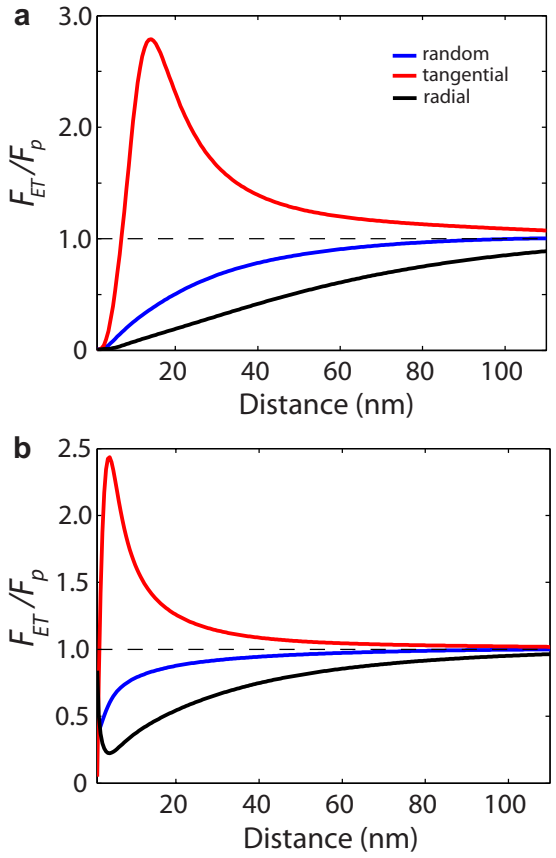

Fig. 5.5. **FRET efficiency.(a)** FRET efficiency enhancement occurs when $F_{ET}/F_p > 1$. We show that this ratio can be optimized for particular distances away from the nanoparticle. Results are shown for same set-up as Fig. 5.4-b but with a $R = 40$ nm nanoparticle. **(b)** Counter-intuitive to prevalent designs, here we provide an all-dielectric design to engineer FRET efficiency using a transparent nanosphere ($\epsilon_2 = 6.25 > 0$) and 40 nm radius. The efficiency enhancement in FRET implies a larger fraction of the donor energy is transferred to the acceptor in presence of the nanosphere. This effect arises from suppression of the Purcell factor which is necessary to avoid energy transfer to the environment.

5.7 Comparison to experiments

To provide a conclusive settlement to the debate surrounding FRET, we use our theory to explain recent experiments which have found that FRET intriguingly is not

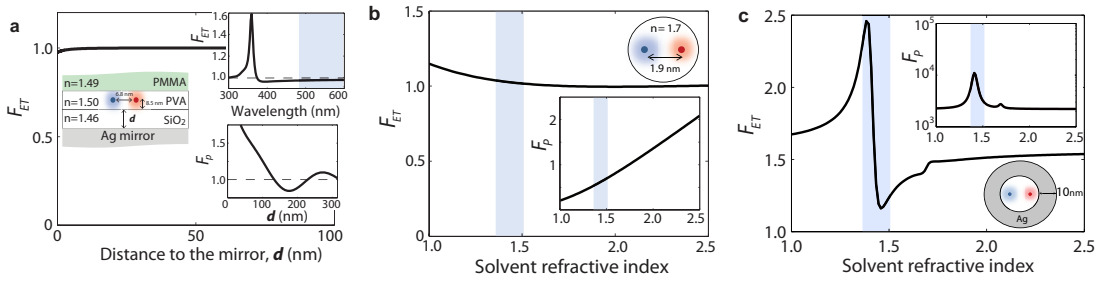

Fig. 5.6. **Comparison to experiments. (a)** Theoretical comparison to experiment in ref. [115]. The system configuration is shown in the inset. The FRET figure of merit is theoretically calculated to be $F_{ET} \approx 1$ for a wide range of separation distances **d** from the mirror, in agreement with the experiment (plotted at the donor's peak emission wavelength of 525 nm). Theoretical Purcell factor F_p shows excellent agreement with experimental results (lower inset). However, using our theoretical model, we predict a drastic change in the FRET FOM near the Ag SPP resonance in the limit $\mathbf{d} \to 0$ (top inset). This shows that FRET rate can be modified for the same experiment if the regime is modified. **(b)** Theoretical comparison to experiment in ref. [116]. The donor-acceptor pair is embedded inside a nanocrystal (4 nm diameter) with assumed refractive index $n = 1.7$ ($LaPO_4$). By varying the refractive index of the surrounding medium, we find that $F_{ET} \approx 1$ in agreement with our analysis. Note that we also predict the linear dependence of the Purcell factor as measured in the experiment (inset). **(c)** However, we predict that a silver-coated nanocrystal would produce a drastic change in the FRET FOM as well as the Purcell factor. This result would require the donor-acceptor overlap spectrum to lie around the 400 nm wavelength range. Note that the above results clearly show that FRET can be engineered by the environment even though it is extremely difficult in comparison to modifying spontaneous emission. The dyadic Green function formalism and results from QED theory were used to calculate all results and parameters were obtained from the experiments.

affected by the environment. Our goal is to show that this is not universal behavior. Our theory explains the experimental results while simultaneously pointing to regimes in the same experiment where FRET rate enhancement or suppression can occur. We have carefully isolated the experimental parameters of interest from the relevant works for theoretical consideration below.

We first turn to the planar multilayer system considered in [115] which showed a null result of the environment on FRET. Our theory shows that this result is specific to the experimental parameters considered. The multilayer structure is shown in the inset of Fig. 5.6 consisting of a half cavity system. The donor-acceptor pairs are separated by a distance d from a Ag mirror. In the experiment, the distance from the mirror is varied in order to study the environmental influence on FRET. By using a transfer matrix method as well as the GF formalism, we calculated the FRET figure of merit for the exact configuration in the experiment. Here, we show that our results capture the Purcell factor variation and match exactly with the observed null effect in the FRET rate. There are two reasons contributing to the no-effect result: (i) the separation distance between the donor-acceptor pair and the mirror is far too large to influence the quasi-static fields, and (ii) the surface plasmon resonance lies near the UV region which is outside the spectral overlap region of the donor-acceptor pair. We show that if the same experiment is repeated with donor-acceptor spectra in the UV region, the SPP resonance would surely have an effect on FRET. This plasmonic resonance could be tailored with surface layers or metamaterials to overlap with the relevant spectrum of FRET.

We also conclusively explain a more recent experiment [116] consisting of a donor-acceptor pair inside a $LaPO_4$ nanocrystal with 4 nm diameter (see inset Fig. 5.6-c which again showed the null result of the environment on the FRET rate. A change in the environment was achieved by dispersing the nanocrystals in solvents with different refractive indices. The range of the refractive index change in the experiment is highlighted in the blue region. Our theory predicts that for the exact range of solvent refractive indices considered in the experiment, FRET is unchanged in agreement with experiment. We note that our calculations for the SE rate enhancement also show the same linear dependence that was observed in the experiment (see Fig. 5.6-b inset) reinforcing our results. However, closer inspection reveals that changing the refractive indices beyond this range should have a clear effect on FRET. In Fig. 5.6-c, we propose a new experimental set-up where the nanocrystal has a 10 nm

silver coating. We have calculated the results for a 400 nm operating wavelength to elucidate the role of the resonances. It is striking that a subtle change in the exact same environment leads to a large variation in the FRET enhancement factor across the identical solvent index range that was probed in the experiment.

We now consider the FRET-nanoparticle experiment of [103] which consisted of a donor-acceptor pair with a fixed separation distance of 9.2 nm placed at a fixed position away from a silver nanoparticle with 10 nm radius. Our results help to identify the dipole moment orientation dependence of the observations and also point to mechanisms beyond conventional weak-coupling QED FRET theory. Based on the single-exponential lifetime fits from the experiment, the authors measured a donor lifetime enhancement of $\gamma_D/\gamma_D^o = 2.35$, a FRET rate enhancement of $\Gamma_{DA}/\Gamma_{DA}^o = 29.4$ and an overall FRET efficiency enhancement of $F_{eff} = 5.3$. The donor molecule had a peak emission wavelength at 662 nm. The trends of the theoretical figures of merit will be very similar to those in Fig. 5.4-b. For our simulation, we assumed that the donor and acceptor were both 4.5 nm away from the nanoparticle. We provide the overall results in the following table for various orientations. In the table, F_{ET} and F_p

	F_{ET}	F_p	Q_D	F_{eff}
co-tangential	1.58	3.8	0.48	1.13
co-radial	0.39	13.9	0.11	0.15
random	0.72	7.2	0.22	0.41

were calculated independently based on the parameters mentioned above. The intrinsic quantum yield Q_D is used as a fitting parameter to reproduce the experimental decay rate enhancement $\gamma_D/\gamma_D^o = 2.35$. The theoretical FRET efficiency enhancement factor can be obtained using (5.17) with an initial FRET efficiency of $\eta_o = 0.12$, given in [103]. As we can see from the table, the co-tangential FRET case is the only one able to reproduce the FRET efficiency enhancement seen in the experiment. Since the radial and random cases are in extreme disagreement with the experimental results, this might suggest that the measured lifetime values consisted primarily

of the co-tangential dipole contribution. Such preferred orientations can arise from steric effects of ligands that attach the donor and acceptor to the nanoparticle. We must emphasize that the low quantum yield of the donor is an important factor in the observed FRET efficiency enhancement – in agreement with our previous arguments. Moreover, while the co-tangential case provides qualitative agreement with the experiment, the theoretical values of $F_{ET} = 1.58$ and $F_{eff} = 1.13$ vastly underestimate the experimental values of $\Gamma_{DA}/\Gamma^{o}_{DA} = 29.4$ and $F_{eff} = 5.3$ reported in the experiment. Since our current theory provides the upper bound for a weak-coupling model, these experimental results are suggestive of more exotic physical phenomena that would influence the overall energy transfer rate. The possibilities include surface roughness-induced plasmonic hot-spots that increase the two-point Green function, non-adiabatic effects, or coherent-like effects in energy transfer [142].

At this point, it is important to consider some of the approximations that were made in the QED derivation of the FRET rate. The two primary approximations consists of: (1) weak-coupling and Markovian approximation, and (2) the dipole approximation. Since going beyond these approximations is beyond the scope of the current work, it would be interesting to see in the future how the transition to the strong coupling regime affects FRET in inhomogeneous environments, as well as how finite-size emitters affects FRET. The bounds we have established for the FRET efficiency in the weak-coupling regime will be important to identify new pathways of energy transfer such as quantum coherence in photosynthesis [142].

5.8 Chapter Summary

In conclusion, we have shown that the environment modifies dipole-dipole interactions and FRET which can be captured by an effective near-field dipole model. We have clearly isolated the regimes which show enhancement, suppression and no effect on the FRET rate settling the long-standing debate surrounding FRET. Finally, we also conclusively explained several recent experiments that examined the role of the

environment of FRET. Engineering FRET is fundamental to multitude of applications from energy harvesting to molecular sensing and our theory provides intuitive insight unavailable up until now.

Chapter appendix

Orientational Averaging Here, we provide the generalized coordinate-free trace formulas for orientational averaging. The relevant quantity for the local density of states is given by

$$\langle \mathbf{n}_D \cdot \mathbf{G}(r_D, r_D) \cdot \mathbf{n}_D \rangle_D = \frac{1}{3} \operatorname{Tr}[\mathbf{G}(r_D, r_D)]. \tag{5.21}$$

Similarly, one can show that the relevant quantity for FRET is given by:

$$\langle |\mathbf{n}_A \cdot \mathbf{G}(r_A, r_D) \cdot \mathbf{n}_D|^2 \rangle_{D,A} = \frac{1}{9} \operatorname{Tr}[\mathbf{G}^\dagger(r_A, r_D)\mathbf{G}(r_A, r_D)] \tag{5.22}$$

where $\langle\,\rangle_{D,A}$ denotes orientational averaging over donor and acceptor orientations, and † denotes the hermitian conjugate.

Spherical nanoparticle System We provide details of the calculation for a spherical nanoparticle system. The formulation of the scattered dyadic Green function in spherically multilayered media was originally cast in [141]. For self-consistency, we provide the results here in terms of a single summation rather than the double summation originally shown in [141]. The simplification is achieved through the use of Legendre addition rules.

$$G_{rr} = \frac{ik_1}{4\pi} \sum_{n=1} n(n+1)(2n+1) \frac{h_{1a} h_{1d}}{\rho_{1a} \rho_{1d}} P_n(\cos\theta) R_p^f \tag{5.23}$$

$$G_{r\theta} = \frac{ik_1}{4\pi} \sum_{n=1} (2n+1) \frac{h_{1a} h'_{1d}}{\rho_{1a} \rho_{1d}} P'_n(\cos\theta) \sin\theta \, R_p^f \tag{5.24}$$

$$G_{\theta r} = \frac{ik_1}{4\pi} \sum_{n=1} (2n+1) \frac{h'_{1a} h_{1d}}{\rho_{1a} \rho_{1d}} P'_n(\cos\theta) \sin\theta \, R_p^f \tag{5.25}$$

$$\begin{aligned} G_{\theta\theta} = \frac{ik_1}{4\pi} \sum_{n=1} (2n+1) \Bigg\{ & \frac{h_{1a} h_{1d}}{n(n+1)} P'_n(\cos\theta) \, R_s^f + \\ & \frac{h'_{1a} h'_{1d}}{\rho_{1a} \rho_{1d}} \left(P_n(\cos\theta) - \frac{P'_n(\cos\theta)\cos\theta}{n(n+1)} \right) R_p^f \Bigg\} \end{aligned} \tag{5.26}$$

$$G_{\phi\phi} = \frac{ik_1}{4\pi}\sum_{n=1}(2n+1)\left\{\frac{h'_{1a}h'_{1d}}{\rho_{1a}\rho_{1d}}\frac{P'_n(\cos\theta)}{n(n+1)}R_p^f + h_{1a}h_{1d}\left(P_n(\cos\theta) - \frac{P'_n(\cos\theta)\cos\theta}{n(n+1)}\right)R_s^f\right\} \tag{5.27}$$

where $\theta = \theta_D - \theta_A$, $\rho_{kl} = k_k r_l$, $k_k = \sqrt{\epsilon_k}\omega/c$, and $G_{ij} = \mathbf{e}_{i_A}\mathbf{G}(r_A, r_D)\mathbf{e}_{j_D}$. Note that we have used the simplified notation $h_{kl} = h_n^{(1)}(\rho_{kl})$ and $h'_{kl} = \frac{d[\rho_{kl}h_n^{(1)}(\rho_{kl})]}{d\rho_{kl}}$ where $h_n^{(1)}(\rho)$ is the spherical hankel function of the first kind. The indices i, j correspond the spherical coordinates r, θ, ϕ; the index $k = 1, 2$ corresponds to outer medium and inner medium with respect to sphere; and the index $l = d, a$ correspond to donor and acceptor respectively. R_p^f and R_s^f denote the centrifugal reflection coefficients for TM and TE polarized light as outlined in [141].

In the quasistatic regime, one can approximate these results to get an expression for the FRET FOM in terms of a dipole-driven multipolar source. For radial dipoles, the FRET figure of merit takes the form:

$$F_{ET} = \left|1 + \frac{r^3}{\kappa}\sum_{n=1}\frac{(n+1)^2\tilde{\alpha}_n P_n(\cos\theta_A)}{r_A^{n+2}r_D^{n+2}}\right|^2. \tag{5.28}$$

where $\tilde{\alpha}_n$ is the renormalized polarizability for the nth mode of the nanoparticle

$$\tilde{\alpha}_n = \alpha_n\left[1 - i\frac{\alpha_n(n+1)k_1^{2n+1}}{n(2n-1)!!(2n+1)!!}\right]^{-1} \tag{5.29}$$

and

$$\alpha_n = \frac{n(\epsilon_2 - \epsilon_1)}{n\epsilon_2 + (n+1)\epsilon_1}R^{(2n+1)}. \tag{5.30}$$

The resonant frequency of the nth mode is $\omega_n = \sqrt{n}\omega_p/\sqrt{n\epsilon_\infty + (n+1)\epsilon_1}$. Similar expressions can be derived for other dipole orientations.

6. FUNDAMENTAL EFFICIENCY BOUND FOR COHERENT ENERGY TRANSFER IN NANOPHOTONICS

In this Chapter, we ask the question of whether quantum coherence and entanglement can enhance energy transfer efficiency in a nanophotonic environment. To obtain a formal answer, we derive a unified quantum theory of coherent and incoherent energy transfer between two atoms (donor and acceptor) valid in arbitrary Markovian nanophotonic environments. Our theory predicts a fundamental bound $\eta_{max} = \frac{\gamma_a}{\gamma_d+\gamma_a}$ for energy transfer efficiency arising from the spontaneous emission rates γ_d and γ_a of the donor and acceptor. We propose the control of the acceptor spontaneous emission rate as a new design principle for enhancing energy transfer efficiency. We predict an experiment using mirrors to enhance the efficiency bound by exploiting the dipole orientations of the donor and acceptor. Of fundamental interest, we show that while quantum coherence implies the ultimate efficiency bound has been reached, reaching the ultimate efficiency does not require quantum coherence. Our work paves the way towards nanophotonic analogues of efficiency enhancing environments known in quantum biological systems.

6.1 Motivation: energy transfer in photosynthesis

Energy transfer is typically distinguished as incoherent Förster-type resonance energy transfer (FRET), or coherent excitation energy transfer. The two regimes occur in the limits, $J_{dd}/\gamma_{tot} \ll 1$ and $J_{dd}/\gamma_{tot} \gg 1$, involving the ratio of the electronic dipole-dipole coupling J_{dd} to the total linewidth γ_{tot} of each molecule. The total linewidth is a measure of the coupling strength to the bath's spin, vibrational or electrodynamic degrees of freedom. In photosynthetic systems, the system-bath

coupling is primarily dominated by vibrations. The complex nature of photosynthetic systems results in electronic and vibrational coupling strengths varying greatly between the incoherent and coherent coupling limits. Understanding the role of the environment from the weak-to-intermediate-to-strong coupling regimes has been an important topic of interest required to explain experimental observations [143]. In this regard, there has been tremendous progress in the development of a wide variety of open quantum system frameworks (modified-Redfield, Hierarchical equations of motion, Polaron-modified master equation) [144–150] that operate under a wide range of coupling strengths. While a complete understanding of photosynthetic energy transfer has not been achieved [151], there has been a lot of progress outlining how the environment can positively influence energy transfer efficiency [144–150, 152–156]. Understanding the fundamental role of quantum coherence remains an open problem in photosynthesis, and it is still not clear whether it does play a role [157, 158]. It is possible that other guiding principles give rise to near-unity efficiencies in photosynthesis.

Precise control of resonance energy transfer has also emerged as a fundamental topic of interest in the nanophotonic community. There has been a multitude of theoretical [57, 123, 132, 134, 159] and experimental [99, 103, 104, 109, 113, 115, 116] work proposing and demonstrating nanophotonic control of energy transfer with plasmonic, optical waveguide, and cavity-based systems. Unlike work in the photosynthetic community, most nanophotonic theories of energy transfer have relied on classical electrodynamic descriptions or perturbative approaches based on Fermi's golden rule. While some authors have provided rigorous quantum electrodynamic formulations, the final analytical expressions are typically valid in either the weak or strong coupling regimes [42, 86, 127]. Moreover, a proper definition of the energy transfer efficiency has been lacking in nanophotonics where most results use Förster's perturbative expression.

In this Chapter together with Appendix B, we combine ideas from both communities to develop an exactly solvable theory for resonance energy transfer from

first-principles. We derive a quantum master equation providing a unified picture of energy transfer dynamics in the coherent and incoherent coupling regimes applicable in arbitrary Markovian nanophotonic environments. We then solve the model exactly to derive a simple analytical expression for the energy transfer efficiency. Our result provides insight into the role of finely-tuned coupling strengths, dephasing rates, and detuning between the donor and acceptor required to achieve near-unity energy transfer efficiencies. The central result of this Chapter is the ultimate efficiency of

$$\eta_{max} = \frac{\gamma_a}{\gamma_d + \gamma_a}. \tag{6.1}$$

This provides a fundamental limit to the energy transfer efficiency between two atoms regardless of coupling strength, quantum coherence and spectral overlap. It also implies the condition $\gamma_a \gg \gamma_d$ is required to achieve near-unity efficiency with the corollary that two identical atoms will have a maximum efficiency of 50%. To the best of our knowledge, this surprisingly simple and intuitive result has not been discussed nor derived in the resonance energy transfer literature. We emphasize this fundamental bound will also apply to quantum transport in the two-chromophore system relevant to many biological systems.

Interestingly, this bound suggests the acceptor spontaneous emission rate can be used as a new degree of freedom to control energy transfer. To illustrate the interplay of these effects, we predict an experiment to control the efficiency between two atoms above a mirror. We also show that while quantum coherence implies the ultimate efficiency bound has been reached, reaching the ultimate efficiency does not require quantum coherence. Ultimately, these results will enable the design of nanophotonic systems which can mimic quantum biological environments to enhance energy transfer efficiency.

6.2 Perturbative energy transfer efficiency

The efficiency of energy transfer is conventionally defined as the ratio of the energy transfer rate Γ_{da} to the total dissipation rate of the donor,

$$\eta_{et} = \frac{\Gamma_{da}}{\Gamma_{da} + \gamma_d}.$$

In free-space, the spontaneous emission rate of the donor is $\gamma_d = d_d^2\omega^3/(3\pi\hbar\epsilon_o c^3)$. The energy transfer rate is $\Gamma_{da} = \frac{2\pi}{\hbar^2}|V_{dd}|^2\mathcal{J}_{da}$ where $\mathcal{J}_{da}$ is the spectral overlap integral of the donor emission and acceptor absorption. The resonant dipole-dipole interaction (RDDI), $V_{dd} = \hbar(-J_{dd}+i\gamma_{dd}/2) = \frac{\omega^2}{\epsilon_o c^2}\mathbf{d}_a\cdot\mathbf{G}(\mathbf{r}_a,\mathbf{r}_d,\omega)\cdot\mathbf{d}_d$, defines the magnitude of the dipole-dipole coupling. The results are written in terms of the dyadic Green function $\mathbf{G}(\mathbf{r}_a,\mathbf{r}_d,\omega)$ containing both near-field Coulombic and far-field radiative contributions. These definitions of the spontaneous emission and energy transfer rates are based on Fermi's Golden rule valid in the incoherent limit. From these relations, we observe that increasing dipole-dipole coupling ($|V_{dd}| \rightarrow \infty$) results in a near-unity energy transfer efficiency, and therefore no fundamental bound exists.

6.3 Non-perturbative energy transfer efficiency

In this Chapter, we follow the extensive work of photosynthetic excitation energy transfer [160, 161] and use the following definition for the energy transfer efficiency,

$$\eta_{et} = \gamma_a \int_0^\infty \rho_{aa}(t)dt, \tag{6.2}$$

valid for non-stationary processes such as when the donor is initially in its excited state. This result is general enough to work in the weak and strong coupling regimes between two atoms. Here, the energy transfer efficiency is proportional to the time-integrated luminescence originating from the acceptor. $\rho_{aa}(t)$ is the time-dependent density matrix population of the acceptor in the excited-state. For many applications, this is a much more useful and intuitive definition for the energy transfer efficiency.

In Appendix B, we derive the RDDI master equation for two non-identical atoms of the form, $\frac{\partial}{\partial t}\rho = i[\rho, H_{coh}] + \mathcal{L}[\rho]$, from first principles. The first term involves the

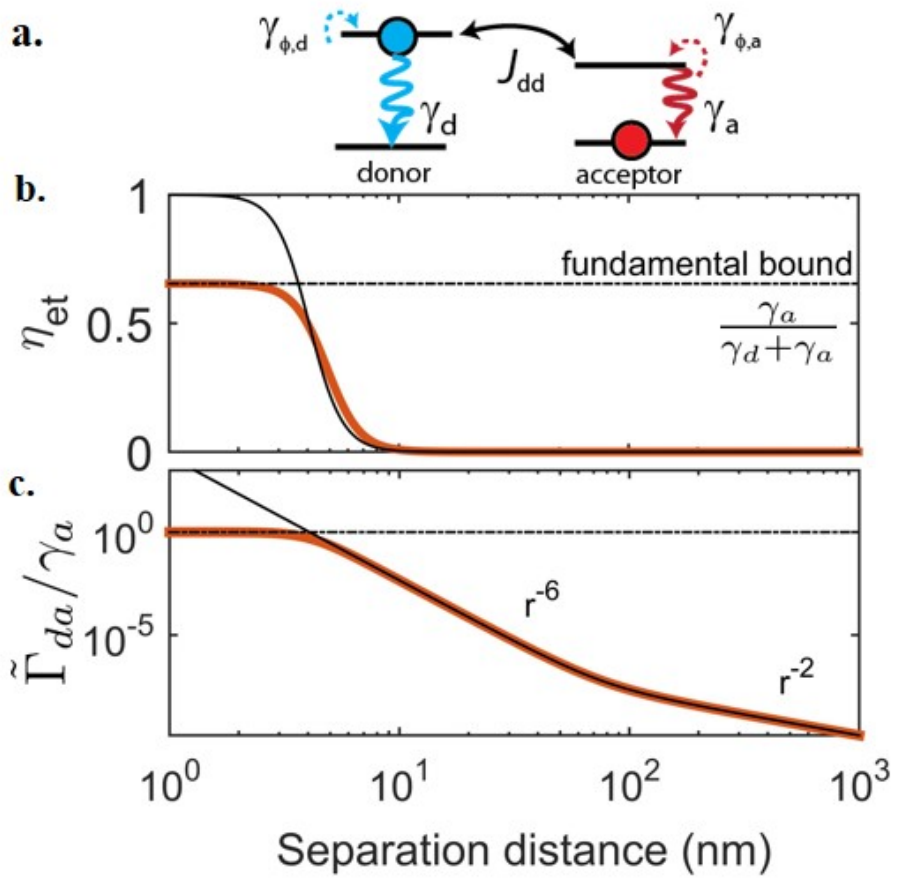

Fig. 6.1. (a) A donor initially in its excited-state will either transfer energy to an acceptor, or spontaneously emit light with rate γ_d. Once the energy is transferred to the acceptor, the energy can either return to the donor or escape into vacuum with rate γ_a. The energy transfer efficiency is defined as the total probability of an acceptor emitting the initial excitation as opposed to the donor. (b) Using this metric, we find the energy transfer efficiency will have a fundamental bound as the separation distance between two atoms decreases (orange curve), in stark contrast to the conventional definition for the FRET efficiency (black curve). (c) The result can also be understood in terms of the renormalized transfer rate $\tilde{\Gamma}_{da}$ (orange curve) having a fundamental bound as compared to the energy transfer rate Γ_{da}. We take $\gamma_a = 2\gamma_d$ giving an ultimate efficiency of $\eta_{max} = 2/3$.

coherent dynamics due to dipole-dipole coupling J_{dd}. The second term is a Lindblad superoperator describing the incoherent dynamics due to spontaneous emission and pure dephasing of the donor and acceptor respectively. For rest of the Chapter, we will ignore non-local cooperative decay γ_{dd} typically associated with superradiant and subradiant effects. We will explore these effects in a future paper. Our results are general enough to work in any Markovian bath with a correlation time τ_c that is much smaller than the relaxation times of the atoms, $\tau_c^{-1} \gg \gamma_d, \gamma_a, \Gamma_{da}$. This extends the range of applicability of this approach beyond the vacuum case, allowing the consideration of more complicated nanophotonic environments. Using the RDDI master equation, a central result of this Chapter is the exact analytical expression of the energy transfer efficiency valid in the coherent and incoherent coupling regimes,

$$\eta_{et} = \frac{\tilde{\Gamma}_{da}}{\tilde{\Gamma}_{da} + \gamma_d} \tag{6.3}$$

where we define the renormalized energy transfer rate,

$$\tilde{\Gamma}_{da} = \frac{\gamma_a \Gamma_{da}}{\gamma_a + \Gamma_{da}}. \tag{6.4}$$

Surprisingly, we recover the same functional form of Förster's perturbative energy transfer rate, $\Gamma_{da} = \frac{2\pi}{\hbar^2}|V_{dd}|^2 \mathcal{J}_{da}$, however, the master equation approach allows for an exact solution of the spectral overlap integral,

$$\mathcal{J}_{da} = \frac{(\gamma_d + \gamma_{\phi,d} + \gamma_a + \gamma_{\phi,a})/(2\pi)}{(\tilde{\omega}_d - \tilde{\omega}_a)^2 + (\gamma_d + \gamma_{\phi,d} + \gamma_a + \gamma_{\phi,a})^2/4}. \tag{6.5}$$

The overlap integral $\mathcal{J}_{da}$ is equal to the integral of two Lorentzians with resonant frequencies $\tilde{\omega}_d = \omega_d + \delta\omega_d$, $\tilde{\omega}_a = \omega_a + \delta\omega_a$ and linewidths $\gamma_d + \gamma_{\phi,d}$, $\gamma_a + \gamma_{\phi,a}$ respectively. Here, we introduce $\gamma_{\phi,i}$ as the phenomenological dephasing rate for each atom accounting for fluctuations in the transition frequency. The dephasing rate contributes to an observable linewidth broadening dominant in ambient temperatures where $\gamma_{\phi,i} \gg \gamma_i$.

While the functional form for the energy transfer rate Γ_{da} is similar to conventional FRET theory, this approach goes beyond the perturbative result by taking

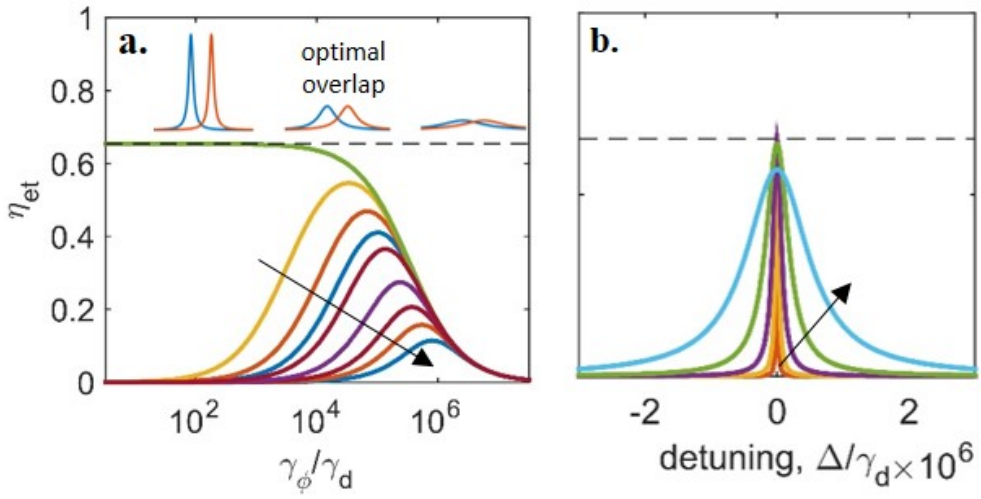

Fig. 6.2. Energy transfer efficiency as function of (a) dephasing rate γ_ϕ and (b) atom-atom detuning $\Delta = \tilde{\omega}_d - \tilde{\omega}_a$. Note the energy transfer efficiency always remains below the fundamental bound regardless of coupling strengths, spontaneous emission, dephasing or detuning. This bound may be reached asymptotically for the case of two atoms with zero detuning in the limit of small dephasing (green curve left). Black arrow denotes (a) increased detuning and (b) increased dephasing.

into account the modification of the resonant frequency and linewidth of each atom, $\delta\omega_i = -\frac{\omega^2}{\hbar\epsilon_o c^2}\mathbf{d}_i \cdot \mathrm{Re}\,\mathbf{G}(\mathbf{r}_i, \mathbf{r}_i, \omega) \cdot \mathbf{d}_i$ and $\gamma_i = \frac{2\omega^2}{\hbar\epsilon_o c^2}\mathbf{d}_i \cdot \mathrm{Im}\,\mathbf{G}(\mathbf{r}_i, \mathbf{r}_i, \omega) \cdot \mathbf{d}_i$, resulting in modified non-perturbative emission and absorption spectra for the donor and acceptor respectively. In general, the dyadic Green function consists of vacuum and scattered contributions, reinforcing the applicability of this approach to more complicated nanophotonic environments.

6.4 Ultimate energy transfer efficiency

The renormalized energy transfer rate (6.4) arises from the exact non-stationary solution for two non-identical atoms. The perturbative expression for the FRET efficiency can be recovered when $\Gamma_{da} \ll \gamma_a$. This condition suggests Förster's result is only valid when the acceptor has a fast enough dissipation rate to ensure irreversible

energy transfer. In realistic systems, the finite dissipation rate of the acceptor will result in a bottleneck effect. Energy cannot be transferred efficiently at a rate faster than the dissipation rate of the acceptor. In the limit of large dipole-dipole coupling, $|V_{dd}| \to \infty$, the renormalized transfer rate is bounded, $\tilde{\Gamma}_{da} \to \gamma_a$. The ultimate bound (6.1) for the energy transfer efficiency immediately follows.

The results for the non-perturbative efficiency η_{et} and the renormalized transfer rate $\bar{\Gamma}_{da}$ are shown in Fig. 6.1 for two atoms in vacuum as a function of separation distance. The renormalized transfer rate $\bar{\Gamma}_{da}$ has a r^{-6} inverse power law dependence until it reaches the bottleneck limit of γ_a, at which point the energy transfer efficiency reaches the fundamental bound. For comparison, we plot the energy transfer efficiency as would be predicted through Förster's expression (black line).

In Fig. 6.2, we provide numerical evidence of the robustness of this bound to atom-atom detuning $\Delta = \tilde{\omega}_d - \tilde{\omega}_a$ as well as dephasing. It is shown that the fundamental efficiency bound can be approached in the limit of zero detuning, $\Delta \to 0$. For large detuning, the energy transfer rate will decrease due poor spectral overlap in the absence of dephasing. As dephasing is increased (see Fig. 6.2-a) the energy transfer efficiency reaches a maximum when the following condition is satisfied

$$(\tilde{\omega}_d - \tilde{\omega}_a)^2 = (\gamma_d + \gamma_a + 2\gamma_\phi)^2/4. \tag{6.6}$$

Here, we have assumed equal dephasing for both atoms, $\gamma_\phi = \gamma_{\phi,d} = \gamma_{\phi,a}$. Condition (5) corresponds to the optimal emission-absorption spectral overlap. The use of dephasing to enhance efficiency is often referred to as environment assisted quantum transport (ENAQT).

6.5 Role of quantum coherence and entanglement

In general, quantum coherence occurs in the strong coupling regime, $|V_{dd}| \gg \gamma_d, \gamma_a, \gamma_\phi$. The strong coupling condition coincides with the condition, $|V_{dd}| \to \infty$, required to achieve the fundamental bound therefore any system with strong coupling and quantum coherence will operate at an efficiency equal to the fundamental bound

(1). However, we emphasize the opposite is not true: operating near the fundamental bound does not imply the system has quantum coherence. To demonstrate this effect, we show the population dynamics and efficiency of two distinct systems. We use Wootter's concurrence [162], $C = \max[0, \sqrt{\lambda_1} - \sqrt{\lambda_2} - \sqrt{\lambda_3} - \sqrt{\lambda_4}]$, to measure quantum entanglement. Here, λ_i are the eigenvalues of the operator $\rho(\sigma_y \otimes \sigma_y)\rho^*(\sigma_y \otimes \sigma_y)$ in descending order. A concurrence of 1 implies maximally entangled states while a concurrence of zero implies separable states with zero entanglement. Interestingly, for the non-stationary energy transfer problem the concurrence is exactly equal to the off-diagonal coherence, $C = 2|\rho_{ad}|$, therefore it serves as a measure of both coherence and entanglement. In fig 3-a, the system consists of a perfectly tuned donor-acceptor pair, $\Delta = 0$, with zero dephasing. This system achieves the ultimate efficiency of $\eta_{max} = 2/3$. The time-dependent concurrence (bottom plot) clearly shows quantum coherence is present in this system. In Fig. 6.3-b, we have two detuned atoms $\Delta/(2\pi) = 10$ THz with large dephasing $\gamma_\phi/(2\pi) = 4$ THz close to the necessary condition (5) for optimal spectral overlap. Interestingly, the second system exhibits irreversible energy transfer with negligible concurrence and therefore lacks quantum coherence but nevertheless reaches an efficiency that lies within 1 percent of the fundamental bound. The clear advantage of quantum coherence is that it reaches η_{max} for longer distances, $r = 45$ nm, while the detuned system requires a separation distance of $r = 4.5$ nm.

6.6 Nanophotonic control of fundamental efficiency bound

The fundamental bound (1) suggests a new design strategy for increasing the energy transfer efficiency based on control of donor and acceptor spontaneous emission rates. In figure 4, we present a canonical example illustrating how a nanophotonic environment can positively influence the energy transfer efficiency between two atoms using a non-resonant mirror eliminating the need for high-Q cavities. The basic idea is to use an orientation-dependent Purcell effect close to the mirror, understood

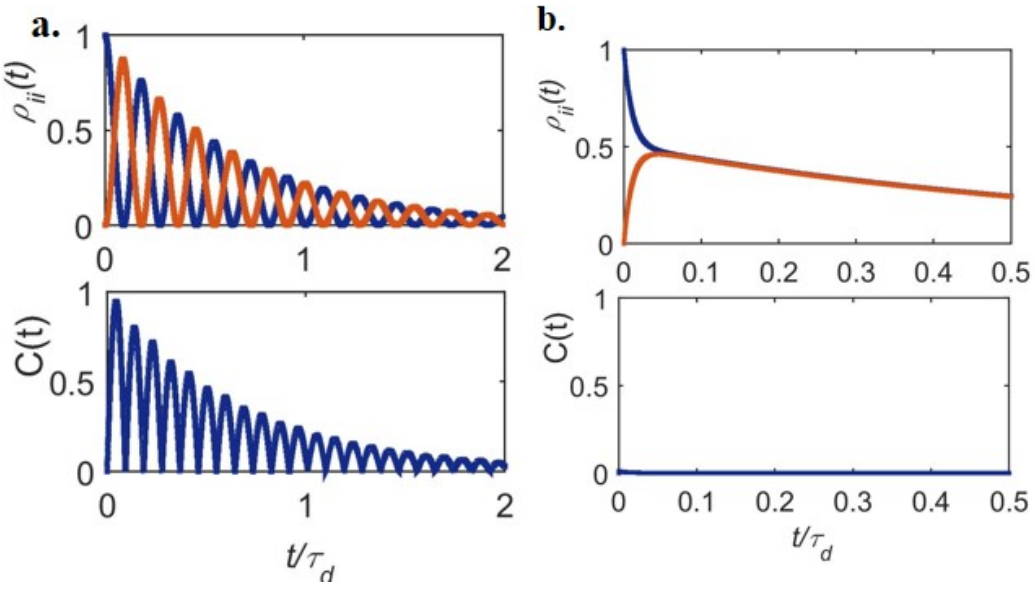

Fig. 6.3. Population dynamics of donor (blue) and acceptor (orange) as well as concurrence (bottom) used as a measure of quantum coherence. (a) Quantum coherent energy transfer between two atoms (r = 45 nm) operating at the ultimate efficiency $\eta_{max} = 2/3$. (b) Irreversible energy transfer between two atoms (r = 4.5 nm) operating within 1 percent of the ultimate efficiency exhibiting negligible quantum coherence.

through an image dipole model (inset). A parallel dipole close to a mirror will form an image dipole with the opposite orientation suppressing spontaneous emission, while a perpendicular dipole close to a mirror will form a collinear image dipole enhancing spontaneous emission. This suggests an ideal configuration where the donor is parallel and acceptor is perpendicular to the mirror surface (orange curve). The mirror-enhanced efficiency bound is reached at approximately 10 nm from the mirror. Note that this configuration is typically forbidden in free-space, but becomes possible due to image dipole formation.

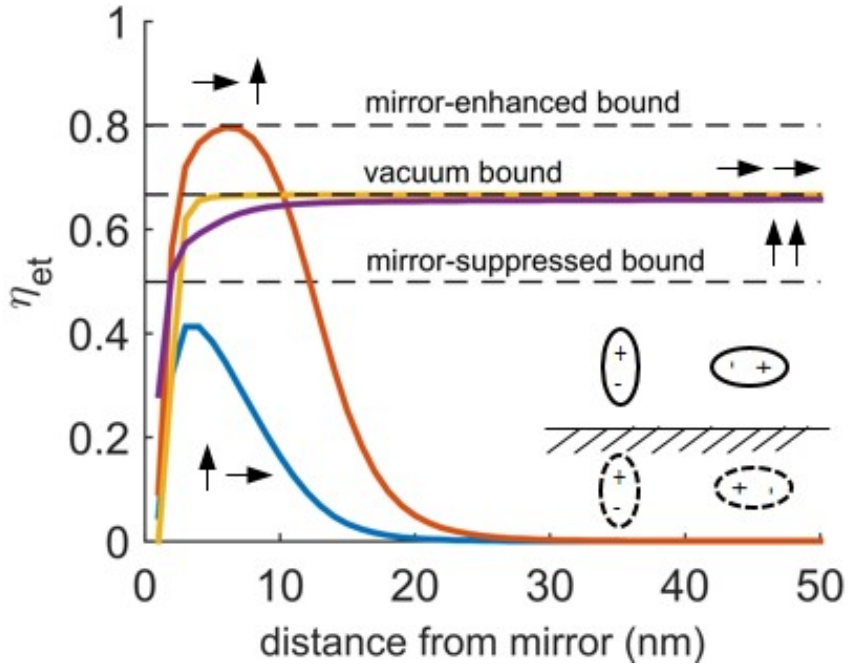

Fig. 6.4. Nanophotonic control of energy transfer between two atoms above a silver mirror. Here, we provide an example of how the environment can positively or negatively influence the energy transfer efficiency based primarily on the transition dipole moment orientation. We consider two atoms with spontaneous emission rates $\gamma_a = 2\gamma_d$ corresponding to a vacuum bound of $\eta_{max} = 2/3$. To overcome the vacuum bound, we propose using the orientation dipole moments of each atom relative to the mirror to control spontaneous emission rates. The ideal configuration corresponds to a donor parallel to a mirror and an acceptor perpendicular to a mirror, as it achieves the condition $\gamma_a \gg \gamma_d$ around 10 nm from the mirror. In this scenario, the environment modifies the fundamental bound of the energy transfer efficiency resulting in an overall enhancement. The opposite configuration (blue) will decrease the fundamental bound suppressing the overall energy transfer efficiency. Results are calculated with the full dyadic Green function for two atoms $r = 10$ nm apart.

6.7 Chapter Summary.

To conclude, we have derived a fundamental efficiency bound for resonance energy transfer between two atoms in the limit of large dipole-dipole coupling and in the absence of cooperative decay. We use the bound to derive design principles for controlling resonance energy transfer in nanophotonics and present an exactly solvable canonical example to illustrate the interplay of these effects. Our results will be critical in understanding the role of the environment in resonance energy transfer using nanophotonic and metamaterial approaches [45]. Future work will focus on developing a rigorous non-Markovian theory of energy transfer expanding the range of applicability to a wider range of electrodynamic engineered-reservoirs.

7. CONCLUSIONS AND OUTLOOK

For hyperbolic media, we have developed a foundation towards the study of hyperbolic many-body physics. Our work presents a unified framework to deriving a wide-range of seemingly disparate multi-atom processes for both ground-state and excited-state atoms. This approach avoids ad-hoc assumptions typically made through semi-classical treatments while also providing a clear identification of quantum-enhanced processes. Future work focusing on many-body physical phenomena in hyperbolic media will likely result in exciting discoveries with unique properties unlike those observed in cavity or waveguide QED.

An interesting idea to pursue, from the author's perspective, regards the study of light-induced self-organization in hyperbolic media. As we outlined in Chapter 3, the Super-Coulombic effect is only manifested in excited-state atoms. This implies this class of phenomena is only observable for atoms that are directly driven by light. Our theory predicts light-driven, freely-moving dopants/defects inside a hyperbolic medium would tend reorganize themselves in order to minimize their free energy. The self-organized structure should have long-range dipole-dipole correlations with potential superradiant emission properties when arranged along the hyperbolic resonance angle.

Regarding the second part of this thesis, the work requires further developments in both theory and experimental fronts. Theoretically, the definition for the energy transfer efficiency needs to be expanded to take into account the excitation of the donor. Furthermore, a careful comparison between theory and experiment should test the wide-ranging definitions of efficiency that exist within the literature. From an experimental perspective, it remains challenging to control the individual positions of atoms and molecules. Recent developments based on DNA scaffolding and STM-based positioning systems could potentially overcome these limitations. Finally, we

must emphasize that the quantum design principles we have proposed are basic rules of thumb which will require further refinement for an application-based photovoltaic design. Further work should focus on applying these principles for the design of the designer molecules for organic-based solar cells.

REFERENCES

REFERENCES

[1] P. W. Shor, "Algorithms for quantum computation: Discrete logarithms and factoring," in *Foundations of Computer Science, 1994 Proceedings., 35th Annual Symposium on*. Ieee, 1994, pp. 124–134.

[2] D. Beckman, A. N. Chari, S. Devabhaktuni, and J. Preskill, "Efficient networks for quantum factoring," *Physical Review A*, vol. 54, no. 2, p. 1034, 1996.

[3] L. M. Vandersypen, M. Steffen, G. Breyta, C. S. Yannoni, M. H. Sherwood, and I. L. Chuang, "Experimental realization of shor's quantum factoring algorithm using nuclear magnetic resonance," *Nature*, vol. 414, no. 6866, pp. 883–887, 2001.

[4] C.-Y. Lu, D. E. Browne, T. Yang, and J.-W. Pan, "Demonstration of a compiled version of shors quantum factoring algorithm using photonic qubits," *Physical Review Letters*, vol. 99, no. 25, p. 250504, 2007.

[5] B. Lanyon, T. Weinhold, N. K. Langford, M. Barbieri, D. James, A. Gilchrist, and A. White, "Experimental demonstration of a compiled version of shors algorithm with quantum entanglement," *Physical Review Letters*, vol. 99, no. 25, p. 250505, 2007.

[6] S. Lloyd, "Enhanced sensitivity of photodetection via quantum illumination," *Science*, vol. 321, no. 5895, pp. 1463–1465, 2008.

[7] G. Brida, I. P. Degiovanni, M. Genovese, E. D. Lopaeva, A. Meda, and I. R. Berchera, "Beyond classical limits by exploiting quantum light : a short review of inrim results," *Journal of Physics: Conference Series*, vol. 442, no. 1, p. 012022, 2013. [Online]. Available: `http://stacks.iop.org/1742-6596/442/i=1/a=012022`

[8] I. Bechera, A. Meda, I. Degiovanni, G. Brida, and M. Genovese, "Overcoming classical measurement limits through photon number correlations: an overview of a few recent results," in *SPIE Optical Engineering+ Applications*. International Society for Optics and Photonics, 2014, pp. 922 502–922 502.

[9] M. O. Scully, M. S. Zubairy, G. S. Agarwal, and H. Walther, "Extracting work from a single heat bath via vanishing quantum coherence," *Science*, vol. 299, no. 5608, pp. 862–864, 2003.

[10] K. E. Dorfman, D. V. Voronine, S. Mukamel, and M. O. Scully, "Photosynthetic reaction center as a quantum heat engine," *Proceedings of the National Academy of Sciences*, vol. 110, no. 8, pp. 2746–2751, 2013.

[11] J. Roßnagel, O. Abah, F. Schmidt-Kaler, K. Singer, and E. Lutz, "Nanoscale heat engine beyond the carnot limit," *Physical review letters*, vol. 112, no. 3, p. 030602, 2014.

[12] G. S. Engel, T. R. Calhoun, E. L. Read, T.-K. Ahn, T. Mančal, Y.-C. Cheng, R. E. Blankenship, and G. R. Fleming, "Evidence for wavelike energy transfer through quantum coherence in photosynthetic systems," *Nature*, vol. 446, no. 7137, pp. 782–786, 2007.

[13] E. Collini, C. Y. Wong, K. E. Wilk, P. M. Curmi, P. Brumer, and G. D. Scholes, "Coherently wired light-harvesting in photosynthetic marine algae at ambient temperature," *Nature*, vol. 463, no. 7281, p. 644, 2010.

[14] G. Panitchayangkoon, D. Hayes, K. A. Fransted, J. R. Caram, E. Harel, J. Wen, R. E. Blankenship, and G. S. Engel, "Long-lived quantum coherence in photosynthetic complexes at physiological temperature," *Proceedings of the National Academy of Sciences*, vol. 107, no. 29, pp. 12 766–12 770, 2010.

[15] H. Wallrabe and A. Periasamy, "Imaging protein molecules using fret and flim microscopy," *Current opinion in biotechnology*, vol. 16, no. 1, pp. 19–27, 2005.

[16] E. Romero, R. Augulis, V. I. Novoderezhkin, M. Ferretti, J. Thieme, D. Zigmantas, and R. Van Grondelle, "Quantum coherence in photosynthesis for efficient solar energy conversion," *Nature Physics*, vol. 10, no. 9, p. 676, 2014.

[17] J.-L. Brédas, E. H. Sargent, and G. D. Scholes, "Photovoltaic concepts inspired by coherence effects in photosynthetic systems," *Nature materials*, vol. 16, no. 1, pp. 35–44, 2017.

[18] D. Smith, P. Kolinko, and D. Schurig, "Negative refraction in indefinite media," *JOSA B*, vol. 21, no. 5, pp. 1032–1043, 2004.

[19] V. Podolskiy and E. Narimanov, "Strongly anisotropic waveguide as a nonmagnetic left-handed system," *Physical Review B*, vol. 71, no. 20, p. 201101, 2005.

[20] Z. Jacob, L. V. Alekseyev, and E. Narimanov, "Optical hyperlens: far-field imaging beyond the diffraction limit," *Optics express*, vol. 14, no. 18, pp. 8247–8256, 2006.

[21] D. Schurig, J. Mock, B. Justice, S. A. Cummer, J. B. Pendry, A. Starr, and D. Smith, "Metamaterial electromagnetic cloak at microwave frequencies," *Science*, vol. 314, no. 5801, pp. 977–980, 2006.

[22] S. Zhang, Y.-S. Park, J. Li, X. Lu, W. Zhang, and X. Zhang, "Negative refractive index in chiral metamaterials," *Physical review letters*, vol. 102, no. 2, p. 023901, 2009.

[23] S. Sun, Q. He, S. Xiao, Q. Xu, X. Li, and L. Zhou, "Gradient-index metasurfaces as a bridge linking propagating waves and surface waves," *Nature materials*, vol. 11, no. 5, pp. 426–431, 2012.

[24] N. Liu, M. Mesch, T. Weiss, M. Hentschel, and H. Giessen, "Infrared perfect absorber and its application as plasmonic sensor," *Nano letters*, vol. 10, no. 7, pp. 2342–2348, 2010.

[25] A. A. Govyadinov and V. A. Podolskiy, "Metamaterial photonic funnels for subdiffraction light compression and propagation," *Physical Review B*, vol. 73, no. 15, p. 155108, 2006.

[26] J. Yao, X. Yang, X. Yin, G. Bartal, and X. Zhang, "Three-dimensional nanometer-scale optical cavities of indefinite medium," *Proceedings of the National Academy of Sciences*, vol. 108, no. 28, pp. 11 327–11 331, 2011.

[27] Y. Guo, C. L. Cortes, S. Molesky, and Z. Jacob, "Broadband super-planckian thermal emission from hyperbolic metamaterials," *Applied Physics Letters*, vol. 101, no. 13, p. 131106, 2012.

[28] Z. Jacob, J.-Y. Kim, G. Naik, A. Boltasseva, E. Narimanov, and V. Shalaev, "Engineering photonic density of states using metamaterials," *Applied Physics B*, vol. 100, no. 1, pp. 215–218, 2010.

[29] W. E. Lamb and R. C. Retherford, "Fine structure of the hydrogen atom by a microwave method," *Phys. Rev.*, vol. 72, pp. 241–243, Aug 1947. [Online]. Available: `https://link.aps.org/doi/10.1103/PhysRev.72.241`

[30] H. A. Bethe, "The electromagnetic shift of energy levels," *Phys. Rev.*, vol. 72, pp. 339–341, Aug 1947. [Online]. Available: `https://link.aps.org/doi/10.1103/PhysRev.72.339`

[31] B. Odom, D. Hanneke, B. dUrso, and G. Gabrielse, "New measurement of the electron magnetic moment using a one-electron quantum cyclotron," *Physical Review Letters*, vol. 97, no. 3, p. 030801, 2006.

[32] G. Gabrielse, D. Hanneke, T. Kinoshita, M. Nio, and B. Odom, "New determination of the fine structure constant from the electron g value and qed," *Physical Review Letters*, vol. 97, no. 3, p. 030802, 2006.

[33] Anonymous, "Proceedings of the american physical society," *Phys. Rev.*, vol. 69, pp. 674–674, Jun 1946. [Online]. Available: `https://link.aps.org/doi/10.1103/PhysRev.69.674`

[34] C. Carniglia and L. Mandel, "Quantization of evanescent electromagnetic waves," *Physical Review D*, vol. 3, no. 2, p. 280, 1971.

[35] G. Agarwal, "Quantum electrodynamics in the presence of dielectrics and conductors. ii. theory of dispersion forces," *Physical Review A*, vol. 11, no. 1, p. 243, 1975.

[36] J. M. Wylie and J. Sipe, "Quantum electrodynamics near an interface," *Physical Review A*, vol. 30, no. 3, p. 1185, 1984.

[37] B. Huttner and S. M. Barnett, "Quantization of the electromagnetic field in dielectrics," *Physical Review A*, vol. 46, no. 7, p. 4306, 1992.

[38] R. Matloob, R. Loudon, S. M. Barnett, and J. Jeffers, "Electromagnetic field quantization in absorbing dielectrics," *Physical Review A*, vol. 52, no. 6, p. 4823, 1995.

[39] L. Knöll, S. Scheel, and D.-G. Welsch, "Qed in dispersing and absorbing media," *Coherence and Statistics of Photons and Atoms*, 2001.

[40] ——, "Qed in dispersing and absorbing media," Tech. Rep., 2000.

[41] S. Scheel and S. Y. Buhmann, "Macroscopic qed-concepts and applications," *arXiv preprint arXiv:0902.3586*, 2009.

[42] H. T. Dung, L. Knöll, and D.-G. Welsch, "Resonant dipole-dipole interaction in the presence of dispersing and absorbing surroundings," *Physical Review A*, vol. 66, no. 6, p. 063810, 2002.

[43] H. Safari and M. R. Karimpour, "Body-assisted van der waals interaction between excited atoms," *Physical review letters*, vol. 114, no. 1, p. 013201, 2015.

[44] H. Safari, S. Y. Buhmann, D.-G. Welsch, and H. T. Dung, "Body-assisted van der waals interaction between two atoms," *Physical Review A*, vol. 74, no. 4, p. 042101, 2006.

[45] C. L. Cortes and Z. Jacob, "Super-coulombic atom–atom interactions in hyperbolic media," *Nature communications*, vol. 8, p. 14144, 2017.

[46] I. Bloch, "Quantum coherence and entanglement with ultracold atoms in optical lattices," *Nature*, vol. 453, no. 7198, pp. 1016–1022, 2008.

[47] T. Wang, S. Yelin, R. Côté, E. Eyler, S. Farooqi, P. Gould, M. Koštrun, D. Tong, and D. Vrinceanu, "Superradiance in ultracold rydberg gases," *Physical Review A*, vol. 75, no. 3, p. 033802, 2007.

[48] R. A. de Oliveira, M. S. Mendes, W. S. Martins, P. L. Saldanha, J. W. Tabosa, and D. Felinto, "Single-photon superradiance in cold atoms," *Physical Review A*, vol. 90, no. 2, p. 023848, 2014.

[49] C. Hettich, C. Schmitt, J. Zitzmann, S. Kühn, I. Gerhardt, and V. Sandoghdar, "Nanometer resolution and coherent optical dipole coupling of two individual molecules," *Science*, vol. 298, no. 5592, pp. 385–389, 2002.

[50] A. Goban, C.-L. Hung, J. D. Hood, S.-P. Yu, J. A. Muniz, O. Painter, and H. J. Kimble, "Superradiance for atoms trapped along a photonic crystal waveguide," *Phys. Rev. Lett.*, vol. 115, p. 063601, Aug 2015.

[51] A. González-Tudela, C.-L. Hung, D. Chang, J. Cirac, and H. Kimble, "Subwavelength vacuum lattices and atom–atom interactions in two-dimensional photonic crystals," *Nature Photonics*, vol. 9, no. 5, pp. 320–325, 2015.

[52] S. Ravets, H. Labuhn, D. Barredo, L. Béguin, T. Lahaye, and A. Browaeys, "Coherent dipole-dipole coupling between two single rydberg atoms at an electrically-tuned forster resonance," *Nature Physics*, vol. 10, no. 12, pp. 914–917, 2014.

[53] M. Saffman, T. Walker, and K. Mølmer, "Quantum information with rydberg atoms," *Reviews of Modern Physics*, vol. 82, no. 3, p. 2313, 2010.

[54] M. H. Devoret, A. Wallraff, and J. Martinis, "Superconducting qubits: A short review," *Preprint at http://arxiv.org/abs/cond-mat/0411174*, 2004.

[55] R. Fleury and A. Alù, "Enhanced superradiance in epsilon-near-zero plasmonic channels," *Physical Review B*, vol. 87, no. 20, p. 201101, 2013.

[56] R. Maas, J. Parsons, N. Engheta, and A. Polman, "Experimental realization of an epsilon-near-zero metamaterial at visible wavelengths," *Nature Photonics*, vol. 7, no. 11, pp. 907–912, 2013.

[57] D. Martín-Cano, L. Martín-Moreno, F. J. Garcia-Vidal, and E. Moreno, "Resonance energy transfer and superradiance mediated by plasmonic nanowaveguides," *Nano letters*, vol. 10, no. 8, pp. 3129–3134, 2010.

[58] S.-A. Biehs and G. S. Agarwal, "Large enhancement of förster resonance energy transfer on graphene platforms," *Applied Physics Letters*, vol. 103, no. 24, p. 243112, 2013.

[59] A. Imamog, D. D. Awschalom, G. Burkard, D. P. DiVincenzo, D. Loss, M. Sherwin, A. Small *et al.*, "Quantum information processing using quantum dot spins and cavity qed," *Physical Review Letters*, vol. 83, no. 20, p. 4204, 1999.

[60] J. Ye, D. Vernooy, and H. Kimble, "Trapping of single atoms in cavity qed," *Physical Review Letters*, vol. 83, no. 24, p. 4987, 1999.

[61] H. Zheng, D. J. Gauthier, and H. U. Baranger, "Waveguide qed: Many-body bound-state effects in coherent and fock-state scattering from a two-level system," *Physical Review A*, vol. 82, no. 6, p. 063816, 2010.

[62] A. F. Van Loo, A. Fedorov, K. Lalumière, B. C. Sanders, A. Blais, and A. Wallraff, "Photon-mediated interactions between distant artificial atoms," *Science*, vol. 342, no. 6165, pp. 1494–1496, 2013.

[63] D. E. Chang, A. S. Sørensen, E. A. Demler, and M. D. Lukin, "A single-photon transistor using nanoscale surface plasmons," *Nature Physics*, vol. 3, no. 11, pp. 807–812, 2007.

[64] T. Baba, "Slow light in photonic crystals," *Nature photonics*, vol. 2, no. 8, pp. 465–473, 2008.

[65] D. Martín-Cano, A. González-Tudela, L. Martín-Moreno, F. J. García-Vidal, C. Tejedor, and E. Moreno, "Dissipation-driven generation of two-qubit entanglement mediated by plasmonic waveguides," *Phys. Rev. B*, vol. 84, p. 235306, Dec 2011.

[66] R. Sokhoyan and H. A. Atwater, "Quantum optical properties of a dipole emitter coupled to an -near-zero nanoscale waveguide," *Optics express*, vol. 21, no. 26, pp. 32 279–32 290, 2013.

[67] G. W. Milton, R. C. McPhedran, and A. Sihvola, "The searchlight effect in hyperbolic materials," *Optics express*, vol. 21, no. 12, pp. 14 926–14 942, 2013.

[68] A. Poddubny, I. Iorsh, P. Belov, and Y. Kivshar, "Hyperbolic metamaterials," *Nature Photonics*, vol. 7, no. 12, pp. 948–957, 2013.

[69] C. Cortes, W. Newman, S. Molesky, and Z. Jacob, "Quantum nanophotonics using hyperbolic metamaterials," *Journal of Optics*, vol. 14, no. 6, p. 063001, 2012.

[70] H. N. Krishnamoorthy, Z. Jacob, E. Narimanov, I. Kretzschmar, and V. M. Menon, "Topological transitions in metamaterials," *Science*, vol. 336, no. 6078, pp. 205–209, 2012.

[71] J. D. Caldwell, A. V. Kretinin, Y. Chen, V. Giannini, M. M. Fogler, Y. Francescato, C. T. Ellis, J. G. Tischler, C. R. Woods, A. J. Giles *et al.*, "Sub-diffractional volume-confined polaritons in the natural hyperbolic material hexagonal boron nitride," *Nature Communications*, vol. 5, p. 5221, 2014.

[72] S. Dai, Q. Ma, M. K. Liu, T. Andersen, Z. Fei, M. D. Goldflam, M. Wagner, K. Watanabe, T. Taniguchi, M. Thiemens, F. Keilmann, G. C. a. M. Janssen, S.-E. Zhu, P. Jarillo-Herrero, M. M. Fogler, and D. N. Basov, "Graphene on hexagonal boron nitride as a tunable hyperbolic metamaterial," *Nature Nanotechnology*, vol. 10, no. 8, pp. 682–686, Aug. 2015.

[73] T. T. Tran, K. Bray, M. J. Ford, M. Toth, and I. Aharonovich, "Quantum emission from hexagonal boron nitride monolayers," *Nature Nanotechnology*, vol. 11, no. 1, pp. 37–41, Jan. 2016.

[74] D. Wong, J. Velasco Jr, L. Ju, J. Lee, S. Kahn, H.-Z. Tsai, C. Germany, T. Taniguchi, K. Watanabe, A. Zettl *et al.*, "Characterization and manipulation of individual defects in insulating hexagonal boron nitride using scanning tunnelling microscopy," *Nature nanotechnology*, vol. 10, no. 11, pp. 949–953, 2015.

[75] T. U. Tumkur, J. K. Kitur, C. E. Bonner, A. N. Poddubny, E. E. Narimanov, and M. A. Noginov, "Control of förster energy transfer in the vicinity of metallic surfaces and hyperbolic metamaterials," *Faraday discussions*, vol. 178, pp. 395–412, 2015.

[76] A. N. Poddubny, "Collective förster energy transfer modified by a planar metallic mirror," *Physical Review B*, vol. 92, no. 15, p. 155418, 2015.

[77] A. S. Potemkin, A. N. Poddubny, P. A. Belov, and Y. S. Kivshar, "Green function for hyperbolic media," *Physical Review A*, vol. 86, no. 2, p. 023848, 2012.

[78] Z. Jacob and E. E. Narimanov, "Optical hyperspace for plasmons: Dyakonov states in metamaterials," *Applied Physics Letters*, vol. 93, no. 22, p. 221109, 2008.

[79] A. A. High, R. C. Devlin, A. Dibos, M. Polking, D. S. Wild, J. Perczel, N. P. de Leon, M. D. Lukin, and H. Park, "Visible-frequency hyperbolic metasurface," *Nature*, vol. 522, no. 7555, pp. 192–196, 2015.

[80] J. S. Gomez-Diaz, M. Tymchenko, and A. Alù, "Hyperbolic plasmons and topological transitions over uniaxial metasurfaces," *Physical review letters*, vol. 114, no. 23, p. 233901, 2015.

[81] S. Gangaraj, T. Low, A. Nemilentsau, and G. W. Hanson, "Black phosphorus and two-dimensional hyperbolic materials: tunable surface plasmons, green function and complex-plane analysis," *Preprint at http://arxiv.org/abs/1509.01544*, 2015.

[82] W. D. Newman, C. L. Cortes, A. Afshar, A. Meldrum, K. Cadien, R. Fedosejevs, and Z. Jacob, "Super-coulombic dipole-dipole interactions in hyperbolic media," in *Conference on Lasers and Electro-Optics*. Optical Society of America, 2016, p. FTh4D.1.

[83] W. Yan, M. Wubs, and N. A. Mortensen, "Hyperbolic metamaterials: Nonlocal response regularizes broadband supersingularity," *Physical Review B*, vol. 86, no. 20, p. 205429, 2012.

[84] D. Correas-Serrano, J. Gomez-Diaz, M. Tymchenko, and A. Alù, "Nonlocal response of hyperbolic metasurfaces," *Optics express*, vol. 23, no. 23, pp. 29 434–29 448, 2015.

[85] P. K. Jha, M. Mrejen, J. Kim, C. Wu, Y. Wang, Y. V. Rostovtsev, and X. Zhang, "Coherence-driven topological transition in quantum metamaterials," *Physical review letters*, vol. 116, no. 16, p. 165502, 2016.

[86] H. T. Dung, L. Knöll, and D.-G. Welsch, "Intermolecular energy transfer in the presence of dispersing and absorbing media," *Physical Review A*, vol. 65, no. 4, p. 043813, 2002.

[87] S. Bidault, A. Devilez, P. Ghenuche, B. Stout, N. Bonod, and J. Wenger, "Competition between forster resonance energy transfer and donor photodynamics in plasmonic dimer nanoantennas," *ACS photonics*, vol. 3, no. 5, pp. 895–903, 2016.

[88] C. Blum, N. Zijlstra, A. Lagendijk, M. Wubs, A. P. Mosk, V. Subramaniam, and W. L. Vos, "Nanophotonic control of the förster resonance energy transfer efficiency," *Physical review letters*, vol. 109, no. 20, p. 203601, 2012.

[89] R. Chance, A. Prock, and R. Silbey, "Molecular fluorescence and energy transfer near interfaces," *Advances in Chemical Physics*, vol. 37, pp. 1–65, 1978. [Online]. Available: `http://onlinelibrary.wiley.com/doi/10.1002/9780470142561.ch1/summary`

[90] G. Ford and W. Weber, "Electromagnetic interactions of molecules with metal surfaces," *Physics Reports*, vol. 113, no. 4, pp. 195–287, 1984. [Online]. Available: `http://totuvach.free.fr/Articles/fordweber.pdf`

[91] L. Klushin and O. Tcherkasskaya, "Effects of molecular distribution on the fluorescence transfer: Exact results for slab geometry," *The Journal of chemical physics*, vol. 119, no. 6, pp. 3421–3428, 2003.

[92] J. R. Lakowicz, *Principles of Fluorescence Spectroscopy*, 2nd ed. New York: Springer, 2004.

[93] M. Scheibner, T. Schmidt, L. Worschech, A. Forchel, G. Bacher, T. Passow, and D. Hommel, "Superradiance of quantum dots," *Nature Physics*, vol. 3, no. 2, pp. 106–110, 2007.

[94] C. Van Ditzhuijzen, A. Koenderink, J. Hernández, F. Robicheaux, L. Noordam, and H. v. L. Van Den Heuvell, "Spatially resolved observation of dipole-dipole interaction between rydberg atoms," *Physical Review Letters*, vol. 100, no. 24, p. 243201, 2008.

[95] Z. Ficek and R. Tanaś, "Delayed sudden birth of entanglement," *Physical Review A*, vol. 77, no. 5, p. 054301, 2008.

[96] P. C. Ray, Z. Fan, R. A. Crouch, S. S. Sinha, and A. Pramanik, "Nanoscopic optical rulers beyond the fret distance limit: fundamentals and applications," *Chemical Society Reviews*, vol. 43, no. 17, pp. 6370–6404, 2014.

[97] L. Novotny and B. Hecht, *Principles of nano-optics*. Cambridge Univ Pr, 2006.

[98] M. Hopmeier, W. Guss, M. Deussen, E. O. Gbel, and R. F. Mahrt, "Enhanced dipole-dipole interaction in a polymer microcavity," *Physical review letters*, vol. 82, no. 20, p. 4118, 1999. [Online]. Available: http://journals.aps.org/prl/abstract/10.1103/PhysRevLett.82.4118

[99] P. Andrew and W. L. Barnes, "Frster energy transfer in an optical microcavity," *Science*, vol. 290, no. 5492, pp. 785–788, 2000. [Online]. Available: http://www.sciencemag.org/content/290/5492/785.short

[100] C. E. Finlayson, D. S. Ginger, and N. C. Greenham, "Enhanced Frster energy transfer in organic/inorganic bilayer optical microcavities," *Chemical physics letters*, vol. 338, no. 2, pp. 83–87, 2001. [Online]. Available: http://www.sciencedirect.com/science/article/pii/S0009261401002470

[101] J. R. Lakowicz, Y. Shen, S. D'Auria, J. Malicka, J. Fang, Z. Gryczynski, and I. Gryczynski, "Radiative decay engineering. 2. Effects of Silver Island films on fluorescence intensity, lifetimes, and resonance energy transfer," *Analytical Biochemistry*, vol. 301, no. 2, pp. 261–277, Feb. 2002.

[102] H. Fujiwara, K. Sasaki, and H. Masuhara, "Enhancement of Frster energy transfer within a microspherical cavity," *ChemPhysChem*, vol. 6, no. 11, pp. 2410–2416, 2005. [Online]. Available: http://onlinelibrary.wiley.com/doi/10.1002/cphc.200500318/full

[103] J. Zhang, Y. Fu, and J. Lakowicz, "Enhanced frster resonance energy transfer (FRET) on a single metal particle," *Journal of Physical Chemistry C*, vol. 111, no. 1, pp. 50–56, Jan. 2007. [Online]. Available: http://www-ncbi-nlm-nih-gov.login.ezproxy.library.ualberta.ca/pmc/articles/PM

[104] V. K. Komarala, A. L. Bradley, Y. P. Rakovich, S. J. Byrne, Y. K. Gunko, and A. L. Rogach, "Surface plasmon enhanced Frster resonance energy transfer between the CdTe quantum dots," *Applied Physics Letters*, vol. 93, no. 12, p. 123102, Sep. 2008. [Online]. Available: http://scitation.aip.org/content/aip/journal/apl/93/12/10.1063/1.2981209

[105] M. L. Viger, D. Brouard, and D. Boudreau, "Plasmon-Enhanced Resonance Energy Transfer from a Conjugated Polymer to Fluorescent Multilayer Core-Shell Nanoparticles: A Photophysical Study," *The Journal of Physical Chemistry C*, vol. 115, no. 7, pp. 2974–2981, 2011. [Online]. Available: http://pubs.acs.org/doi/abs/10.1021/jp109993a

[106] P. Ghenuche, J. de Torres, S. B. Moparthi, V. Grigoriev, and J. Wenger, "Nanophotonic Enhancement of the Frster Resonance Energy-Transfer Rate with Single Nanoapertures," *Nano letters*, vol. 14, no. 8, pp. 4707–4714, 2014. [Online]. Available: http://pubs.acs.org/doi/abs/10.1021/nl5018145

[107] D. Lu, S. K. Cho, S. Ahn, L. Brun, C. J. Summers, and W. Park, "Plasmon Enhancement Mechanism for the Upconversion Processes in NaYF4: Yb3+, Er3+ Nanoparticles: Maxwell versus Frster," *ACS nano*, vol. 8, no. 8, pp. 7780–7792, 2014. [Online]. Available: http://pubs.acs.org/doi/abs/10.1021/nn5011254

[108] F. Reil, U. Hohenester, J. R. Krenn, and A. Leitner, "Frster-Type Resonant Energy Transfer Influenced by Metal Nanoparticles," *Nano Letters*, vol. 8, no. 12, pp. 4128–4133, Dec. 2008. [Online]. Available: http://dx.doi.org/10.1021/nl801480m

[109] L. Zhao, T. Ming, L. Shao, H. Chen, and J. Wang, "Plasmon-controlled frster resonance energy transfer," *The Journal of Physical Chemistry C*, vol. 116, no. 14, pp. 8287–8296, Apr. 2012. [Online]. Available: http://dx.doi.org/10.1021/jp300916a

[110] C. A. Marocico, X. Zhang, and A. L. Bradley, "Spectral overlap dependence of enhanced energy transfer near small Au nanoparticles," in *Transparent Optical Networks (ICTON), 2014 16th International Conference on*. IEEE, 2014, pp. 1–4. [Online]. Available: http://ieeexplore.ieee.org/xpls/abs$_a ll.jsp?arnumber = 6876459$

[111] A. Leitner and H. Reinisch, "Reduced intermolecular energy transfer on silver island films," *Chemical Physics Letters*, vol. 146, no. 34, pp. 320–324, May 1988. [Online]. Available: http://www.sciencedirect.com/science/article/pii/0009261488874529

[112] K.-S. Kim, J.-H. Kim, H. Kim, F. Laquai, E. Arifin, J.-K. Lee, S. I. Yoo, and B.-H. Sohn, "Switching off FRET in the hybrid assemblies of diblock copolymer micelles, quantum dots, and dyes by plasmonic nanoparticles," *ACS nano*, vol. 6, no. 6, pp. 5051–5059, 2012. [Online]. Available: http://pubs.acs.org/doi/abs/10.1021/nn301893e

[113] T. U. Tumkur, J. K. Kitur, C. E. Bonner, A. N. Poddubny, E. E. Narimanov, and M. A. Noginov, "Control of forster energy transfer in the vicinity of metallic surfaces and hyperbolic metamaterials," *Faraday Discuss.*, pp. –, 2015. [Online]. Available: http://dx.doi.org/10.1039/C4FD00184B

[114] M. J. A. de Dood, J. Knoester, A. Tip, and A. Polman, "Frster transfer and the local optical density of states in erbium-doped silica," *Physical Review B*, vol. 71, no. 11, p. 115102, Mar. 2005. [Online]. Available: http://link.aps.org/doi/10.1103/PhysRevB.71.115102

[115] C. Blum, N. Zijlstra, A. Lagendijk, M. Wubs, A. P. Mosk, V. Subramaniam, and W. L. Vos, "Nanophotonic control of the frster resonance energy transfer efficiency," *Physical Review Letters*, vol. 109, no. 20, p. 203601, Nov. 2012.

[116] F. T. Rabouw, S. A. den Hartog, T. Senden, and A. Meijerink, "Photonic effects on the Frster resonance energy transfer efficiency," *Nature Communications*, vol. 5, Apr. 2014. [Online]. Available: http://www.nature.com/ncomms/2014/140402/ncomms4610/full/ncomms4610.html

[117] F. Schleifenbaum, A. M. Kern, A. Konrad, and A. J. Meixner, "Dynamic control of Frster energy transfer in a photonic environment," *Physical Chemistry Chemical Physics*, vol. 16, no. 25, p. 12812, 2014. [Online]. Available: http://xlink.rsc.org/?DOI=c4cp01306a

[118] R. R. Chance, A. Prock, and R. Silbey, "Comments on the classical theory of energy transfer," *The Journal of Chemical Physics*, vol. 62, no. 6, pp. 2245–2253, 1975. [Online]. Available: http://scitation.aip.org/content/aip/journal/jcp/62/6/10.1063/1.430748

[119] V. Agranovich and M. Galanin, "Electron-excitation energy transfer in condensed media," *Moscow Izdatel Nauka*, vol. 1, 1978.

[120] X. M. Hua, J. I. Gersten, and A. Nitzan, "Theory of energy transfer between molecules near solid state particles," *The Journal of Chemical Physics*, vol. 83, no. 7, p. 3650, 1985. [Online]. Available: http://jcp.aip.org/resource/1/jcpsa6/v83/i7/p3650$_s$1?$coden = JCPSA6volume = 83issue = 7page = 3650seqno = 1view = citings$

[121] G. Kurizki and A. Z. Genack, "Suppression of molecular interactions in periodic dielectric structures," *Physical review letters*, vol. 61, no. 19, p. 2269, 1988. [Online]. Available: http://journals.aps.org/prl/abstract/10.1103/PhysRevLett.61.2269

[122] S. John and J. Wang, "Quantum optics of localized light in a photonic band gap," *Physical Review B*, vol. 43, no. 16, pp. 12 772–12 789, Jun. 1991. [Online]. Available: http://link.aps.org/doi/10.1103/PhysRevB.43.12772

[123] T. Kobayashi, Q. Zheng, and T. Sekiguchi, "Resonant dipole-dipole interaction in a cavity," *Physical Review A*, vol. 52, no. 4, p. 2835, 1995. [Online]. Available: http://journals.aps.org/pra/abstract/10.1103/PhysRevA.52.2835

[124] S. Bay, P. Lambropoulos, and K. Mlmer, "Atom-atom interaction in strongly modified reservoirs," *Physical Review A*, vol. 55, no. 2, pp. 1485–1496, Feb. 1997. [Online]. Available: http://link.aps.org/doi/10.1103/PhysRevA.55.1485

[125] G. S. Agarwal and S. D. Gupta, "Microcavity-induced modification of the dipole-dipole interaction," *Physical Review A*, vol. 57, no. 1, pp. 667–670, Jan. 1998. [Online]. Available: http://link.aps.org/doi/10.1103/PhysRevA.57.667

[126] V. V. Klimov and V. S. Letokhov, "Resonance interaction between two atomic dipoles separated by the surface of a dielectric nanosphere," *Physical Review A*, vol. 58, no. 4, p. 3235, 1998. [Online]. Available: http://journals.aps.org/pra/abstract/10.1103/PhysRevA.58.3235

[127] D. L. Andrews and A. A. Demidov, *Resonance energy transfer*. Wiley New York, 1999.

[128] D. M. Basko, F. Bassani, G. C. La Rocca, and V. M. Agranovich, "Electronic energy transfer in a microcavity," *Physical Review B*, vol. 62, no. 23, p. 15962, 2000. [Online]. Available: http://journals.aps.org/prb/abstract/10.1103/PhysRevB.62.15962

[129] H. T. Dung, L. Knoll, and D.-G. Welsch, "Intermolecular energy transfer in the presence of dispersing and absorbing media," *Physical Review A*, vol. 65, no. 4, p. 043813, Apr. 2002. [Online]. Available: http://link.aps.org/doi/10.1103/PhysRevA.65.043813

[130] G. C. des Francs, C. Girard, and O. J. Martin, "Fluorescence resonant energy transfer in the optical near field," *Physical Review A*, vol. 67, no. 5, p. 053805, 2003. [Online]. Available: http://journals.aps.org/pra/abstract/10.1103/PhysRevA.67.053805

[131] A. O. Govorov, J. Lee, and N. A. Kotov, "Theory of plasmon-enhanced frster energy transfer in optically excited semiconductor and metal nanoparticles," *Physical Review B*, vol. 76, no. 12, p. 125308, Sep. 2007. [Online]. Available: http://link.aps.org/doi/10.1103/PhysRevB.76.125308

[132] M. Durach, A. Rusina, V. I. Klimov, and M. I. Stockman, "Nanoplasmonic renormalization and enhancement of Coulomb interactions," *New Journal of Physics*, vol. 10, no. 10, p. 105011, Oct. 2008. [Online]. Available: http://iopscience.iop.org/1367-2630/10/10/105011

[133] U. Hohenester and A. Trugler, "Interaction of Single Molecules With Metallic Nanoparticles," *IEEE Journal of Selected Topics in Quantum Electronics*, vol. 14, no. 6, pp. 1430–1440, Nov. 2008.

[134] V. N. Pustovit and T. V. Shahbazyan, "Resonance energy transfer near metal nanostructures mediated by surface plasmons," *Physical Review B*, vol. 83, no. 8, p. 085427, Feb. 2011. [Online]. Available: http://link.aps.org/doi/10.1103/PhysRevB.83.085427

[135] L. Novotny and B. Hecht, *Principles of nano-optics*. Cambridge university press, 2012.

[136] G. Ford and W. Weber, "Electromagnetic interactions of molecules with metal surfaces," *Physics Reports*, vol. 113, no. 4, pp. 195–287, 1984.

[137] R. Chance, A. Prock, and R. Silbey, "Molecular fluorescence and energy transfer near interfaces," *Advances in Chemical Physics*, vol. 37, pp. 1–65, 1978.

[138] *See supplementary info for more details.*

[139] J. Zhang, Y. Fu, M. H. Chowdhury, and J. R. Lakowicz, "Enhanced Frster resonance energy transfer on single metal particle. 2. dependence on donor-acceptor separation distance, particle size, and distance from metal surface," *The Journal of Physical Chemistry C*, vol. 111, no. 32, pp. 11 784–11 792, 2007. [Online]. Available: http://pubs.acs.org/doi/abs/10.1021/jp067887r

[140] M. Lunz, V. A. Gerard, Y. K. Gunko, V. Lesnyak, N. Gaponik, A. S. Susha, A. L. Rogach, and A. L. Bradley, "Surface plasmon enhanced energy transfer between donor and acceptor CdTe nanocrystal quantum dot monolayers," *Nano Letters*, vol. 11, no. 8, pp. 3341–3345, Aug. 2011. [Online]. Available: http://dx.doi.org/10.1021/nl201714y

[141] L.-W. Li, P.-S. Kooi, M.-S. Leong, and T.-S. Yee, "Electromagnetic dyadic green's function in spherically multilayered media," *Microwave Theory and Techniques, IEEE Transactions on*, vol. 42, no. 12, pp. 2302–2310, 1994.

[142] H. Lee, Y.-C. Cheng, and G. R. Fleming, "Coherence dynamics in photosynthesis: protein protection of excitonic coherence," *Science*, vol. 316, no. 5830, pp. 1462–1465, 2007.

[143] A. Chenu and G. D. Scholes, "Coherence in energy transfer and photosynthesis," *Annual review of physical chemistry*, vol. 66, pp. 69–96, 2015.

[144] M. Yang and G. R. Fleming, "Influence of phonons on exciton transfer dynamics: comparison of the Redfield, Frster, and modified Redfield equations," *Chemical physics*, vol. 275, no. 1, pp. 355–372, 2002. [Online]. Available: http://www.sciencedirect.com/science/article/pii/S0301010401005407

[145] A. Ishizaki and G. R. Fleming, "Unified treatment of quantum coherent and incoherent hopping dynamics in electronic energy transfer: Reduced hierarchy equation approach," *The Journal of chemical physics*, vol. 130, no. 23, p. 234111, 2009.

[146] C. Wang, J. Ren, and J. Cao, "Nonequilibrium energy transfer at nanoscale: A unified theory from weak to strong coupling," *Scientific reports*, vol. 5, 2015.

[147] D. Beljonne, C. Curutchet, G. D. Scholes, and R. J. Silbey, "Beyond forster resonance energy transfer in biological and nanoscale systems," *The journal of physical chemistry B*, vol. 113, no. 19, pp. 6583–6599, 2009.

[148] Y. Tanimura, "Reduced hierarchical equations of motion in real and imaginary time: Correlated initial states and thermodynamic quantities," *The Journal of chemical physics*, vol. 141, no. 4, p. 044114, 2014.

[149] E. N. Zimanyi and R. J. Silbey, "Theoretical description of quantum effects in multi-chromophoric aggregates," *Phil. Trans. R. Soc. A*, vol. 370, no. 1972, pp. 3620–3637, 2012.

[150] D. P. McCutcheon and A. Nazir, "Consistent treatment of coherent and incoherent energy transfer dynamics using a variational master equation," *The Journal of chemical physics*, vol. 135, no. 11, p. 114501, 2011.

[151] I. Kassal, J. Yuen-Zhou, and S. Rahimi-Keshari, "Does coherence enhance transport in photosynthesis?" *The journal of physical chemistry letters*, vol. 4, no. 3, pp. 362–367, 2013.

[152] I. Kassal and A. Aspuru-Guzik, "Environment-assisted quantum transport in ordered systems," *New Journal of Physics*, vol. 14, no. 5, p. 053041, 2012.

[153] M. Mohseni, A. Shabani, S. Lloyd, and H. Rabitz, "Energy-scales convergence for optimal and robust quantum transport in photosynthetic complexes," *The Journal of chemical physics*, vol. 140, no. 3, p. 01B609_1, 2014.

[154] P. Rebentrost, M. Mohseni, I. Kassal, S. Lloyd, and A. Aspuru-Guzik, "Environment-assisted quantum transport," *New Journal of Physics*, vol. 11, no. 3, p. 033003, 2009.

[155] A. Chin, J. Prior, R. Rosenbach, F. Caycedo-Soler, S. Huelga, and M. Plenio, "The role of non-equilibrium vibrational structures in electronic coherence and recoherence in pigment-protein complexes," *Nature Physics*, vol. 9, no. 2, p. 113, 2013.

[156] R. Croce and H. Van Amerongen, "Natural strategies for photosynthetic light harvesting," *Nature chemical biology*, vol. 10, no. 7, pp. 492–501, 2014.

[157] H.-G. Duan, V. I. Prokhorenko, R. J. Cogdell, K. Ashraf, A. L. Stevens, M. Thorwart, and R. D. Miller, "Nature does not rely on long-lived electronic quantum coherence for photosynthetic energy transfer," *Proceedings of the National Academy of Sciences*, vol. 114, no. 32, pp. 8493–8498, 2017.

[158] D. M. Wilkins and N. S. Dattani, "Why quantum coherence is not important in the fenna–matthews–olsen complex," *Journal of chemical theory and computation*, vol. 11, no. 7, pp. 3411–3419, 2015.

[159] S. D. Druger, S. Arnold, and L. M. Folan, "Theory of enhanced energy transfer between molecules embedded in spherical dielectric particles," *The Journal of Chemical Physics*, vol. 87, no. 5, pp. 2649–2659, Sep. 1987. [Online]. Available: http://scitation.aip.org/content/aip/journal/jcp/87/5/10.1063/1.453103

[160] A. Olaya-Castro, C. F. Lee, F. F. Olsen, and N. F. Johnson, "Efficiency of energy transfer in a light-harvesting system under quantum coherence," *Physical Review B*, vol. 78, no. 8, p. 085115, 2008.

[161] M. Mohseni, P. Rebentrost, S. Lloyd, and A. Aspuru-Guzik, "Environment-assisted quantum walks in photosynthetic energy transfer," *The Journal of chemical physics*, vol. 129, no. 17, p. 11B603, 2008.

[162] W. K. Wootters, "Entanglement of formation of an arbitrary state of two qubits," *Physical Review Letters*, vol. 80, no. 10, p. 2245, 1998.

[163] H. C. Chen, *Theory of electromagnetic waves: a coordinate-free approach*. McGraw-Hill Book Company, 1983.

[164] A. Gonzalez-Tudela, D. Martin-Cano, E. Moreno, L. Martin-Moreno, C. Tejedor, and F. J. Garcia-Vidal, "Entanglement of two qubits mediated by one-dimensional plasmonic waveguides," *Physical review letters*, vol. 106, no. 2, p. 020501, 2011.

APPENDICES

A. APPENDIX: DYADIC GREEN FUNCTION ABOVE A UNIAXIAL MEDIUM

In this appendix, we derive the scattering coefficients and dyadic Green functions required for the problem of two atoms interacting atoms above a uniaxial half-space. We consider both homogeneous and scattering contributions, providing simplified results in all cases.

A.1 Scattering coefficients of a general uniaxial half-space

In this section, we will develop a formalism that determines the reflection and transmission coefficients between an isotropic medium and a general uniaxial medium with arbitrary optic axis $\mathbf{c}$. The incident, reflected and transmitted electric field vectors will then take the form

$$\mathbf{E}_i = (A_1\mathbf{s} + A_2\mathbf{p}_\pm) \tag{A.1}$$

$$\mathbf{E}_r = (B_1\mathbf{s} + B_2\mathbf{p}_\mp) \tag{A.2}$$

$$\mathbf{E}_t = (C_1\mathbf{e}_o + C_2\mathbf{e}_e) \tag{A.3}$$

where $\mathbf{s} = \mathbf{k} \times \mathbf{n}$ is vector that lies perpendicular to the plane of incidence, and $\mathbf{p}_\pm = \mathbf{k}_\pm \times \mathbf{s}$ lies perpendicular to $\mathbf{k}$ and $\mathbf{s}$. Inside the uniaxial medium, general wave propagation is decomposed in terms of an ordinary wavevector $\mathbf{e}_o$ and extraordinary wavevector contribution $\mathbf{e}_e$. Using $\mathbf{k}\times\mathbf{E}_k = \omega\mu_o\mathbf{H}_k$, the magnetic field intensity takes the form

$$\mathbf{H}_i = k_1(A_1\mathbf{p}_\pm - A_2\mathbf{s}) \tag{A.4}$$

$$\mathbf{H}_r = k_1(B_1\mathbf{p}_\mp - B_2\mathbf{s}) \tag{A.5}$$

$$\mathbf{H}_t = (C_1(\mathbf{k}_{to} \times \mathbf{e}_o) + C_2(\mathbf{k}_{te} \times \mathbf{e}_e)) \tag{A.6}$$

Applying these equations to the boundary conditions, we get

$$[A_1\mathbf{s} + A_2\mathbf{p}_\pm + B_1\mathbf{s} + B_2\mathbf{p}_\mp - C_1\mathbf{e}_o - C_2\mathbf{e}_e] \times \mathbf{n} = 0 \quad \text{(A.7)}$$

$$[A_1k_1\mathbf{p}_\pm - A_2k_1\mathbf{s} + B_1k_1\mathbf{p}_\mp - B_2k_1\mathbf{s} - C_1(\mathbf{k}_{to} \times \mathbf{e}_o) - C_2(\mathbf{k}_{te} \times \mathbf{e}_e)] \times \mathbf{n} = 0 \quad \text{(A.8)}$$

which are vector equations. To convert to a scalar equation, we must take the dot product with some arbitrary vector $\mathbf{m}$. What is the correct choice of $\mathbf{m}$? In the kDB basis, there are only three independent choices: $\mathbf{k}, \mathbf{s}$, and $\mathbf{p}$. If we apply all three, we see that only $\mathbf{k}$ and $\mathbf{s}$ give non-zero solutions. We thus obtain the set of four independent equations:

$$\mathbf{k} \cdot [A_1\mathbf{s} + A_2\mathbf{p}_+ + B_1\mathbf{s} + B_2\mathbf{p}_- - C_1\mathbf{e}_o - C_2\mathbf{e}_e] \times \mathbf{n} = 0 \quad \text{(A.9)}$$

$$\mathbf{s} \cdot [A_1\mathbf{s} + A_2\mathbf{p}_+ + B_1\mathbf{s} + B_2\mathbf{p}_- - C_1\mathbf{e}_o - C_2\mathbf{e}_e] \times \mathbf{n} = 0 \quad \text{(A.10)}$$

$$\mathbf{k} \cdot [A_1k_1\mathbf{p}_+ - A_2k_1\mathbf{s} + B_1k_1\mathbf{p}_- - B_2k_1\mathbf{s} - C_1(\mathbf{k}_{to} \times \mathbf{e}_o) - C_2(\mathbf{k}_{te} \times \mathbf{e}_e)] \times \mathbf{n} = 0 \quad \text{(A.11)}$$

$$\mathbf{s} \cdot [A_1k_1\mathbf{p}_+ - A_2k_1\mathbf{s} + B_1k_1\mathbf{p}_- - B_2k_1\mathbf{s} - C_1(\mathbf{k}_{to} \times \mathbf{e}_o) - C_2(\mathbf{k}_{te} \times \mathbf{e}_e)] \times \mathbf{n} = 0 \quad \text{(A.12)}$$

A bit of simple vector manipulation yields

$$[A_1\mathbf{s} + A_2\mathbf{p}_\pm + B_1\mathbf{s} + B_2\mathbf{p}_\mp - C_1\mathbf{e}_o - C_2\mathbf{e}_e] \cdot \mathbf{s} = 0 \quad \text{(A.13)}$$

$$[A_1\mathbf{s} + A_2\mathbf{p}_\pm + B_1\mathbf{s} + B_2\mathbf{p}_\mp - C_1\mathbf{e}_o - C_2\mathbf{e}_e] \cdot \mathbf{k}_\rho = 0 \quad \text{(A.14)}$$

$$[A_1k_1\mathbf{p}_\pm - A_2k_1\mathbf{s} + B_1k_1\mathbf{p}_\mp - B_2k_1\mathbf{s} - C_1(\mathbf{k}_{to} \times \mathbf{e}_o) - C_2(\mathbf{k}_{te} \times \mathbf{e}_e)] \cdot \mathbf{s} = 0 \quad \text{(A.15)}$$

$$[A_1k_1\mathbf{p}_\pm - A_2k_1\mathbf{s} + B_1k_1\mathbf{p}_\mp - B_2k_1\mathbf{s} - C_1(\mathbf{k}_{to} \times \mathbf{e}_o) - C_2(\mathbf{k}_{te} \times \mathbf{e}_e)] \cdot \mathbf{k}_\rho = 0 \quad \text{(A.16)}$$

where $\mathbf{k}_\rho = \mathbf{n} \times \mathbf{s}$ is a unit vector. Using the orthonormality relations $\mathbf{s} \cdot \mathbf{p}_\pm = 0$, $\mathbf{s} \cdot \mathbf{k}_\rho = 0$, and $\mathbf{s} \cdot \mathbf{s} = 1$, we get

$$A_1 + B_1 - C_1(\mathbf{e}_o \cdot \mathbf{s}) - C_2(\mathbf{e}_e \cdot \mathbf{s}) = 0 \tag{A.17}$$

$$A_2 - B_2 - C_1\frac{(\mathbf{e}_o \cdot \mathbf{k}_\rho)}{(\mathbf{p}_\pm \cdot \mathbf{k}_\rho)} - C_2\frac{(\mathbf{e}_e \cdot \mathbf{k}_\rho)}{(\mathbf{p}_\pm \cdot \mathbf{k}_\rho)} = 0 \tag{A.18}$$

$$A_2 + B_2 + C_1\frac{(\mathbf{k}_{to} \times \mathbf{e}_o) \cdot \mathbf{s}}{k_1} + C_2\frac{(\mathbf{k}_{te} \times \mathbf{e}_e) \cdot \mathbf{s}}{k_1} = 0 \tag{A.19}$$

$$A_1 - B_1 - C_1\frac{(\mathbf{k}_{to} \times \mathbf{e}_o) \cdot \mathbf{k}_\rho}{k_1(\mathbf{p}_\pm \cdot \mathbf{k}_\rho)} - C_2\frac{(\mathbf{k}_{te} \times \mathbf{e}_e) \cdot \mathbf{k}_\rho}{k_1(\mathbf{p}_\pm \cdot \mathbf{k}_\rho)} = 0 \tag{A.20}$$

where we used $\mathbf{p}_\pm \cdot \mathbf{k}_\rho = \pm k_{z1}/k_1$. Further manipulation yields

$$A_1 = \frac{C_1}{2k_{z1}}(\mathbf{e}_o \cdot \mathbf{s})(k_{z1} + k_{zo}) + \frac{C_2}{2k_{z1}}(\mathbf{e}_e \cdot \mathbf{s})(k_{z1} + k_{ze}) \tag{A.21}$$

$$B_1 = \frac{C_1}{2k_{z1}}(\mathbf{e}_o \cdot \mathbf{s})(k_{z1} - k_{zo}) + \frac{C_2}{2k_{z1}}(\mathbf{e}_e \cdot \mathbf{s})(k_{z1} - k_{ze}) \tag{A.22}$$

$$A_2 = \pm\frac{C_1}{2k_{z1}k_1}[k_1^2(\mathbf{e}_o \cdot \mathbf{k}_\rho) \mp k_{z1}(\mathbf{k}_{to} \times \mathbf{e}_o) \cdot \mathbf{s}] \pm \frac{C_2}{2k_{z1}k_1}[k_1^2(\mathbf{e}_e \cdot \mathbf{k}_\rho) \mp k_{z1}(\mathbf{k}_{te} \times \mathbf{e}_e) \cdot \mathbf{s}] \tag{A.23}$$

$$B_2 = \mp\frac{C_1}{2k_{z1}k_1}[k_1^2(\mathbf{e}_o \cdot \mathbf{k}_\rho) \pm k_{z1}(\mathbf{k}_{to} \times \mathbf{e}_o) \cdot \mathbf{s}] \mp \frac{C_2}{2k_{z1}k_1}[k_1^2(\mathbf{e}_e \cdot \mathbf{k}_\rho) \pm k_{z1}(\mathbf{k}_{te} \times \mathbf{e}_e) \cdot \mathbf{s}] \tag{A.24}$$

We can now write the results in matrix form as

$$\begin{pmatrix} A_1 \\ A_2 \end{pmatrix} = \begin{pmatrix} a & b \\ \pm c & \pm d \end{pmatrix} \begin{pmatrix} C_1 \\ C_2 \end{pmatrix} \tag{A.25}$$

which we can invert to get

$$\begin{pmatrix} C_1 \\ C_2 \end{pmatrix} = \begin{pmatrix} t_{11} & t_{12} \\ t_{21} & t_{22} \end{pmatrix} \begin{pmatrix} A_1 \\ A_2 \end{pmatrix} \tag{A.26}$$

where

$$t_{11} = \frac{2k_{z1}}{\Delta}[k_1^2(\mathbf{k}_\rho \cdot \mathbf{e}_e) \mp k_{z1}\mathbf{s} \cdot (\mathbf{k}_{te} \times \mathbf{e}_e)] \tag{A.27}$$

$$t_{12} = \mp\frac{2k_{z1}k_1}{\Delta}(\mathbf{s} \cdot \mathbf{e}_e)(k_{z1} + k_{ze}) \tag{A.28}$$

$$t_{21} = -\frac{2k_{z1}}{\Delta}[k_1^2(\mathbf{k}_\rho \cdot \mathbf{e}_o) \mp k_{z1}\mathbf{s} \cdot (\mathbf{k}_{to} \times \mathbf{e}_o)] \tag{A.29}$$

$$t_{22} = \pm\frac{2k_{z1}k_1}{\Delta}(\mathbf{s} \cdot \mathbf{e}_o)(k_{z1} + k_{zo}) \tag{A.30}$$

where

$$\Delta = (\mathbf{s}\cdot\mathbf{e}_o)(k_{z1}+k_{zo})[k_1^2(\mathbf{k}_\rho\cdot\mathbf{e}_e)\mp k_{z1}\mathbf{s}\cdot(\mathbf{k}_{te}\times\mathbf{e}_e)]-(\mathbf{s}\cdot\mathbf{e}_e)(k_{z1}+k_{ze})[k_1^2(\mathbf{k}_\rho\cdot\mathbf{e}_o)\mp k_{z1}\mathbf{s}\cdot(\mathbf{k}_{to}\times\mathbf{e}_o)] \tag{A.31}$$

Similarly, we have

$$\begin{aligned}\begin{pmatrix} B_1 \\ B_2 \end{pmatrix} &= \begin{pmatrix} a' & b' \\ \mp c' & \mp d' \end{pmatrix} \begin{pmatrix} C_1 \\ C_2 \end{pmatrix} \\ &= \begin{pmatrix} a' & b' \\ \mp c' & \mp d' \end{pmatrix} \begin{pmatrix} t_{11} & t_{12} \\ t_{21} & t_{22} \end{pmatrix} \begin{pmatrix} A_1 \\ A_2 \end{pmatrix} \\ &= \begin{pmatrix} a't_{11}+b't_{21} & a't_{12}+b't_{22} \\ \mp c't_{11}\mp d't_{21} & \mp c't_{12}\mp d't_{22} \end{pmatrix} \begin{pmatrix} A_1 \\ A_2 \end{pmatrix}\end{aligned} \tag{A.32}$$

or

$$\begin{pmatrix} B_1 \\ B_2 \end{pmatrix} = \begin{pmatrix} r_{11} & r_{12} \\ r_{21} & r_{22} \end{pmatrix} \begin{pmatrix} A_1 \\ A_2 \end{pmatrix} \tag{A.33}$$

where

$$\begin{aligned} r_{11} &= \frac{1}{\Delta}(\mathbf{s}\cdot\mathbf{e}_o)(k_{z1}-k_{zo})[k_1^2(\mathbf{k}_\rho\cdot\mathbf{e}_e)\mp k_{z1}\mathbf{s}\cdot(\mathbf{k}_{te}\times\mathbf{e}_e)] \\ &\quad -\frac{1}{\Delta}(\mathbf{s}\cdot\mathbf{e}_e)(k_{z1}-k_{ze})[k_1^2(\mathbf{k}_\rho\cdot\mathbf{e}_o)\mp k_{z1}\mathbf{s}\cdot(\mathbf{k}_{to}\times\mathbf{e}_o)] \qquad \text{(A.34)} \\ r_{12} &= \pm\frac{2k_{z1}k_1}{\Delta}(\mathbf{s}\cdot\mathbf{e}_e)(\mathbf{s}\cdot\mathbf{e}_o)(k_{zo}-k_{ze}) \qquad \text{(A.35)} \\ r_{21} &= \frac{2k_{z1}k_1}{\Delta}[\mathbf{s}\cdot(\mathbf{k}_{te}\times\mathbf{e}_e)(\mathbf{k}_\rho\cdot\mathbf{e}_o)-\mathbf{s}\cdot(\mathbf{k}_{to}\times\mathbf{e}_o)(\mathbf{k}_\rho\cdot\mathbf{e}_e)] \qquad \text{(A.36)} \\ r_{22} &= \frac{1}{\Delta}(\mathbf{s}\cdot\mathbf{e}_e)(k_{z1}+k_{ze})[k_1^2(\mathbf{k}_\rho\cdot\mathbf{e}_o)\pm k_{z1}\mathbf{s}\cdot(\mathbf{k}_{to}\times\mathbf{e}_o)] \\ &\quad -\frac{1}{\Delta}(\mathbf{s}\cdot\mathbf{e}_o)(k_{z1}+k_{zo})[k_1^2(\mathbf{k}_\rho\cdot\mathbf{e}_e)\pm k_{z1}\mathbf{s}\cdot(\mathbf{k}_{te}\times\mathbf{e}_e)] \qquad \text{(A.37)}\end{aligned}$$

Specific Examples

We will now use the formulas from the previous section. Here, we will specify the geometry of the optic axis and basis vectors. The results will be used to calculate the Green function of a dipole above a regular hyperbolic medium, as well as a hyperbolic meta-surface.

A.1.1 Optic axis perpendicular to interface: Bulk Hyperbolic Medium

Let $\mathbf{c} = \mathbf{z}$, so that the basis vectors are defined as

$$\mathbf{s} = \frac{1}{\sqrt{k_x^2 + k_y^2}} \begin{pmatrix} k_y \\ -k_x \\ 0 \end{pmatrix}, \quad \mathbf{p}_\pm = \frac{1}{k_1 \sqrt{k_x^2 + k_y^2}} \begin{pmatrix} \pm k_x k_z \\ \pm k_y k_z \\ -(k_x^2 + k_y^2) \end{pmatrix} , \tag{A.38}$$

$$\mathbf{e}_o = \frac{1}{\sqrt{k_x^2 + k_y^2}} \begin{pmatrix} k_y \\ -k_x \\ 0 \end{pmatrix} \text{ and } \mathbf{e}_e^\pm = \frac{1}{\sqrt{\epsilon_x} k_o \sqrt{k_x^2 + k_y^2}} \begin{pmatrix} \pm k_x k_{zp} \\ \pm k_y k_{zp} \\ -(k_x^2 + k_y^2)\frac{\epsilon_x}{\epsilon_z} \end{pmatrix} \tag{A.39}$$

We now calculate

$$\mathbf{k}_\rho \cdot \mathbf{e}_o = 0 \ , \ \mathbf{k}_\rho \cdot \mathbf{e}_e = \frac{k_{ze}}{\sqrt{\epsilon_x} k_o} \ , \ \mathbf{s} \cdot (\mathbf{k}_{te} \times \mathbf{e}_e) = -\sqrt{\epsilon_x} k_o \ , \ \mathbf{s} \cdot (\mathbf{k}_{to} \times \mathbf{e}_o) = 0 \ , \ \mathbf{s} \cdot \mathbf{e}_o = 1 \ , \ \mathbf{s} \cdot \mathbf{e}_e = 0 \tag{A.40}$$

We therefore get

$$\Delta = \frac{k_o}{\sqrt{\epsilon_x}} (k_{z1} + k_{zo})(\epsilon_1 k_{ze} + \epsilon_x k_{z1}) \tag{A.41}$$

which leads to the transmission coefficients

$$t_{11} = \frac{2k_{z1}}{k_{z1} + k_{zo}} \ , \ t_{12} = t_{21} = 0 \ , \ t_{22} = \frac{2\epsilon_x k_{z1}}{\epsilon_x k_{z1} + k_z^p \epsilon_1} \sqrt{\frac{\epsilon_1}{\epsilon_x}} \tag{A.42}$$

and the reflection coefficients

$$r_{11} = \frac{k_{z1} - k_{zo}}{k_{z1} + k_{zo}} \ , \ r_{12} = r_{21} = 0 \ , \ r_{22} = \frac{\epsilon_x k_{z1} - \epsilon_1 k_{ze}}{\epsilon_x k_{z1} + \epsilon_1 k_{ze}} \tag{A.43}$$

A.1.2 Optic axis parallel to interface: application to hyperbolic Metasurface

Let $\mathbf{c} = \mathbf{x}$ and the normal $\mathbf{n} = \mathbf{z}$ so that the basis vectors are defined as

$$\mathbf{s}_1 = \frac{1}{\sqrt{k_x^2 + k_y^2}} \begin{pmatrix} k_y \\ -k_x \\ 0 \end{pmatrix}, \quad \mathbf{p}_\pm = \frac{1}{k_1\sqrt{k_x^2 + k_y^2}} \begin{pmatrix} \pm k_x k_z \\ \pm k_y k_z \\ -(k_x^2 + k_y^2) \end{pmatrix} \tag{A.44}$$

We emphasize that the basis vectors in a uniaxial medium are defined with respect to the optic axis, such that

$$\mathbf{e}_o = \frac{1}{\sqrt{k_{zo}^2 + k_y^2}} \begin{pmatrix} 0 \\ \pm k_{zo} \\ -k_y \end{pmatrix}, \quad \mathbf{e}_{e\pm} = \frac{1}{\sqrt{\epsilon_z} k_o \sqrt{k_{ze}^2 + k_y^2}} \begin{pmatrix} -(k_{ze}^2 + k_y^2)\frac{\epsilon_z}{\epsilon_x} \\ k_y k_x \\ \pm k_x k_{ze} \end{pmatrix} \tag{A.45}$$

We now calculate

$$\mathbf{k}_\rho \cdot \mathbf{e}_o = \frac{\pm k_y k_{zo}}{\sqrt{k_x^2 + k_y^2}\sqrt{k_y^2 + k_{zo}^2}}, \; \mathbf{k}_\rho \cdot \mathbf{e}_e = \frac{-k_x k_{zo}^2}{\sqrt{\epsilon_z} k_o \sqrt{k_{ze}^2 + k_y^2}\sqrt{k_x^2 + k_y^2}} \tag{A.46}$$

$$\mathbf{s} \cdot (\mathbf{k}_{to} \times \mathbf{e}_o) = -\frac{\epsilon_z k_o^2 k_y}{\sqrt{k_{zo}^2 + k_y^2}\sqrt{k_x^2 + k_y^2}}, \; \mathbf{s} \cdot (\mathbf{k}_{te} \times \mathbf{e}_e) = \frac{\pm\sqrt{\epsilon_z} k_o k_x k_{ze}}{\sqrt{k_{ze}^2 + k_y^2}\sqrt{k_x^2 + k_y^2}} \tag{A.47}$$

$$\mathbf{s} \cdot \mathbf{e}_o = \frac{\mp k_x k_{zo}}{\sqrt{k_x^2 + k_y^2}\sqrt{k_y^2 + k_{zo}^2}}, \; \mathbf{s} \cdot \mathbf{e}_e = \frac{-\sqrt{\epsilon_z} k_y k_o}{\sqrt{k_{ze}^2 + k_y^2}\sqrt{k_x^2 + k_y^2}} \tag{A.48}$$

The denominator can then be written as

$$\Delta = \pm \frac{k_x^2 k_{zo} k_o (k_{z1} + k_{zo})(\epsilon_1 k_{zo}^2 + \epsilon_z k_{z1} k_{ze}) + \epsilon_z k_y^2 k_o^3 (k_{z1} + k_{ze})(\epsilon_1 k_{zo} + \epsilon_z k_{z1})}{\sqrt{\epsilon_z}(k_x^2 + k_y^2)\sqrt{k_{zo}^2 + k_y^2}\sqrt{k_{ze}^2 + k_y^2}} \tag{A.49}$$

so that we get

$$t_{11} = -\frac{2k_{z1}k_x k_o}{\sqrt{\epsilon_z}\Delta}\frac{\epsilon_1 k_{zo}^2 + \epsilon_z k_{z1}k_{ze}}{\sqrt{(k_x^2+k_y^2)(k_{ze}^2+k_y^2)}} \tag{A.50}$$

$$t_{12} = \pm\frac{2k_{z1}k_y k_o^2}{\Delta}\frac{(k_{z1}+k_{ze})\sqrt{\epsilon_1\epsilon_z}}{\sqrt{(k_x^2+k_y^2)(k_{ze}^2+k_y^2)}} \tag{A.51}$$

$$t_{21} = \mp\frac{2k_{z1}k_y k_o^2}{\Delta}\frac{\epsilon_1 k_{zo} + \epsilon_z k_{z1}}{\sqrt{(k_x^2+k_y^2)(k_y^2+k_{zo}^2)}} \tag{A.52}$$

$$t_{22} = -\frac{2k_{z1}k_{zo}k_1 k_x}{\Delta}\frac{k_{z1}+k_{zo}}{\sqrt{(k_x^2+k_y^2)(k_y^2+k_{zo}^2)}} \tag{A.53}$$

similarly we get the following reflection coefficients

$$r_{11} = \pm\frac{k_x^2 k_o k_{zo}(k_{z1}-k_{zo})(\epsilon_1 k_{zo}^2 + \epsilon_z k_{z1}k_{ze}) + \epsilon_z k_y^2 k_o^3(k_{z1}-k_{ze})(\epsilon_1 k_{zo}+\epsilon_z k_{z1})}{\sqrt{\epsilon_z}\Delta(k_x^2+k_y^2)\sqrt{(k_y^2+k_{zo}^2)(k_y^2+k_{ze}^2)}} \tag{A.54}$$

$$r_{12} = \frac{2k_{z1}k_{zo}k_x k_y k_o^2(k_{zo}-k_{ze})\sqrt{\epsilon_1\epsilon_z}}{\Delta(k_x^2+k_y^2)\sqrt{(k_y^2+k_{zo}^2)(k_y^2+k_{ze}^2)}} = -r_{21} \tag{A.55}$$

$$r_{22} = \mp\frac{\epsilon_z k_y^2 k_o^3(k_{z1}+k_{ze})(\epsilon_1 k_{zo}-\epsilon_z k_{z1}) + k_x^2 k_{zo}k_o(k_{z1}+k_{zo})(\epsilon_1 k_{zo}^2 - \epsilon_z k_{z1}k_{ze})}{\sqrt{\epsilon_z}\Delta(k_x^2+k_y^2)\sqrt{(k_y^2+k_{zo}^2)(k_y^2+k_{ze}^2)}} \tag{A.56}$$

Homogeneous and scattered Green functions

In the following, we provide explicit expressions for the bulk Green function as well as the scattered (reflected and transmitted) Green functions. The dyadic Green function approach can be used to calculate the electric and magnetic field profiles of a dipole, as well as the resonant dipole-dipole interaction, Casimir-Polder interaction, etc. in an arbitrary multilayered environments. In particular, we will demonstrate how to simplify the Green function to a single 1-d integral that can be readily calculated via numerical methods. This approach can easiliy be generalized for spatially dispersive materials.

Simplification of bulk DGF

The non-singular part of the homogeneous dyadic Green function in an isotropic medium is given by

$$\mathbf{G}_o(\mathbf{r}) = \frac{i}{8\pi^2}\int dk_x dk_y e^{i\mathbf{k}_\rho\cdot\rho}\left[\mathbf{I} - \frac{\mathbf{kk}}{k_1^2}\right]\frac{e^{ik_z z}}{k_z} \tag{A.57}$$

$$= \frac{i}{8\pi^2}\int dk_x dk_y e^{i\mathbf{k}_\rho\cdot\rho}\left[\mathbf{p}_\pm\mathbf{p}_\pm + \mathbf{ss}\right]\frac{e^{ik_z z}}{k_z} \tag{A.58}$$

where

$$\mathbf{s} = \frac{1}{\sqrt{k_x^2+k_y^2}}\begin{pmatrix} k_y \\ -k_x \\ 0 \end{pmatrix} \quad \text{and} \quad \mathbf{p}_\pm = \frac{1}{k_1\sqrt{k_x^2+k_y^2}}\begin{pmatrix} \pm k_x k_z \\ \pm k_y k_z \\ -(k_x^2+k_y^2) \end{pmatrix} \tag{A.59}$$

where $\pm$ refers to directions above/below the dipole respectively. We can simplify the integral by converting to cylindrical coordinates, using

$$k_x = k_\rho\cos\phi \quad , \quad k_y = k_\rho\sin\phi$$
$$x = \rho\cos\theta \quad , \quad y = \rho\sin\theta.$$

and

$$\int_{-\infty}^{\infty} dk_x dk_y\, e^{i\mathbf{k}_\rho\cdot\rho} = \int_0^\infty dk_\rho k_\rho \int_0^{2\pi} d\phi\; e^{ik_\rho\rho\cos(\phi-\theta)}.$$

The dyadic terms are then explicitly written as

$$\mathbf{ss} = \begin{pmatrix} \sin^2\phi & -\cos\phi\sin\phi & 0 \\ -\cos\phi\sin\phi & \cos^2\phi & 0 \\ 0 & 0 & 0 \end{pmatrix} \tag{A.60}$$

and

$$\mathbf{p}_\pm\mathbf{p}_\pm = \frac{1}{k_1^2}\begin{pmatrix} k_z^2\cos^2\phi & k_z^2\cos\phi\sin\phi & \mp k_\rho k_z\cos\phi \\ k_z^2\cos\phi\sin\phi & k_z^2\sin^2\phi & \mp k_\rho k_z\sin\phi \\ \mp k_\rho k_z\cos\phi & \mp k_\rho k_z\sin\phi & k_\rho^2 \end{pmatrix} \tag{A.61}$$

Integrating over angle ϕ yields

$$\int_0^{2\pi} d\phi\; e^{ik_\rho \rho\cos(\phi-\theta)}\mathbf{ss} = \frac{2\pi}{2}\begin{pmatrix} J_o + J_2\cos 2\theta & J_2\sin 2\theta & 0 \\ J_2\sin 2\theta & J_o - J_2\cos 2\theta & 0 \\ 0 & 0 & 0 \end{pmatrix} \tag{A.62}$$

$$\int_0^{2\pi} d\phi\; e^{ik_\rho \rho\cos(\phi-\theta)}\mathbf{p}_\pm\mathbf{p}_\pm = \frac{2\pi}{2k_1^2}\begin{pmatrix} k_z^2(J_o - J_2\cos 2\theta) & -k_z^2 J_2\sin 2\theta & \mp 2ik_\rho k_z J_1\cos\theta \\ -k_z^2 J_2\sin 2\theta & k_z^2(J_o + J_2\cos 2\theta) & \mp 2ik_\rho k_z J_1\sin\theta \\ \mp 2ik_\rho k_z J_1\cos\theta & \mp 2ik_\rho k_z J_1\sin\theta & 2k_\rho^2 J_o \end{pmatrix} \tag{A.63}$$

where we used the identities: $2\sin\phi\cos\phi = \sin 2\phi$, $\sin^2\phi = (1-\cos 2\phi)/2$, $\cos^2\phi = (1+\cos 2\phi)/2$, and

$$\int_0^{2\pi} d\phi \cos(n\phi) e^{ik_\rho\rho\cos(\phi-\theta)} = 2\pi i^n J_n(k_\rho\rho)\cos(n\theta) \tag{A.64}$$

$$\int_0^{2\pi} d\phi \sin(n\phi) e^{ik_\rho\rho\cos(\phi-\theta)} = 2\pi i^n J_n(k_\rho\rho)\sin(n\theta) \tag{A.65}$$

The result is easily proven by variable substitution, expanding the exponential function, and then using the summation definition of the cylindrical bessel function of order n. The final result is written as

$$\begin{aligned}
G_{xx}(\mathbf{r}) &= \frac{i}{8\pi k_1^2}\int dk_\rho \frac{k_\rho}{k_z} e^{ik_z|z-z_o|}\left[k_1^2 J_+ + k_z^2 J_-\right] \\
G_{xy}(\mathbf{r}) &= \frac{i}{8\pi k_1^2}\int dk_\rho \frac{k_\rho}{k_z} e^{ik_z|z-z_o|}\left[k_1^2 J_2^s - k_z^2 J_2^s\right] \\
G_{xz}(\mathbf{r}) &= \frac{i}{8\pi k_1^2}\int dk_\rho k_\rho^2 e^{ik_z|z-z_o|}\left[\mp 2i J_1^c\right] \\
G_{yy}(\mathbf{r}) &= \frac{i}{8\pi k_1^2}\int dk_\rho \frac{k_\rho}{k_z} e^{ik_z|z-z_o|}\left[k_1^2 J_- + k_z^2 J_+\right] \\
G_{yz}(\mathbf{r}) &= \frac{i}{8\pi k_1^2}\int dk_\rho k_\rho^2 e^{ik_z|z-z_o|}\left[\mp 2i J_1^s\right] \\
G_{zz}(\mathbf{r}) &= \frac{i}{8\pi k_1^2}\int dk_\rho \frac{k_\rho^3}{k_z} e^{ik_z|z-z_o|} 2J_o(k_\rho\rho)
\end{aligned}$$

Note that $G_{xy} = G_{yx}$, $G_{xz} = G_{zx}$, $G_{yz} = G_{zy}$. We have also defined the shorthand notation for the cylindrical bessel functions

$$J_2^c = J_2(k_\rho \rho)\cos 2\theta \tag{A.66}$$

$$J_2^s = J_2(k_\rho \rho)\sin 2\theta \tag{A.67}$$

$$J_1^c = J_1(k_\rho \rho)\cos \theta \tag{A.68}$$

$$J_1^s = J_1(k_\rho \rho)\sin \theta \tag{A.69}$$

$$J_\pm = J_o(k_\rho \rho) \pm J_2(k_\rho \rho)\cos 2\theta \tag{A.70}$$

Scattered DGF above a uniaxial half-space

Consider a dipole in an isotropic medium that is a distance d above a general half-space. The scattered dyadic Green function will take the form

$$\mathbf{G}_s(\mathbf{r}) = \frac{i}{8\pi^2}\int dk_x dk_y e^{i\mathbf{k}_\rho \cdot \rho}\left[r_{pp}(\mathbf{p}_+\mathbf{p}_-) + r_{sp}(\mathbf{s}\mathbf{p}_-) + r_{ps}(\mathbf{p}_+\mathbf{s}) + r_{ss}(\mathbf{s}\mathbf{s})\right]\frac{e^{ik_z(d+z)}}{k_z} \tag{A.71}$$

Let us simplify the double integral as before by writing out the dyadic terms in cylindrical coordinates:

$$\mathbf{p}_+\mathbf{p}_- = \frac{1}{k_1^2}\begin{pmatrix} -k_z^2\cos^2\phi & -k_z^2\cos\phi\sin\phi & -k_\rho k_z\cos\phi \\ -k_z^2\cos\phi\sin\phi & -k_z^2\sin^2\phi & -k_\rho k_z\sin\phi \\ k_\rho k_z\cos\phi & k_\rho k_z\sin\phi & k_\rho^2 \end{pmatrix}$$

$$\mathbf{p}_+\mathbf{s} = \frac{1}{k_1}\begin{pmatrix} k_z\cos\phi\sin\phi & -k_z\cos^2\phi & 0 \\ k_z\sin^2\phi & -k_z\cos\phi\sin\phi & 0 \\ -k_\rho\sin\phi & k_\rho\cos\phi & 0 \end{pmatrix}$$

$$\mathbf{s}\mathbf{p}_- = \frac{1}{k_1}\begin{pmatrix} -k_z\cos\phi\sin\phi & -k_z\sin^2\phi & -k_\rho\sin\phi \\ k_z\cos^2\phi & k_z\cos\phi\sin\phi & k_\rho\cos\phi \\ 0 & 0 & 0 \end{pmatrix}$$

Explicitly, the double integral result is given by

$$G_{xx}(\mathbf{r}) = \frac{i}{8\pi^2 k_1^2}\int dk_\rho d\phi\ \frac{k_\rho}{k_z}[r_{ss}k_1^2 s^2\phi + k_1 k_z c(\phi)s(\phi)(r_{ps}-r_{sp}) - r_{pp}k_z^2 c^2\phi]e^{ik_\rho\rho\cos(\phi-\theta)+ik_z(z+d)} \tag{A.72}$$

$$G_{xy}(\mathbf{r}) = \frac{i}{8\pi^2 k_1^2}\int dk_\rho d\phi\ \frac{k_\rho}{k_z}[-r_{ss}k_1^2 s(2\phi)/2 - (r_{ps}c^2\phi + r_{sp}s^2\phi)k_1 k_z - r_{pp}k_z^2 s(2\phi)/2]e^{ik_\rho\rho\cos(\phi-\theta)+ik_z(z+d)} \tag{A.73}$$

$$G_{xz}(\mathbf{r}) = \frac{i}{8\pi^2 k_1^2}\int dk_\rho d\phi\ \frac{k_\rho}{k_z}[-r_{sp}k_1 k_\rho s(\phi) - r_{pp}k_\rho k_z c(\phi)]e^{ik_\rho\rho\cos(\phi-\theta)+ik_z(z+d)} \tag{A.74}$$

$$G_{yx}(\mathbf{r}) = \frac{i}{8\pi^2 k_1^2}\int dk_\rho d\phi\ \frac{k_\rho}{k_z}[-r_{ss}k_1^2 s(2\phi)/2 + (r_{ps}s^2\phi + r_{sp}c^2\phi)k_1 k_z - r_{pp}k_z^2 s(2\phi)/2]e^{ik_\rho\rho\cos(\phi-\theta)+ik_z(z+d)} \tag{A.75}$$

$$G_{yy}(\mathbf{r}) = \frac{i}{8\pi^2 k_1^2}\int dk_\rho d\phi\ \frac{k_\rho}{k_z}[r_{ss}k_1^2 c^2\phi - (r_{ps}-r_{sp})k_1 k_z c(\phi)s(\phi) - r_{pp}k_z^2 s^2\phi]e^{ik_\rho\rho\cos(\phi-\theta)+ik_z(z+d)} \tag{A.76}$$

$$G_{yz}(\mathbf{r}) = \frac{i}{8\pi^2 k_1^2}\int dk_\rho d\phi\ \frac{k_\rho}{k_z}\,[r_{sp}k_1 k_\rho c(\phi) - r_{pp}k_\rho k_z s(\phi)]e^{ik_\rho\rho\cos(\phi-\theta)+ik_z(z+d)} \tag{A.77}$$

$$G_{zx}(\mathbf{r}) = \frac{i}{8\pi^2 k_1^2}\int dk_\rho d\phi\ \frac{k_\rho}{k_z}\,[-r_{ps}k_1 k_\rho s(\phi) + r_{pp}k_\rho k_z c(\phi)]e^{ik_\rho\rho\cos(\phi-\theta)+ik_z(z+d)} \tag{A.78}$$

$$G_{zy}(\mathbf{r}) = \frac{i}{8\pi^2 k_1^2}\int dk_\rho d\phi\ \frac{k_\rho}{k_z}\,[+r_{ps}k_1 k_\rho c(\phi) + r_{pp}k_\rho k_z s(\phi)]e^{ik_\rho\rho\cos(\phi-\theta)+ik_z(z+d)} \tag{A.79}$$

$$G_{zz}(\mathbf{r}) = \frac{i}{8\pi^2 k_1^2}\int dk_\rho d\phi\ \frac{k_\rho^3}{k_z}r_{pp}\,e^{ik_\rho\rho\cos(\phi-\theta)+ik_z(z+d)} \tag{A.80}$$

This is the main result that will be necessary when the symmetry along the $x-y$ plane is broken. In such cases, the reflection coefficients will depend on the magnitude of wavevector as well as the angle, e.g. $r_{11} = r_{11}(k_\rho, \phi)$. This will be important when we consider a uniaxial medium with the optic axis lying in the $x-y$ plane.

For media that has $x-y$ symmetry, we can integrate over the angle ϕ,

$$\int_0^{2\pi} d\phi\ e^{ik_\rho\rho\cos(\phi-\theta)}\mathbf{p}_+\mathbf{p}_- = \frac{2\pi}{2k_1^2}\begin{pmatrix} -k_z^2(J_o - J_2\cos 2\theta) & k_z^2 J_2\sin 2\theta & -2ik_\rho k_z J_1\cos\theta \\ k_z^2 J_2\sin 2\theta & -k_z^2(J_o + J_2\cos 2\theta) & -2ik_\rho k_z J_1\sin\theta \\ 2ik_\rho k_z J_1\cos\theta & 2ik_\rho k_z J_1\sin\theta & 2k_\rho^2 J_o \end{pmatrix} \tag{A.81}$$

$$\int_0^{2\pi} d\phi\; e^{ik_\rho \rho\cos(\phi-\theta)}\mathbf{p}_+\mathbf{s} = \frac{2\pi}{2k_1}\begin{pmatrix} -k_z J_2\sin 2\theta & -k_z(J_o - J_2\cos 2\theta) & 0 \\ k_z(J_o + J_2\cos 2\theta) & k_z J_2\sin 2\theta & 0 \\ -2ik_\rho J_1\sin\theta & 2ik_\rho J_1\cos\theta & 0 \end{pmatrix} \tag{A.82}$$

$$\int_0^{2\pi} d\phi\; e^{ik_\rho \rho\cos(\phi-\theta)}\mathbf{s}\mathbf{p}_- = \frac{2\pi}{2k_1}\begin{pmatrix} k_z J_2\sin 2\theta & -k_z(J_o + J_2\cos 2\theta) & -2ik_\rho J_1\sin\theta \\ k_z(J_o - J_2\cos 2\theta) & -k_z J_2\sin 2\theta & 2ik_\rho J_1\cos\theta \\ 0 & 0 & 0 \end{pmatrix} \tag{A.83}$$

yielding the final result

$$G_{xx}(\mathbf{r}) = \frac{i}{8\pi k_1^2}\int dk_\rho \frac{k_\rho}{k_z} e^{ik_z(z+d)}\left[k_1^2 J_+^c r_{ss} - k_1 k_z J_2^s r_{ps} + k_1 k_z J_2^s r_{sp} - k_z^2 J_-^c r_{pp}\right] \tag{A.84}$$

$$G_{xy}(\mathbf{r}) = \frac{i}{8\pi k_1^2}\int dk_\rho \frac{k_\rho}{k_z} e^{ik_z(z+d)}\left[k_1^2 J_2^s r_{ss} - k_1 k_z J_-^c r_{ps} - k_1 k_z J_+^c r_{sp} + k_z^2 J_2^s r_{pp}\right] \tag{A.85}$$

$$G_{xz}(\mathbf{r}) = \frac{i}{8\pi k_1^2}\int dk_\rho \frac{k_\rho}{k_z} e^{ik_z(z+d)}\left[-2ik_1 k_\rho J_1^s r_{sp} - 2ik_\rho k_z J_1^c r_{pp}\right] \tag{A.86}$$

$$G_{yx}(\mathbf{r}) = \frac{i}{8\pi k_1^2}\int dk_\rho \frac{k_\rho}{k_z} e^{ik_z(z+d)}\left[k_1^2 J_2^s r_{ss} + k_1 k_z J_+^c r_{ps} + k_1 k_z J_-^c r_{sp} + k_z^2 J_2^s r_{pp}\right] \tag{A.87}$$

$$G_{yy}(\mathbf{r}) = \frac{i}{8\pi k_1^2}\int dk_\rho \frac{k_\rho}{k_z} e^{ik_z(z+d)}\left[k_1^2 J_-^c r_{ss} + k_1 k_z J_2^s r_{ps} - k_1 k_z J_2^s r_{sp} - k_z^2 J_+^c r_{pp}\right] \tag{A.88}$$

$$G_{yz}(\mathbf{r}) = \frac{i}{8\pi k_1^2}\int dk_\rho \frac{k_\rho}{k_z} e^{ik_z(z+d)}\left[2ik_1 k_\rho J_1^c r_{sp} - 2ik_\rho k_z J_1^s r_{pp}\right] \tag{A.89}$$

$$G_{zx}(\mathbf{r}) = \frac{i}{8\pi k_1^2}\int dk_\rho \frac{k_\rho}{k_z} e^{ik_z(z+d)}\left[-2ik_1 k_\rho J_1^s r_{ps} + 2ik_\rho k_z J_1^c r_{pp}\right] \tag{A.90}$$

$$G_{zy}(\mathbf{r}) = \frac{i}{8\pi k_1^2}\int dk_\rho \frac{k_\rho}{k_z} e^{ik_z(z+d)}\left[+2ik_1 k_\rho J_1^c r_{ps} + 2ik_\rho k_z J_1^s r_{pp}\right] \tag{A.91}$$

$$G_{zz}(\mathbf{r}) = \frac{i}{8\pi k_1^2}\int dk_\rho \frac{k_\rho}{k_z} e^{ik_z(z+d)}\left[2k_\rho^2 J_o r_{pp}\right] \tag{A.92}$$

We emphasize that this is the most general result that can be used along the $x-y$ plane or the $x-z$ plane.

A.1.3 Transmitted DGF in uniaxial half-space (c = z)

We will first consider the case where the optic axis of the uniaxial medium lies perpendicular to the interface $\mathbf{c} = \mathbf{z}$.

$$\mathbf{G}_t(\mathbf{r}) = \frac{i}{8\pi^2}\int dk_x dk_y \frac{e^{i\mathbf{k}_\rho\cdot\rho + ik_{z1}d}}{k_z}[[t_{pp}(\mathbf{e}_e^- \otimes \mathbf{p}_-) + t_{ps}(\mathbf{e}_e^- \otimes \mathbf{s})]e^{k_{zp}z} + [t_{sp}(\mathbf{e}_o \otimes \mathbf{p}_-) + t_{ss}(\mathbf{e}_o \otimes \mathbf{s})]e^{k_{zs}z}] \tag{A.93}$$

The basis vectors in the uniaxial medium are given by

$$\mathbf{e}_o = \frac{1}{\sqrt{k_x^2 + k_y^2}}\begin{pmatrix} k_y \\ -k_x \\ 0 \end{pmatrix} \quad \text{and} \quad \mathbf{e}_e^- = \frac{1}{\sqrt{\epsilon_x}k_o\sqrt{k_x^2 + k_y^2}}\begin{pmatrix} -k_x k_{zp} \\ -k_y k_{zp} \\ -(k_x^2 + k_y^2)\frac{\epsilon_x}{\epsilon_z} \end{pmatrix} \tag{A.94}$$

The dyadic terms can be written explicitly as

$$\mathbf{e}_o\mathbf{s} = \begin{pmatrix} \sin^2\phi & -\cos\phi\sin\phi & 0 \\ -\cos\phi\sin\phi & \cos^2\phi & 0 \\ 0 & 0 & 0 \end{pmatrix} \tag{A.95}$$

$$\mathbf{e}_e^-\mathbf{p}_- = \frac{1}{\sqrt{\epsilon_1\epsilon_x}k_o^2}\begin{pmatrix} k_z k_z^p \cos^2\phi & k_z k_z^p \cos\phi\sin\phi & k_z^p k_\rho \cos\phi \\ k_z k_z^p \cos\phi\sin\phi & k_z k_z^p \sin^2\phi & k_z^p k_\rho \sin\phi \\ k_\rho k_z \cos\phi\frac{\epsilon_x}{\epsilon_z} & k_\rho k_z \sin\phi\frac{\epsilon_x}{\epsilon_z} & k_\rho^2\frac{\epsilon_x}{\epsilon_z} \end{pmatrix}$$

$$\mathbf{e}_e^-\mathbf{s} = \frac{1}{\sqrt{\epsilon_x}k_o}\begin{pmatrix} -k_z^p\cos\phi\sin\phi & k_z^p\cos^2\phi & 0 \\ -k_z^p\sin^2\phi & k_z^p\cos\phi\sin\phi & 0 \\ -k_\rho\sin\phi\frac{\epsilon_x}{\epsilon_z} & k_\rho\cos\phi\frac{\epsilon_x}{\epsilon_z} & 0 \end{pmatrix}$$

$$\mathbf{e}_o\mathbf{p}_- = \frac{1}{k_1}\begin{pmatrix} -k_z\cos\phi\sin\phi & -k_z\sin^2\phi & -k_\rho\sin\phi \\ k_z\cos^2\phi & k_z\cos\phi\sin\phi & k_\rho\cos\phi \\ 0 & 0 & 0 \end{pmatrix}$$

Applying the same procedure as before, we obtain the double integral result

$$G_{xx}(\mathbf{r}) = \frac{i}{8\pi^2 k_1 k_2}\int dk_\rho d\phi\ \frac{k_\rho}{k_z}[t_{ss}k_1k_2s^2\phi + t_{ps}k_1k_z^p c(\phi)s(\phi) + t_{sp}k_2k_z c(\phi)s(\phi) + t_{pp}k_zk_z^p c^2\phi]e^{ik_\rho\rho\cos(\phi-\theta)+ik_z(z+d)} \tag{A.96}$$

$$G_{xy}(\mathbf{r}) = \frac{i}{8\pi^2 k_1 k_2}\int dk_\rho d\phi\ \frac{k_\rho}{k_z}[-t_{ss}k_1k_2s(2\phi)/2 + t_{ps}k_1k_z^p c^2\phi - t_{sp}k_2k_z s^2\phi + t_{pp}k_zk_z^p s(2\phi)/2]e^{ik_\rho\rho\cos(\phi-\theta)+ik_z(z+d)} \tag{A.97}$$

$$G_{xz}(\mathbf{r}) = \frac{i}{8\pi^2 k_1 k_2}\int dk_\rho d\phi\ \frac{k_\rho}{k_z}[-t_{sp}k_2k_\rho s(\phi) + t_{pp}k_\rho k_z^p c(\phi)]\ e^{ik_\rho\rho\cos(\phi-\theta)+ik_z(z+d)} \tag{A.98}$$

$$G_{yx}(\mathbf{r}) = \frac{i}{8\pi^2 k_1 k_2}\int dk_\rho d\phi\ \frac{k_\rho}{k_z}[-t_{ss}k_1k_2s(2\phi)/2 - t_{ps}k_1k_z^p s^2\phi + t_{sp}k_2k_z c^2\phi + t_{pp}k_zk_z^p s(2\phi)/2]e^{ik_\rho\rho\cos(\phi-\theta)+ik_z(z+d)} \tag{A.99}$$

$$G_{yy}(\mathbf{r}) = \frac{i}{8\pi^2 k_1 k_2}\int dk_\rho d\phi\ \frac{k_\rho}{k_z}[t_{ss}k_1k_2c^2\phi + t_{ps}k_1k_z^p c(\phi)s(\phi) + t_{sp}k_2k_z c(\phi)s(\phi) + t_{pp}k_zk_z^p s^2\phi]e^{ik_\rho\rho\cos(\phi-\theta)+ik_z(z+d)} \tag{A.100}$$

$$G_{yz}(\mathbf{r}) = \frac{i}{8\pi^2 k_1 k_2}\int dk_\rho d\phi\ \frac{k_\rho}{k_z}[t_{sp}k_2k_\rho c(\phi) + t_{pp}k_\rho k_z^p s(\phi)]e^{ik_\rho\rho\cos(\phi-\theta)+ik_z(z+d)} \tag{A.101}$$

$$G_{zx}(\mathbf{r}) = \frac{i}{8\pi^2 k_1 k_2}\int dk_\rho d\phi\ \frac{k_\rho}{k_z}\left[-t_{ps}k_1k_\rho s(\phi)\frac{\epsilon_x}{\epsilon_z} + t_{pp}k_\rho k_z c(\phi)\frac{\epsilon_x}{\epsilon_z}\right]e^{ik_\rho\rho\cos(\phi-\theta)+ik_z(z+d)} \tag{A.102}$$

$$G_{zy}(\mathbf{r}) = \frac{i}{8\pi^2 k_1 k_2}\int dk_\rho d\phi\ \frac{k_\rho}{k_z}\left[+t_{ps}k_1k_\rho c(\phi)\frac{\epsilon_x}{\epsilon_z} + t_{pp}k_\rho k_z s(\phi)\frac{\epsilon_x}{\epsilon_z}\right]e^{ik_\rho\rho\cos(\phi-\theta)+ik_z(z+d)} \tag{A.103}$$

$$G_{zz}(\mathbf{r}) = \frac{i}{8\pi^2 k_1 k_2}\int dk_\rho d\phi\ \frac{k_\rho^3}{k_z}t_{pp}\frac{\epsilon_x}{\epsilon_z}\ e^{ik_\rho\rho\cos(\phi-\theta)+ik_z(z+d)} \tag{A.104}$$

where $k_2 = \sqrt{\epsilon_x} k_o$. Upon integrating over angle ϕ we will also obtain the simpler 1-d integral result

$$G_{xx}(\mathbf{r}) = \frac{i}{8\pi k_1 k_2} \int dk_\rho \frac{k_\rho}{k_z} e^{ik_z(z+d)} \left[t_{ss} k_1 k_2 J_+^c - k_1 k_z^p J_2^s t_{ps} - k_2 k_z J_2^s t_{sp} + k_z k_z^p J_-^c t_{pp} \right] \tag{A.105}$$

$$G_{xy}(\mathbf{r}) = \frac{i}{8\pi k_1 k_2} \int dk_\rho \frac{k_\rho}{k_z} e^{ik_z(z+d)} \left[k_1 k_2 J_2^s t_{ss} + k_1 k_z^p J_-^c t_{ps} + k_2 k_z J_+^c t_{sp} + k_z k_z^p J_2^s t_{pp} \right] \tag{A.106}$$

$$G_{xz}(\mathbf{r}) = \frac{i}{8\pi k_1 k_2} \int dk_\rho \frac{k_\rho}{k_z} e^{ik_z(z+d)} \left[-2ik_2 k_\rho J_1^s t_{sp} + 2ik_\rho k_z^p J_1^c t_{pp} \right] \tag{A.107}$$

$$G_{yx}(\mathbf{r}) = \frac{i}{8\pi k_1 k_2} \int dk_\rho \frac{k_\rho}{k_z} e^{ik_z(z+d)} \left[k_1 k_2 J_2^s t_{ss} - k_1 k_z^p J_+^c t_{ps} + k_2 k_z J_-^c t_{sp} + k_z k_z^p J_2^s t_{pp} \right] \tag{A.108}$$

$$G_{yy}(\mathbf{r}) = \frac{i}{8\pi k_1 k_2} \int dk_\rho \frac{k_\rho}{k_z} e^{ik_z(z+d)} \left[k_1 k_2 J_-^c t_{ss} - k_1 k_z^p J_2^s t_{ps} - k_2 k_z J_2^s t_{sp} + k_z k_z^p J_+^c t_{pp} \right] \tag{A.109}$$

$$G_{yz}(\mathbf{r}) = \frac{i}{8\pi k_1 k_2} \int dk_\rho \frac{k_\rho}{k_z} e^{ik_z(z+d)} \left[2ik_2 k_\rho J_1^c t_{sp} + 2ik_\rho k_z^p J_1^s t_{pp} \right] \tag{A.110}$$

$$G_{zx}(\mathbf{r}) = \frac{i}{8\pi k_1 k_2} \int dk_\rho \frac{k_\rho}{k_z} e^{ik_z(z+d)} \left[-2ik_1 k_\rho J_1^s t_{ps} \frac{\epsilon_x}{\epsilon_z} + 2ik_\rho k_z J_1^c t_{pp} \frac{\epsilon_x}{\epsilon_z} \right] \tag{A.111}$$

$$G_{zy}(\mathbf{r}) = \frac{i}{8\pi k_1 k_2} \int dk_\rho \frac{k_\rho}{k_z} e^{ik_z(z+d)} \left[+2ik_1 k_\rho J_1^c t_{ps} \frac{\epsilon_x}{\epsilon_z} + 2ik_\rho k_z J_1^s t_{pp} \frac{\epsilon_x}{\epsilon_z} \right] \tag{A.112}$$

$$G_{zz}(\mathbf{r}) = \frac{i}{8\pi k_1 k_2} \int dk_\rho \frac{k_\rho}{k_z} e^{ik_z(z+d)} \left[2k_\rho^2 J_o t_{pp} \frac{\epsilon_x}{\epsilon_z} \right] \tag{A.113}$$

A.1.4 Transmitted DGF in uniaxial half-space ($\mathbf{c} = \mathbf{x}$)

We will now consider the case where the optic axis of the uniaxial medium lies parallel to the interface $\mathbf{c} = \mathbf{x}$.

$$\begin{aligned} \mathbf{G}_t(\mathbf{r}) = \frac{i}{8\pi^2} \int dk_x dk_y \frac{e^{i\mathbf{k}_\rho \cdot \rho + ik_{z1}d}}{k_{z1}} [& [t_{pp}(\mathbf{e}_e^- \otimes \mathbf{p}_-) + t_{ps}(\mathbf{e}_e^- \otimes \mathbf{s})] e^{k_{ze}z} \\ & + [t_{sp}(\mathbf{e}_o \otimes \mathbf{p}_-) + t_{ss}(\mathbf{e}_o \otimes \mathbf{s})] e^{k_{zo}z}] \end{aligned} \tag{A.114}$$

where

$$\mathbf{e}_o^- = \frac{1}{\sqrt{k_{zo}^2 + k_y^2}} \begin{pmatrix} 0 \\ -k_{zo} \\ -k_y \end{pmatrix}, \quad \mathbf{e}_e^- = \frac{1}{\sqrt{\epsilon_z} k_o \sqrt{k_{ze}^2 + k_y^2}} \begin{pmatrix} -(k_{ze}^2 + k_y^2)\frac{\epsilon_z}{\epsilon_x} \\ k_y k_x \\ -k_x k_{ze} \end{pmatrix} \tag{A.115}$$

The dyadic terms can be written explicitly as before

$$\mathbf{e}_o^- \mathbf{s} = \frac{1}{k_\rho \sqrt{(k_{zo}^2 + k_y^2)}} \begin{pmatrix} 0 & 0 & 0 \\ -k_y k_{zo} & k_x k_{zo} & 0 \\ -k_y^2 & k_x k_y & 0 \end{pmatrix} \tag{A.116}$$

$$\mathbf{e}_o^- \mathbf{p}_- = \frac{1}{k_1 k_\rho \sqrt{(k_{zo}^2 + k_y^2)}} \begin{pmatrix} 0 & 0 & 0 \\ k_x k_{z1} k_{zo} & k_y k_{z1} k_{zo} & k_{zo} k_\rho^2 \\ k_x k_y k_{z1} & k_y^2 k_{z1} & k_y k_\rho^2 \end{pmatrix} \tag{A.117}$$

$$\mathbf{e}_e^- \mathbf{s} = \frac{1}{\sqrt{\epsilon_z} k_o k_\rho \sqrt{(k_{ze}^2 + k_y^2)}} \begin{pmatrix} -k_y(k_{ze}^2 + k_y^2)\frac{\epsilon_z}{\epsilon_x} & k_x(k_{ze}^2 + k_y^2)\frac{\epsilon_z}{\epsilon_x} & 0 \\ -k_x k_y^2 & k_x^2 k_y & 0 \\ -k_x k_y k_{ze} & k_x^2 k_{ze} & 0 \end{pmatrix} \tag{A.118}$$

$$\mathbf{e}_e^- \mathbf{p}_- = \frac{1}{\sqrt{\epsilon_z} k_o k_1 k_\rho \sqrt{(k_{ze}^2 + k_y^2)}} \begin{pmatrix} k_x k_{z1}(k_{ze}^2 + k_y^2)\frac{\epsilon_z}{\epsilon_x} & k_y k_{z1}(k_{ze}^2 + k_y^2)\frac{\epsilon_z}{\epsilon_x} & k_\rho^2(k_{ze}^2 + k_y^2)\frac{\epsilon_z}{\epsilon_x} \\ k_x^2 k_y k_{z1} & k_x k_y^2 k_{z1} & k_\rho^2 k_x k_y \\ k_x^2 k_{z1} k_{ze} & k_x k_y k_{z1} k_{ze} & k_x k_\rho^2 k_{ze} \end{pmatrix} \tag{A.119}$$

The full Green function can then be written as

$$\begin{aligned} G_{xx}(\mathbf{r}) = \frac{i}{8\pi^2 k_1 k_2} \int dk_\rho d\phi \, \frac{1}{k_z} [& -t_{21} k_1 k_y \sqrt{k_{ze}^2 + k_y^2} \frac{\epsilon_z}{\epsilon_x} \\ & + t_{22} k_x k_{z1} \sqrt{k_{ze}^2 + k_y^2} \frac{\epsilon_z}{\epsilon_x}] e^{ik_\rho \rho \cos(\phi - \theta) + ik_z(z+d)} \end{aligned} \tag{A.120}$$

$$G_{zz}(\mathbf{r}) = \frac{i}{8\pi^2 k_1 k_2} \int dk_\rho d\phi \, \frac{k_\rho^2}{k_z} \left[t_{12} k_2 k_y e^{-ik_{zo} z} + t_{22} k_x k_{ze} e^{-ik_{ze} z} \right] e^{ik_\rho \rho \cos(\phi - \theta) + ik_z d} \tag{A.121}$$

where

$$t_{11} = -\frac{2k_{z1}k_xk_o}{\sqrt{\epsilon_z}\Delta}\frac{\epsilon_1 k_{zo}^2 + \epsilon_z k_{z1}k_{ze}}{\sqrt{(k_x^2+k_y^2)(k_{ze}^2+k_y^2)}} \tag{A.122}$$

$$t_{12} = \pm\frac{2k_{z1}k_yk_o^2}{\Delta}\frac{(k_{z1}+k_{ze})\sqrt{\epsilon_1\epsilon_z}}{\sqrt{(k_x^2+k_y^2)(k_{ze}^2+k_y^2)}} \tag{A.123}$$

$$t_{21} = \mp\frac{2k_{z1}k_yk_o^2}{\Delta}\frac{\epsilon_1 k_{zo} + \epsilon_z k_{z1}}{\sqrt{(k_x^2+k_y^2)(k_y^2+k_{zo}^2)}} \tag{A.124}$$

$$t_{22} = -\frac{2k_{z1}k_{zo}k_1k_x}{\Delta}\frac{k_{z1}+k_{zo}}{\sqrt{(k_x^2+k_y^2)(k_y^2+k_{zo}^2)}} \tag{A.125}$$

and

$$\Delta = \pm\frac{k_x^2k_{zo}k_o(k_{z1}+k_{zo})(\epsilon_1k_{zo}^2+\epsilon_zk_{z1}k_{ze}) + \epsilon_zk_y^2k_o^3(k_{z1}+k_{ze})(\epsilon_1k_{zo}+\epsilon_zk_{z1})}{\sqrt{\epsilon_z}(k_x^2+k_y^2)\sqrt{k_{zo}^2+k_y^2}\sqrt{k_{ze}^2+k_y^2}} \tag{A.126}$$

A.2 Green function inside a uniaxial medium.

Finally, we provide the Green tensor as the unique solution to the homogeneous Helmholtz equation with permittivity tensor $\boldsymbol{\epsilon}(\omega)$,

$$\nabla\times\nabla\times\mathbf{G}(\mathbf{r},\mathbf{r}';\omega) - \boldsymbol{\epsilon}(\omega)\frac{\omega^2}{c^2}\mathbf{G}(\mathbf{r},\mathbf{r}';\omega) = \mathbf{I}\delta(\mathbf{r}-\mathbf{r}'), \tag{A.127}$$

and radiation condition $\mathbf{G}(\mathbf{r},\mathbf{r}';\omega) = 0$ for $|\mathbf{r}-\mathbf{r}'|\to\infty$. The coordinate-free form of the Green function is given by [163]

$$\begin{aligned}\mathbf{G}(\mathbf{r},\mathbf{r}';\omega) = \frac{1}{4\pi\sqrt{\epsilon_x}}\Bigg\{&\frac{e^{ik_or_e}}{r_e}\Bigg[\left(\frac{k_o^2r_e^2+ik_or_e-1}{k_o^2r_e^2}\right)\epsilon_x\epsilon_z\boldsymbol{\epsilon}^{-1}\\ &-\left(\frac{k_o^2r_e^2+3ik_or_e-3}{k_o^2r_e^2}\right)\frac{\epsilon_x^2\epsilon_z^2(\boldsymbol{\epsilon}^{-1}\cdot\mathbf{r})(\boldsymbol{\epsilon}^{-1}\cdot\mathbf{r})}{r_e^2}\\ &+\left(\frac{\epsilon_xe^{ik_or_o}}{r_o}-\frac{\epsilon_ze^{ik_or_e}}{r_e}\right)\frac{(\mathbf{r}\times\hat{\mathbf{c}})(\mathbf{r}\times\hat{\mathbf{c}})}{(\mathbf{r}\times\hat{\mathbf{c}})^2}\\ &+\frac{e^{ik_or_o}-e^{ik_or_e}}{ik_o(\mathbf{r}\times\hat{\mathbf{c}})^2}\left[\mathbf{I}-\hat{\mathbf{c}}\hat{\mathbf{c}}-2\frac{(\mathbf{r}\times\hat{\mathbf{c}})(\mathbf{r}\times\hat{\mathbf{c}})}{(\mathbf{r}\times\hat{\mathbf{c}})^2}\right]\Bigg\}\end{aligned} \tag{A.128}$$

where we have fixed the spatial coordinate of the source at the origin, i.e. $\mathbf{r}' = 0$. Note that this Green function is only applicable when $\mathbf{r}\neq\mathbf{r}'$, since we have excluded the singularity term that occurs when $\mathbf{r}=\mathbf{r}'$.

es

B. APPENDIX: FUNDAMENTAL EFFICIENCY BOUND FOR COHERENT ENERGY TRANSFER

Appendix B is directly related to the Chapter 6. It is divided into four sections. Section 1 presents the quantum electrodynamic (QED) theory of two non-identical neutral atoms in arbitrary Markovian nanophotonic environments. Section 2 derives the non-stationary energy transfer efficiency between two atoms. Section 3 provides an analytical expression for the time-dependent concurrence of the two-atom system. We use this result to measure both entanglement and quantum coherence for the two-atom quantum transport problem. Finally, section 4 provides the full Green function expression used to describe the two-atom interaction above a mirror and in free-space.

B.1 Quantum electrodynamic theory of energy transfer

We use a quantum electrodynamic (QED) theory to describe the interaction between two neutral atoms in an arbitrary nanophotonic environment. In the dipole approximation, the multipolar Hamiltonian is composed of three components, $H = H_s + H_b + H_{int}$, where

$$H_s = \sum_{n=g,e} \hbar\omega_{n,d} \left|n_d\right\rangle\!\left\langle n_d\right| + \sum_{n=g,e} \hbar\omega_{n,a} \left|n_a\right\rangle\!\left\langle n_a\right|, \tag{B.1}$$

$$H_b = \int d^3\mathbf{r} \int_0^\infty d\omega\, \hbar\omega\, \hat{\mathbf{f}}^\dagger(\mathbf{r},\omega)\hat{\mathbf{f}}(\mathbf{r},\omega), \tag{B.2}$$

$$H_{int} = -\hat{\mathbf{d}}_d \cdot \hat{\mathbf{E}}(\mathbf{r}_d) - \hat{\mathbf{d}}_a \cdot \hat{\mathbf{E}}(\mathbf{r}_a), \tag{B.3}$$

describes the two-atom system, the electrodynamic bath, and the electric-dipole interaction between each atom's electric dipole moment $\hat{\mathbf{d}}_k$ and the electrodynamic field respectively, $k = \{d, a\}$. We assume each atom only has two electronic energy levels while also ignoring multipolar and spin contributions. This Hamiltonian

has been derived previously by several authors and forms the basis of an *effective-field/macroscopic* quantum electrodynamic theory valid in arbitrary dissipative media satisfying Kramers-Kronig causality relations [41,42]. Here, $\hat{\mathbf{f}}^{\dagger}(\mathbf{r},\omega)/\hat{\mathbf{f}}(\mathbf{r},\omega)$ represent the creation/annihilation operators of the elementary excitations of matter. In vacuum, $\hat{\mathbf{f}}^{\dagger}(\mathbf{r},\omega)$ describes the creation of a *photon*. In macroscopic matter, it describes the creation of a *polariton*. These operators satisfy

$$\hat{\mathbf{f}}(\mathbf{r},\omega)\,|\{0\}\rangle = 0$$
$$\hat{\mathbf{f}}^{\dagger}(\mathbf{r},\omega)\,|\{0\}\rangle = |\mathbf{1}(\mathbf{r},\omega)\rangle$$

as well as

$$[\hat{\mathbf{f}}(\mathbf{r},\omega),\hat{\mathbf{f}}^{\dagger}(\mathbf{r}',\omega')] = \boldsymbol{\delta}(\mathbf{r}-\mathbf{r}')\delta(\omega-\omega')$$
$$[\hat{\mathbf{f}}(\mathbf{r},\omega),\hat{\mathbf{f}}(\mathbf{r}',\omega')] = 0$$

In dissipative quantum electrodynamics, the electric field is defined as

$$\hat{\mathbf{E}}(\mathbf{r},\omega) = i\sqrt{\frac{\hbar\omega^4}{\pi\epsilon_o c^4}}\int d^3\mathbf{r}'\sqrt{\epsilon''(\mathbf{r}',\omega)}\mathbf{G}(\mathbf{r},\mathbf{r}',\omega)\hat{\mathbf{f}}(\mathbf{r}',\omega). \tag{B.4}$$

The electric field is decomposed in terms of positive-frequency and negative-frequency components, $\hat{\mathbf{E}}(\mathbf{r}) = \hat{\mathbf{E}}^{(+)}(\mathbf{r})+\hat{\mathbf{E}}^{(-)}(\mathbf{r})$, where $\hat{\mathbf{E}}^{(+)}(\mathbf{r}) = \int_0^{\infty} d\omega\,\hat{\mathbf{E}}(\mathbf{r},\omega)$ and $[\hat{\mathbf{E}}^{(-)}(\mathbf{r})]^{\dagger} = \hat{\mathbf{E}}^{(+)}(\mathbf{r})$ due to reality conditions for the electrodynamic field. In the following, we derive a quantum master equation describing the atom-atom dynamics arising from the Hamiltonian (1). While such a master equation has been derived before, it is worth re-visiting the derivation to account for inconsistencies with different models in the self-energy (Lamb shift and spontaneous emission) and dipole-dipole interaction terms. Here, we derive the atom-atom dynamics without using the rotating-wave

approximation. To obtain a closed-form solution, we truncate the Hilbert space to the following states,

$$|d\rangle \equiv |e_d, g_a, \{0\}\rangle\,, \tag{B.5}$$

$$|a\rangle \equiv |g_d, e_a, \{0\}\rangle\,, \tag{B.6}$$

$$|g\rangle \equiv |g_d, g_a, \mathbf{1}(\mathbf{r},\omega)\rangle\,, \tag{B.7}$$

$$|e\rangle \equiv |e_d, e_a, \mathbf{1}(\mathbf{r},\omega)\rangle\,, \tag{B.8}$$

corresponding to an excited-state donor with acceptor and field in the ground-state, an excited-state acceptor with donor and field in ground-state, a single-excitation in the field with both atoms in the ground state, and finally a single field excitation with both atoms in the excited-state. Due to truncation of the Hilbert space, this approach is not fully non-perturbative and will fail to describe higher-order multi-photon effects that occur in the ultra-strong coupling regime. As we show below, this approach to derive the atom-atom dynamics provides a first-order correction to the dipole-dipole interaction (B.31) that is markedly different from the dipole-dipole frequency shift derived through the rotating wave approximation. In the truncated Hilbert space, the temporal evolution of the system is captured by the total wavefunction

$$|\psi(t)\rangle = d(t)\,|d\rangle + a(t)\,|a\rangle + \int d^3\mathbf{r} \int d\omega\, g(\mathbf{r},\omega,t)\,|g\rangle + \int d^3\mathbf{r} \int d\omega\, e(\mathbf{r},\omega,t)\,|e\rangle \tag{B.9}$$

Using the Schrodinger equation, $i\hbar\frac{\partial}{\partial t}|\psi(t)\rangle = H\,|\psi(t)\rangle$, we obtain the dynamical equations for the probability amplitudes,

$$i\hbar\frac{\partial d}{\partial t} = \hbar(\omega_{g,a} + \omega_{e,d})d(t) + \int d^3\mathbf{r} \int d\omega\ [g(\mathbf{r},\omega,t)V_{dg} + e(\mathbf{r},\omega,t)V_{de}] \tag{B.10}$$

$$i\hbar\frac{\partial a}{\partial t} = \hbar(\omega_{g,d} + \omega_{e,a})a(t) + \int d^3\mathbf{r} \int d\omega\ [g(\mathbf{r},\omega,t)V_{ag} + e(\mathbf{r},\omega,t)V_{ae}] \tag{B.11}$$

$$i\hbar\frac{\partial g}{\partial t} = \hbar(\omega_{g,a} + \omega_{g,d} + \omega')g(\mathbf{r}',\omega',t) + V_{gd}d(t) + V_{ga}a(t) \tag{B.12}$$

$$i\hbar\frac{\partial e}{\partial t} = \hbar(\omega_{e,a} + \omega_{e,d} + \omega')e(\mathbf{r}',\omega',t) + V_{ed}d(t) + V_{ea}a(t) \tag{B.13}$$

where we define $V_{kn} = \langle k|H_{int}|n(\mathbf{r},\omega)\rangle$ as the interaction coupling coefficient with $k = \{a, d\}$ and $n = \{g, e\}$. In the interaction picture, $d(t) = \tilde{d}(t)e^{-i(\omega_{g,a}+\omega_{e,d})t}$, $a(t) = \tilde{a}(t)e^{-i(\omega_{g,d}+\omega_{e,a})t}$, $g(t) = \tilde{g}(t)e^{-i(\omega_{g,a}+\omega_{g,d}+\omega)t}$ and $e(t) = \tilde{e}(t)e^{-i(\omega_{e,a}+\omega_{e,d}+\omega)t}$, we obtain

$$i\hbar\frac{\partial\tilde{d}}{\partial t} = \int d^3\mathbf{r}\int d\omega\ \left[V_{dg}\tilde{g}(t)e^{-i(\omega-\omega_d)t} + V_{de}\tilde{e}(t)e^{-i(\omega+\omega_a)t}\right] \tag{B.14}$$

$$i\hbar\frac{\partial\tilde{a}}{\partial t} = \int d^3\mathbf{r}\int d\omega\ \left[V_{ag}\tilde{g}(t)e^{-i(\omega-\omega_a)t} + V_{ae}\tilde{e}(t)e^{-i(\omega+\omega_d)t}\right] \tag{B.15}$$

$$i\hbar\frac{\partial\tilde{g}}{\partial t} = V_{gd}\tilde{d}(t)e^{-i(\omega_d-\omega)t} + V_{ga}\tilde{a}(t)e^{-i(\omega_a-\omega)t} \tag{B.16}$$

$$i\hbar\frac{\partial\tilde{e}}{\partial t} = V_{ed}\tilde{d}(t)e^{+i(\omega_a+\omega)t} + V_{ea}\tilde{a}(t)e^{+i(\omega_d+\omega)t} \tag{B.17}$$

where $\omega_k = \omega_{e,k} - \omega_{g,k}$. The formal solutions to the third and fourth equations are

$$i\hbar(\tilde{g}(t) - \tilde{g}(0)) = \int_0^t dt'\left(V_{gd}\tilde{d}(t')e^{-i(\omega_d-\omega)t'} + V_{ga}\tilde{a}(t')e^{-i(\omega_a-\omega)t'}\right) \tag{B.18}$$

$$i\hbar(\tilde{e}(t) - \tilde{e}(0)) = \int_0^t dt'\left(V_{ed}\tilde{d}(t')e^{+i(\omega_a+\omega)t'} + V_{ea}\tilde{a}(t')e^{+i(\omega_d+\omega)t'}\right). \tag{B.19}$$

Assuming the donor is initially excited, $g(t=0) = 0$ and $e(t=0) = 0$, we obtain the coupled integro-differential equations through substitution of (18)-(19) into (14)-(15),

$$\begin{aligned}\frac{\partial\tilde{d}}{\partial t} = -\frac{1}{\hbar^2}\int d^3\mathbf{r}\int d\omega\ \int_0^t dt'\Big(&V_{dg}V_{gd}\tilde{d}(t')e^{-i(\omega-\omega_d)(t-t')} + V_{dg}V_{ga}\tilde{a}(t')e^{-i(\omega-\omega_d)t-i(\omega_a-\omega)t'}\\ &+ V_{de}V_{ed}\tilde{d}e^{-i(\omega_a+\omega)(t-t')} + V_{de}V_{ea}\tilde{a}e^{-i(\omega_a+\omega)t}e^{i(\omega_d+\omega)t'}\Big)\\ \frac{\partial\tilde{a}}{\partial t} = -\frac{1}{\hbar^2}\int d^3\mathbf{r}\int d\omega\ \int_0^t dt'\Big(&V_{ag}V_{gd}\tilde{d}(t')e^{-i(\omega-\omega_a)t-i(\omega_d-\omega)t'} + V_{ag}V_{ga}\tilde{a}(t')e^{-i(\omega-\omega_a)(t-t')}\\ &+ V_{ae}V_{ed}\tilde{d}e^{-i(\omega+\omega_d)t}e^{i(\omega+\omega_a)t'} + V_{ae}V_{ea}\tilde{a}e^{-i(\omega+\omega_d)(t-t')}\Big).\end{aligned}$$

Using the properties we defined above for the creation and annihilation operators, we find

$$\begin{aligned}
\frac{\partial \tilde{d}}{\partial t} = -\frac{1}{\hbar^2}\int_0^t dt' \int d^3\mathbf{r} \int d\omega\, \frac{\hbar\omega^4}{\pi\epsilon_o c^4}\epsilon''(\mathbf{r},\omega)\Big(&\mathbf{d}_{eg}^{d}\cdot\mathbf{G}(\mathbf{r}_d,\mathbf{r},\omega)\mathbf{G}^{\dagger}(\mathbf{r}_d,\mathbf{r},\omega)\cdot\mathbf{d}_{eg}^{*d}\;\tilde{d}(t')e^{-i(\omega-\omega_d)(t-t')}\\
&+\mathbf{d}_{eg}^{d}\cdot\mathbf{G}(\mathbf{r}_d,\mathbf{r},\omega)\mathbf{G}^{\dagger}(\mathbf{r}_a,\mathbf{r},\omega)\cdot\mathbf{d}_{eg}^{*a}\;\tilde{a}(t')e^{-i(\omega-\omega_d)t-i(\omega_a-\omega)t'}\\
&+\mathbf{d}_{ge}^{a}\cdot\mathbf{G}(\mathbf{r}_a,\mathbf{r})\mathbf{G}^{\dagger}(\mathbf{r}_a,\mathbf{r})\cdot\mathbf{d}_{ge}^{a*}\tilde{d}(t')e^{-i(\omega_a+\omega)(t-t')}\\
&+\mathbf{d}_{ge}^{a}\cdot\mathbf{G}(\mathbf{r}_a,\mathbf{r})\mathbf{G}^{\dagger}(\mathbf{r}_d,\mathbf{r})\cdot\mathbf{d}_{ge}^{d*}\tilde{a}(t')e^{-i(\omega_a+\omega)t}e^{i(\omega_d+\omega)t'}\Big)\\
\frac{\partial \tilde{a}}{\partial t} = -\frac{1}{\hbar^2}\int_0^t dt' \int d^3\mathbf{r} \int d\omega\, \frac{\hbar\omega^4}{\pi\epsilon_o c^4}\epsilon''(\mathbf{r},\omega)\Big(&\mathbf{d}_{eg}^{a}\cdot\mathbf{G}(\mathbf{r}_a,\mathbf{r},\omega)\mathbf{G}^{\dagger}(\mathbf{r}_d,\mathbf{r},\omega)\cdot\mathbf{d}_{eg}^{*d}\;\tilde{d}(t')e^{-i(\omega-\omega_a)t-i(\omega_d-\omega)t'}\\
&+\mathbf{d}_{eg}^{a}\cdot\mathbf{G}(\mathbf{r}_a,\mathbf{r},\omega)\mathbf{G}^{\dagger}(\mathbf{r}_a,\mathbf{r},\omega)\cdot\mathbf{d}_{eg}^{*a}\;\tilde{a}(t')e^{-i(\omega-\omega_a)(t-t')}\\
&+\mathbf{d}_{ge}^{d}\cdot\mathbf{G}(\mathbf{r}_d,\mathbf{r})\mathbf{G}^{\dagger}(\mathbf{r}_a,\mathbf{r})\cdot\mathbf{d}_{ge}^{a*}\tilde{d}(t')e^{-i(\omega+\omega_d)t}e^{i(\omega+\omega_a)t'}\\
&+\mathbf{d}_{ge}^{d}\cdot\mathbf{G}(\mathbf{r}_d,\mathbf{r})\mathbf{G}^{\dagger}(\mathbf{r}_d,\mathbf{r})\cdot\mathbf{d}_{ge}^{d*}\tilde{a}(t')e^{-i(\omega+\omega_d)(t-t')}\Big).
\end{aligned}$$

We simplify the result using the relation [41],

$$\int d^3\mathbf{s}\,\frac{\omega^2}{c^2}\epsilon''(\mathbf{s},\omega)\mathbf{G}(\mathbf{r},\mathbf{s},\omega)\mathbf{G}^{*}(\mathbf{s},\mathbf{r}',\omega) = \mathrm{Im}\mathbf{G}(\mathbf{r},\mathbf{r}',\omega) \tag{B.20}$$

along with the reciprocity condition $\mathbf{G}^{T}(\mathbf{r},\mathbf{r}') = \mathbf{G}(\mathbf{r}',\mathbf{r})$, thereby obtaining the main result of this section. The temporal dynamics of two atoms are captured by the coupled integro-differential equations,

$$\frac{\partial \tilde{d}}{\partial t} = -\frac{1}{\hbar}\int_0^t dt' \left[K_{dd}(t,t')\tilde{d}(t') + K_{da}(t,t')\tilde{a}(t')\right] \tag{B.21}$$

$$\frac{\partial \tilde{a}}{\partial t} = -\frac{1}{\hbar}\int_0^t dt' \left[K_{ad}(t,t')\tilde{d}(t') + K_{aa}(t,t')\tilde{a}(t')\right]. \tag{B.22}$$

The memory Kernels are given by

$$K_{dd}(t,t') = \frac{1}{\hbar\pi\epsilon_o c^2}\int_0^\infty \left[\mathbf{d}_{eg}^d \mathrm{Im}\{\mathbf{G}_{dd}\}\mathbf{d}_{ge}^d e^{-i(\omega-\omega_d)(t-t')} + \mathbf{d}_{ge}^a \mathrm{Im}\{\mathbf{G}_{aa}\}\mathbf{d}_{eg}^a e^{-i(\omega+\omega_a)(t-t')}\right]\omega^2 d\omega$$

$$K_{da}(t,t') = \frac{1}{\hbar\pi\epsilon_o c^2}\int_0^\infty \Big[\mathbf{d}_{eg}^d \mathrm{Im}\{\mathbf{G}_{da}\}\mathbf{d}_{ge}^a e^{-i(\omega-\omega_d)t} e^{i(\omega-\omega_a)t'} \tag{B.23}$$

$$+ \mathbf{d}_{ge}^a \mathrm{Im}\{\mathbf{G}_{ad}\}\mathbf{d}_{eg}^d e^{-i(\omega_a+\omega)t} e^{i(\omega_d+\omega)t'}\Big]\omega^2 d\omega$$

$$K_{ad}(t,t') = \frac{1}{\hbar\pi\epsilon_o c^2}\int_0^\infty \Big[\mathbf{d}_{eg}^a \mathrm{Im}\{\mathbf{G}_{ad}\}\mathbf{d}_{ge}^d e^{-i(\omega-\omega_a)t} e^{i(\omega-\omega_d)t'} \tag{B.24}$$

$$+ \mathbf{d}_{ge}^d \mathrm{Im}\{\mathbf{G}_{da}\}\mathbf{d}_{eg}^a e^{-i(\omega_d+\omega)t} e^{i(\omega_a+\omega)t'}\Big]\omega^2 d\omega$$

$$K_{aa}(t,t') = \frac{1}{\hbar\pi\epsilon_o c^2}\int_0^\infty \left[\mathbf{d}_{eg}^a \mathrm{Im}\{\mathbf{G}_{aa}\}\mathbf{d}_{ge}^a e^{-i(\omega-\omega_a)(t-t')} + \mathbf{d}_{ge}^d \mathrm{Im}\{\mathbf{G}_{dd}\}\mathbf{d}_{eg}^d e^{-i(\omega+\omega_d)(t-t')}\right]\omega^2 d\omega \tag{B.25}$$

For simplicity, we used the notation, $\mathbf{G}_{kk'} = \mathbf{G}(\mathbf{r}_k, \mathbf{r}_{k'}; \omega)$. Solving this set of coupled integro-differential equations would provide the complete non-perturbative time dynamical description of two two-level atoms in arbitrary nanophotonic environments. A general analytical solution of this type is not possible to the best of our knowledge, though we will explore this notion in a subsequent paper. In the following, we provide the exact analytical response for the case of two atoms in a *Markovian* nanophotonic environment.

B.1.1 Markov approximation

A Markov process is a random process that is memoryless arising from a reservoir with an infinitely short correlation time and a flat spectral density. In the following, we assume the nanophotonic reservoir has a correlation time τ_c that is much shorter than the relaxation time of each atom. Generally, this is a valid assumption if the nanophotonic reservoir consists of intermediate-to-low quality factor ($Q = \omega/\kappa$) cavities with damping rates that are much larger than the dissipation rates of each atom, $\kappa \gg \gamma_a, \gamma_b$. The Markov approximation assumes the probability amplitudes, valid in the interaction picture only, are slowly varying compared to the bath's correlation

time. Evaluation of one of the dipole-dipole interaction time integrals is performed as follows:

$$\begin{aligned}\int_0^t e^{-i(\omega\pm\omega_d)t}e^{i(\omega\pm\omega_a)t'}\tilde{a}(t')\,dt' &= \int_0^t e^{-i(\omega\pm\omega_+)(t-t')}e^{\mp i\omega_-(t+t')}\tilde{a}(t')\,dt' \\ &\approx \tilde{a}(t)e^{\mp 2i\omega_- t}\int_0^\infty e^{-i(\omega\pm\omega_+)\tau}d\tau \\ &\approx \tilde{a}(t)e^{\mp 2i\omega_- t}\left[\pi\delta(\omega\pm\omega_+) - i\mathcal{P}\left(\frac{1}{\omega\pm\omega_+}\right)\right]\end{aligned}$$

where we defined $\omega_\pm = (\omega_d \pm \omega_a)/2$ and assumed $\omega_+ \gg \omega_-$ in the second line. All other time integrals of the memory kernels are evaluated using the same approach. In the following, we present the self-energy and dipole-dipole interaction terms that arise from the time-integrated memory kernels under the Markov approximation.

B.1.2 Self-energy and dipole-dipole interaction

The first terms in the memory Kernels $K_{dd}(t,t')$ and $K_{aa}(t,t')$ respectively give rise to an excited-state self-energy correction, $\Sigma_{e,k} = \hbar(-\delta\omega_{e,k} + i\gamma_k/2)$,

$$\delta\omega_{e,k} = \frac{\mathcal{P}}{\hbar\epsilon_o\pi}\int_0^\infty d\omega\,\frac{\omega^2}{c^2}\frac{\mathbf{d}_{eg}^k\cdot\mathrm{Im}\mathbf{G}(\mathbf{r}_k,\mathbf{r}_k,\omega)\cdot\mathbf{d}_{ge}^k}{\omega_k-\omega} \quad \text{and} \quad \gamma_k = \frac{2\omega_k^2}{\hbar\epsilon_o c^2}\mathbf{d}_{eg}^k\cdot\mathrm{Im}\mathbf{G}(\mathbf{r}_k,\mathbf{r}_k,\omega_k)\cdot\mathbf{d}_{ge}^k \tag{B.26}$$

corresponding to a frequency shift and a decay rate for the excited energy level of each atom. $\mathcal{P}$ denotes the principal value. As shown in [41], it is convenient to evaluate the principal value integral using contour integration techniques. Using a quarter-circle contour along the upper right-half of the complex ω plane, the principal value integral is decomposed into off-resonant and resonant contributions, $\delta\omega_{e,k} = \delta\omega_{e,k}^{nres} + \delta\omega_{e,k}^{res}$, given by

$$\delta\omega_{e,k}^{nres} = \frac{-1}{\hbar\epsilon_o\pi c^2}\int_0^\infty d\eta\,\eta^2\frac{\omega_k}{\omega_k^2+\eta^2}\mathbf{d}_{eg}^k\cdot\mathrm{Im}\mathbf{G}(\mathbf{r}_k,\mathbf{r}_k;i\eta)\cdot\mathbf{d}_{ge}^k \tag{B.27}$$

and

$$\delta\omega_{e,k}^{res} = -\frac{\omega_k^2}{\hbar\epsilon_o c^2}\mathbf{d}_{eg}^k\cdot\mathrm{Re}\mathbf{G}(\mathbf{r}_k,\mathbf{r}_k;\omega_k)\cdot\mathbf{d}_{ge}^k.$$

The resonant contribution is much more sensitive to nanophotonic environments because it is directly proportional to the Green function evaluated at the transition

frequency of the atom. For the rest of the appendix, we will assume the off-resonant contribution is accounted for in the definition of the excited-state frequency $\omega_{e,k}$. Proceeding with the calculation, the second terms of the memory Kernels $K_{dd}(t,t')$ and $K_{aa}(t,t')$ respectively give rise to the ground-state self-energy

$$\delta\omega_{g,k} = -\frac{\mathcal{P}}{\hbar\epsilon_o\pi}\int_0^\infty d\omega\,\frac{\omega^2}{c^2}\frac{\mathbf{d}_{ge}^k\cdot\mathrm{Im}\mathbf{G}(\mathbf{r}_k,\mathbf{r}_k,\omega)\cdot\mathbf{d}_{eg}^k}{\omega_k+\omega}. \tag{B.28}$$

composed of a frequency (Lamb) shift only. The denominator does not have a pole, therefore the frequency shift is only composed of an off-resonant contribution. In vacuum, this quantity is divergent within the dipole approximation. Special regularization and renormalization techniques are required to properly deal with this divergence. As is normally done in quantum optics, the rest of the calculation will proceed assuming the Lamb shift is accounted for in the definition of the ground-state frequency. Focusing on the memory kernel, $K_{da}(t,t')$, we find the dipole-dipole interaction gives rise to the dissipative rate,

$$\gamma_{kk'} = \frac{2\omega_+^2}{\hbar\epsilon_o c^2}\mathbf{d}_{eg}^k\cdot\mathrm{Im}\mathbf{G}(\mathbf{r}_k,\mathbf{r}_{k'},\omega_+)\cdot\mathbf{d}_{ge}^{k'}, \tag{B.29}$$

also known as the cooperative decay rate. The dipole-dipole frequency shift is

$$\begin{aligned}
\delta\omega_{kk'} &= \frac{\mathcal{P}}{\hbar\epsilon_o\pi}\int_0^\infty d\omega\,\frac{\omega^2}{c^2}\left[\frac{\mathbf{d}_{eg}^k\cdot\mathrm{Im}\mathbf{G}(\mathbf{r}_k,\mathbf{r}_{k'},\omega)\cdot\mathbf{d}_{ge}^{k'}}{\omega_+-\omega} - \frac{\mathbf{d}_{ge}^{k'}\cdot\mathrm{Im}\mathbf{G}(\mathbf{r}_{k'},\mathbf{r}_k,\omega)\cdot\mathbf{d}_{eg}^k}{\omega_++\omega}\right]\\
&= \frac{\mathcal{P}}{\hbar\epsilon_o\pi}\int_0^\infty d\omega\,\frac{\omega^2}{c^2}\left[\frac{\mathbf{d}_{eg}^k\cdot\mathrm{Im}\mathbf{G}(\mathbf{r}_k,\mathbf{r}_{k'},\omega)\cdot\mathbf{d}_{ge}^{k'}}{\omega_+-\omega} - \frac{\mathbf{d}_{eg}^k\cdot\mathrm{Im}\mathbf{G}(\mathbf{r}_k,\mathbf{r}_{k'},\omega)\cdot\mathbf{d}_{ge}^{k'}}{\omega_++\omega}\right]\\
&= \frac{\mathcal{P}}{\hbar\epsilon_o\pi}\int_{-\infty}^\infty d\omega\,\frac{\omega^2}{c^2}\left[\frac{\mathbf{d}_{eg}^k\cdot\mathrm{Im}\mathbf{G}(\mathbf{r}_k,\mathbf{r}_{k'},\omega)\cdot\mathbf{d}_{ge}^{k'}}{\omega_+-\omega}\right]
\end{aligned} \tag{B.30}$$

In the second line, we used the Onsager reciprocity condition, $\mathbf{G}^T(\mathbf{r},\mathbf{r}') = \mathbf{G}(\mathbf{r}',\mathbf{r})$, while the third line used the condition, $\mathbf{G}^*(\omega) = \mathbf{G}(-\omega)$. Using countour integration techniques, one may show that the principal value integral is exactly equal to

$$J_{kk'} \equiv \delta\omega_{kk'} = -\frac{\omega_+^2}{\hbar\epsilon_o c^2}\mathbf{d}_{eg}^k\cdot\mathrm{Re}\mathbf{G}(\mathbf{r}_k,\mathbf{r}_{k'},\omega_+)\cdot\mathbf{d}_{ge}^{k'}. \tag{B.31}$$

As alluded to earlier, this is the reason we chose to work within the Hilbert subspace (5)-(8). The cooperative frequency shift $\delta\omega_{kk'}$ (otherwise known as the dipole-dipole potential $J_{kk'}$) does *not* contain an off-resonant component. This is a subtle

yet important distinction arising from the counter-rotating wave terms. This result does not agree with previous results which calculated the dipole-dipole interaction using the rotating-wave approximation, cf. [164]. On the other hand, this result does agree with rigorous quantum electrodynamic calculations using perturbation theory for intermolecular energy transfer [86,127]. The dipole-dipole potential $J_{kk'}$, combined with the cooperative decay rate $\gamma_{kk'}$, is often referred to as the resonant dipole-dipole interaction (RDDI)

$$V_{kk'} = \hbar(-J_{kk'} + i\gamma_{kk'}/2) = \frac{\omega_+^2}{\epsilon_o c^2}\mathbf{d}_{eg}^k \cdot \mathbf{G}(\mathbf{r}_k, \mathbf{r}_{k'}, \omega_+) \cdot \mathbf{d}_{ge}^{k'}. \tag{B.32}$$

Combining these results, we obtain the following set of coupled differential equations for the probability amplitudes in the Schrodinger picture,

$$i\hbar\frac{\partial d}{\partial t} = -\left[\tilde{\Sigma}_{e,d} + \tilde{\Sigma}_{g,a}\right] d(t) - V_{da}a(t) \tag{B.33}$$

$$i\hbar\frac{\partial a}{\partial t} = -V_{ad}d(t) - \left[\tilde{\Sigma}_{g,d} + \tilde{\Sigma}_{e,a}\right] a(t). \tag{B.34}$$

We have written everything in terms of the modified excited-state self-energy, $\tilde{\Sigma}_{e,k} = -\hbar\omega_{e,k} + \Sigma_{e,k}$, the modified ground-state self-energy $\tilde{\Sigma}_{g,k} = -\hbar\omega_{g,k} + \Sigma_{g,k}$, as well as the resonant dipole-dipole interaction. These coupled differential equations form the main result of this sub-section.

B.2 RDDI quantum master equation

Using (B.33)-(B.34), we find the following set of coupled differential equations for the probability densities and coherences,

$$\frac{\partial}{\partial t}|d|^2 = \frac{2}{\hbar}\mathrm{Re}\left[i(\tilde{\Sigma}_{e,d} + \tilde{\Sigma}_{g,a})|d|^2 + iV_{da}ad^*\right] \tag{B.35}$$

$$\frac{\partial}{\partial t}|a|^2 = \frac{2}{\hbar}\mathrm{Re}\left[iV_{ad}da^* + i(\tilde{\Sigma}_{g,d} + \tilde{\Sigma}_{e,a})|a|^2\right] \tag{B.36}$$

$$\frac{\partial}{\partial t}(da^*) = \frac{1}{i\hbar}\left[-(\tilde{\Sigma}_{e,d} + \tilde{\Sigma}_{g,a})da^* - V_{da}|a|^2 + V_{ad}^*|d|^2 + (\tilde{\Sigma}_{g,d} + \tilde{\Sigma}_{e,a})^*da^*\right] \tag{B.37}$$

Using the definition of the density matrix $\rho = |\phi\rangle\langle\phi|$, it is straightforward to show that these equations are equivalent to the RDDI quantum master equation,

$$\frac{\partial}{\partial t}\rho = -\frac{i}{\hbar}[H_{coh}, \rho] - \sum_{k,k'} \frac{\gamma_{kk'}}{2}[\sigma_k^\dagger \sigma_{k'}\rho - 2\sigma_{k'}\rho\sigma_k^\dagger + \rho\sigma_k^\dagger\sigma_{k'}]. \tag{B.38}$$

where the first term contains the coherent Hamiltonian, $H_{coh} = \sum_{n=g,e}(\omega_{n,d}+\delta\omega_{n,d})\sigma_d^\dagger\sigma_d + \sum_{n=g,e}(\omega_{n,a}+\delta\omega_{n,a})\sigma_a^\dagger\sigma_a + \sum_{k\neq k'} J_{kk'}\sigma_k^\dagger\sigma_{k'}$, while the second term contains the relevant dissipative terms. The RDDI master equation has been derived here for two non-identical atoms. We emphasize this equation describes coherent coupling between two atoms in a Markovian reservoir but cannot describe non-Markovian dynamics or multi-photon effects arising from strong-coupling between the atoms and the electrodynamic field. In other words, it must operate in a regime where the frequency shifts and dipole-dipole couplings are much smaller than the transition frequencies of the atoms ($\delta\omega_k, J_{kk'} \ll \omega_k, \omega_{k'}$). Going beyond this regime requires an expansion of the Hilbert space and corresponds to the ultra-strong coupling regime. To recover the semi-classical Förster regime, we must include a phenomenological dephasing term for each atom described by the super-operators, $\gamma_{\phi,d}\mathcal{L}_{\phi,d} + \gamma_{\phi,a}\mathcal{L}_{\phi,a}$. These terms describe fluctuations in the energy levels resulting in linewidth broadening and loss of coherence. Explicitly, the dephasing super-operators acting on the density operator in the single-excitation sub-space are given by

$$\mathcal{L}_{\phi,d} = \mathcal{L}[\hat{\sigma}_d^\dagger\hat{\sigma}_d]\rho = -\frac{1}{2}\begin{pmatrix} 0 & \rho_{da} \\ \rho_{ad} & 0 \end{pmatrix}, \tag{B.39}$$

$$\mathcal{L}_{\phi,a} = \mathcal{L}[\hat{\sigma}_a^\dagger\hat{\sigma}_a]\rho = -\frac{1}{2}\begin{pmatrix} 0 & \rho_{da} \\ \rho_{ad} & 0 \end{pmatrix}. \tag{B.40}$$

Combining the results above, we find the single-excitation populations satisfy

$$\dot{\rho}_{dd} = \frac{i}{\hbar}(V_{da}\rho_{ad} - V_{da}^*\rho_{da}) - \gamma_d\rho_{dd} \tag{B.41}$$

$$\dot{\rho}_{aa} = \frac{i}{\hbar}(V_{ad}\rho_{da} - V_{ad}^*\rho_{ad}) - \gamma_a\rho_{aa} \tag{B.42}$$

while the coherences obey

$$\dot{\rho}_{da} = +i\omega_1\rho_{da} + \frac{i}{\hbar}(V_{da}\rho_{aa} - V_{ad}^*\rho_{dd}) \tag{B.43}$$

$$\dot{\rho}_{ad} = -i\omega_1^*\rho_{ad} - \frac{i}{\hbar}(V_{da}^*\rho_{aa} - V_{ad}\rho_{dd}). \tag{B.44}$$

To simplify the equations, we defined $\omega_1 = (\tilde{\omega}_a - \tilde{\omega}_d) + i\gamma_1$, and $\gamma_1 = (\gamma_d + \gamma_{\phi,d} + \gamma_a + \gamma_{\phi,a})/2$, with $\tilde{\omega}_a = \omega_a + \delta\omega_a = (\omega_{e,a} - \omega_{g,a}) + (\delta\omega_{e,a} - \delta\omega_{g,a})$, and $\tilde{\omega}_d = \omega_d + \delta\omega_d = (\omega_{e,d} - \omega_{g,d}) + (\delta\omega_{e,d} - \delta\omega_{g,d})$ which was also used in the main text.

B.3 Non-stationary energy transfer efficiency

In this section, we derive the fundamental relation that provides a unified treatment of the energy transfer efficiency in the coherent and incoherent coupling regimes. The non-stationary energy transfer efficiency is obtained by integrating the population equations (B.41)-(B.42) from 0 to ∞,

$$\rho_{dd}(\infty) - \rho_{dd}(0) = -1 = \frac{i}{\hbar}V_{da}\int_0^\infty \rho_{ad}(t)\,dt - \frac{i}{\hbar}V_{da}^*\int_0^\infty \rho_{da}(t)\,dt - \gamma_d\int_0^\infty \rho_{dd}(t)\,dt, \tag{B.45}$$

$$\rho_{aa}(\infty) - \rho_{aa}(0) = \quad 0 = \frac{i}{\hbar}V_{ad}\int_0^\infty \rho_{da}(t)\,dt - \frac{i}{\hbar}V_{ad}^*\int_0^\infty \rho_{ad}(t)\,dt - \gamma_d\int_0^\infty \rho_{aa}(t)\,dt. \tag{B.46}$$

We have assumed the donor is initially in the excited state, $\rho_{dd}(0) = 1$, with the acceptor in the ground state, $\rho_{aa}(0) = 0$. In the long-time limit, the initial excitation leaves the donor-acceptor system resulting in $\rho_{dd}(\infty) = \rho_{aa}(\infty) = 0$. Adding the population equations (B.45)-(B.46) yields the fundamental relation

$$\gamma_d\int_0^\infty \rho_{dd}(t)\,dt + \gamma_a\int_0^\infty \rho_{aa}(t)\,dt = 1. \tag{B.47}$$

Physically, this equation determines the probability of detecting a single photon from the two-atom system, which must equal one in the long-time limit. This result is applicable when a single excitation is initially present in the system. We also assume that both atoms have unit quantum efficiency and only decay through the emission of

a photon. It is important to note that we have assumed the cooperative decay rate, γ_{da}, is zero. We will address the role of cooperativity and superradiance in a future publication and for now it remains out of the scope of this thesis.

B.3.1 Exact solution to the energy transfer efficiency

The energy transfer efficiency is defined as $\eta_{et} = \gamma_a \int_0^\infty \rho_{aa}(t')dt'$. The exact solution to this expression gives the energy transfer efficiency valid in both the weak and strong coupling regimes. There are two approaches to finding the integrated population $\int_0^\infty \rho_{aa}(t')dt'$. The first approach finds the expression for $\rho_{aa}(t')$, then performs the time integral analytically. We introduce a second approach here. Integrating the coherence differential equations, (B.43)-(B.44), from 0 to ∞, we substitute the result into (45)-(46),

$$-1 = -(\tilde{\gamma}_d + \Gamma_{da})\bar{\rho}_{dd} + \Gamma_{da}\bar{\rho}_{aa} \tag{B.48}$$

$$0 = -(\tilde{\gamma}_a + \Gamma_{da})\bar{\rho}_{aa} + \Gamma_{da}\bar{\rho}_{dd} \tag{B.49}$$

where we have defined $\bar{\rho}_{kk} = \int_0^\infty \rho_{kk}(t')dt'$ for the donor and acceptor respectively $k = \{d, a\}$. We also introduce the bare energy transfer rate,

$$\Gamma_{da} = \frac{|V_{dd}|^2}{\hbar^2} \frac{(\gamma_d + \gamma_{\phi,a} + \gamma_d + \gamma_{\phi,b})}{(\tilde{\omega}_d - \tilde{\omega}_a)^2 + (\gamma_d + \gamma_{\phi,d} + \gamma_d + \gamma_{\phi,a})^2/4}. \tag{B.50}$$

Solving for $\bar{\rho}_{aa}$, the non-perturbative expression for the FRET efficiency is

$$\eta = \frac{\tilde{\Gamma}_{da}}{\tilde{\Gamma}_{da} + \gamma_d} \tag{B.51}$$

where $\tilde{\Gamma}_{da}$ is the *renormalized* energy transfer rate

$$\tilde{\Gamma}_{da} = \frac{\gamma_a \Gamma_{da}}{\gamma_a + \Gamma_{da}} \tag{B.52}$$

as shown in Chapter 6. This modified energy transfer rate is one of the major results of Chapter 6 highlighting the drastic modification of the energy transfer efficiency compared to previous theoretical models. These results imply a fundamental bound

for the energy transfer rate and efficiency as discussed in the thesis. Note we have also derived the same analytical expression using the first approach (1), i.e. analytically evaluating the time-integral.

B.4 Quantum entanglement in energy transfer

In the following, we introduce Wooter's concurrence to describe quantum entanglement between two qubits.

Concurrence. The general wavefunction describing 2 qubits is

$$|\psi\rangle = \alpha\,|e_d, e_a\rangle + \beta\,|e_d, g_a\rangle + \gamma\,|g_d, e_a\rangle + \delta\,|g_d, g_a\rangle\,. \tag{B.53}$$

An appropriate measure of entanglement, given by the concurrence, is $C = 2|\alpha\delta - \gamma\beta| \geq 0$. A concurrence of 1 refers to a maximally-entangled state, while $C = 0$ refers to separable states. In the energy transfer problem with a single excitation ($\alpha = 0$), the concurrence is simply given by $C = 2|\beta\gamma|$. Using the notation of section 1, the time-dependent concurrence is $C(t) = 2|d(t)a(t)|$. The result is easily generalized for a density operator describing mixed states. Here, the concurrence is defined as

$$C = \max[0, \sqrt{\lambda_1} - \sqrt{\lambda_2} - \sqrt{\lambda_3} - \sqrt{\lambda_4}] \tag{B.54}$$

where λ_i are the eigenvalues of the operator $\rho(\sigma_y \otimes \sigma_y)\rho^*(\sigma_y \otimes \sigma_y)$ in descending order. For the non-stationary energy transfer problem where the donor is initially in the excited-state, the eigenvalues are readily solved analytically giving the final result

$$C = 2|\rho_{da}| \tag{B.55}$$

and is therefore exactly dependent on the coherence between both atoms in the site basis. Concurrence provides a measure of entanglement as well as coherence, making it an appropriate choice for studying non-classicality in the energy transfer problem.

B.5 Two atoms above a mirror

B.5.1 Free-space Green function

Here, we provide the full Green function expression for two atoms above a mirror. The dyadic Green function in a bulk medium with refractive index $n = \sqrt{\epsilon}$ satisfies the vector wave equation,

$$\nabla \times \nabla \times \mathbf{G}_o(\mathbf{r}, \mathbf{r}'; \omega) - \epsilon \frac{\omega^2}{c^2} \mathbf{G}_o(\mathbf{r}, \mathbf{r}'; \omega) = \mathbf{1}\delta(\mathbf{r} - \mathbf{r}'). \tag{B.56}$$

The homogeneous Green function has a well-known solution ($k = \sqrt{\epsilon}\,\omega/c$):

$$\mathbf{G}_o(\mathbf{r}) = \left[\frac{1}{k^2}\nabla \otimes \nabla + \mathbf{I}\right] \frac{e^{ikr}}{4\pi r} \tag{B.57}$$

$$= \frac{e^{ikr}}{4\pi k^2 r^3}\left[(k^2r^2 + ikr - 1)\mathbf{I} + (3 - 3ikr - k^2r^2)\hat{\mathbf{r}} \otimes \hat{\mathbf{r}}\right] - \frac{1}{3k^2}\delta(\mathbf{r})\mathbf{I} \tag{B.58}$$

containing both Coulombic near-field ($kr \ll 1$) and radiative far-field ($kr \gg 1$) components. We use this result for Fig. 6.1.

B.5.2 Scattered Green function

In the following, we provide the scattered Green function for two atoms above a mirror defined through the normal unit vector $\mathbf{n} = \hat{\mathbf{e}}_z$. The scattered Green function is found self-consistently through the use of electrodynamic boundary conditions. It is possible to show, upon simplification, that the scattered Green function takes the following form in cylindrical coordinates [86]

$$G^s_{xx}(\mathbf{r}) = \frac{i}{8\pi k_1^2}\int dk_\rho \frac{k_\rho}{k_z} e^{2ik_z d}\left[k_1^2 J_+ r_s - k_z^2 J_- r_p\right] \tag{B.59}$$

$$G^s_{xz}(\mathbf{r}) = \frac{i}{8\pi k^2}\int dk_\rho \frac{k_\rho}{k_z} e^{2ik_z d}\left[-2ik_\rho k_z J_1(k_\rho \rho) r_p\right] \tag{B.60}$$

$$G^s_{zx}(\mathbf{r}) = \frac{i}{8\pi k^2}\int dk_\rho \frac{k_\rho}{k_z} e^{2ik_z d}\left[+2ik_\rho k_z J_1(k_\rho \rho) r_p\right] \tag{B.61}$$

$$G^s_{zz}(\mathbf{r}) = \frac{i}{8\pi k^2}\int dk_\rho \frac{k_\rho}{k_z} e^{2ik_z d}\left[2k_\rho^2 J_o(k_\rho \rho) r_p\right] \tag{B.62}$$

where d is the distance of the donor and acceptor from the mirror interface, and ρ is the lateral separation distance between the donor and acceptor. We also introduced

$J_\pm = J_o(k_\rho\rho) \pm J_2(k_\rho\rho)$, where $J_n(k_\rho\rho)$ is the cylindrical Bessel function of order n. The Fresnel reflection coefficients for p and s polarized light are:

$$r_p = \frac{\epsilon_2 k_z - \epsilon k_{z2}}{\epsilon_2 k_z + \epsilon k_{z2}} \text{ and } r_s = \frac{k_z - k_{z2}}{k_z + k_{z2}}. \tag{B.63}$$

with z-component wavevectors, $k_z = \sqrt{\epsilon\,\omega^2/c^2 - k_\rho^2}$ and $k_{z2} = \sqrt{\epsilon_2\,\omega^2/c^2 - k_\rho^2}$. The full Green function integral is evaluated numerically using an adaptive Gauss-Kronrod quadrature. In the near-field limit ($d, \rho \ll \lambda$) the interaction between each atom and the mirror, $|\epsilon_2| \gg \epsilon_1$, is easily understood through the image dipole model described in the main text.